NUMERICAL MODELLING OF REINFORCED CONCRETE PRESSURE TUNNELS USING THE OVERLAPPING LATTICE METHOD

A THESIS SUBMITTED TO
THE GRADUATE SCHOOL OF NATURAL AND APPLIED SCIENCES
OF
MIDDLE EAST TECHNICAL UNIVERSITY

BY

GÖKBERK IŞIK

IN PARTIAL FULFILLMENT OF THE REQUIREMENTS
FOR
THE DEGREE OF MASTER OF SCIENCE
IN
EARTHQUAKE STUDIES

SEPTEMBER 2019

Approval of the thesis:

NUMERICAL MODELLING OF REINFORCED CONCRETE PRESSURE TUNNELS USING THE OVERLAPPING LATTICE METHOD

submitted by **GÖKBERK IŞIK** in partial fulfillment of the requirements for the degree of **Master of Science in Earthquake Studies Department, Middle East Technical University** by,

Prof. Dr. Halil Kalıpçılar
Dean, Graduate School of **Natural and Applied Sciences** _____

Prof. Dr. Ayşegül Askan Gündoğan
Head of Department, **Earthquake Studies** _____

Prof. Dr. Kağan Tuncay
Supervisor, **Earthquake Studies, METU** _____

Prof. Dr. Yalın Arıcı
Co-Supervisor, **Civil Engineering, METU** _____

Examining Committee Members:

Prof. Dr. Erdem Canbay
Civil Engineering, METU _____

Prof. Dr. Kağan Tuncay
Earthquake Studies, METU _____

Prof. Dr. Yalın Arıcı
Civil Engineering, METU _____

Prof. Dr. Barış Binici
Civil Engineering, METU _____

Dr. Halit Cenan Mertol
Civil Engineering, Atılım University _____

Date: 06.09.2019

I hereby declare that all information in this document has been obtained and presented in accordance with academic rules and ethical conduct. I also declare that, as required by these rules and conduct, I have fully cited and referenced all material and results that are not original to this work.

Name, Surname: Gökberk Işık

Signature:

ABSTRACT

NUMERICAL MODELLING OF REINFORCED CONCRETE PRESSURE TUNNELS USING THE OVERLAPPING LATTICE METHOD

Işık, Gökberk
Master of Science, Earthquake Studies
Supervisor: Prof. Dr. Kağan Tuncay
Co-Supervisor: Prof. Dr. Yalın Arıcı

September 2019, 98 pages

Pressure tunnels transmit water from the reservoir to the turbines of hydroelectric power plants. The computational studies conducted to understand the behavior and shed light on the design guides of pressure tunnels were scarcely validated with experimental data as experimental work on pressure tunnels is very limited. Recent experimental studies on reinforced concrete pressure tunnels carried out at the Middle East Technical University (METU), for the first time, allow computational models to be validated with experimental data. Instead of the conventional approach of using finite elements with smeared and discrete crack models, in this study, an Overlapping Lattice Model (OLM) was used to simulate the nonlinear behavior of the reinforced concrete tunnel as well as the surrounding rock body. First, parameters used in the OLM were calibrated using the fracture energy, the tensile strength and the elasticity modulus of concrete. A normalization rule was developed to make sure that energy dissipation is independent of lattice length scale. Then, the quasi-static tunnel experiments performed at METU were simulated and internal pressure-tunnel expansion curves as well as crack patterns obtained in the numerical studies were compared with the experimental observations. OLM predictions are shown to be in agreement with the experimental data. Calibrated model was then applied to study

dynamic crack initiation and propagation in pressure tunnels. In line with the experimental observations and numerical inferences, in-situ stress conditions in the surrounding rock body play an important role on the behavior of the tunnel lining. Low confining stress or lack of sufficient contact between tunnel lining and surrounding rock body are possible causes of the cracks observed in pressure tunnels. As a future research opportunity, OLM developed in the context of this research can be used to evaluate the seismic behavior of tunnels.

Keywords: Pressure Tunnel, Reinforced Concrete, Simulation, Lattice Model, Fracture Mechanics

ÖZ

İÇ BASINÇLI BETONARME TÜNELLERİN ÖRTÜŞEN KAFES MODELİ KULLANILARAK SAYISAL MODELLENMESİ

Işık, Gökberk
Yüksek Lisans, Deprem Çalışmaları
Tez Danışmanı: Prof. Dr. Kağan Tuncay
Ortak Tez Danışmanı: Prof. Dr. Yalın Arıcı

Eylül 2019, 98 sayfa

Basınçlı enerji tünelleri, hidroelektrik santrallerde suyu rezervuardan türbinlere iletirler. Bu tünellerin davranışını anlamak ve tasarım kılavuzları oluşturmak için yapılan hesaplama çalışmaları, deneysel çalışmaların sınırlı olması nedeniyle güçlükle doğrulanabilmiştir. Orta Doğu Teknik Üniversitesinde (ODTÜ) betonarme enerji tünelleri üzerine yapılan deneysel son çalışmalar, ilk kez hesaplama modellerinin deneysel verilerle doğrulanmasına imkân sağlamıştır. Yayılı ve ayrık çatlak modelleriyle sonlu elemanların kullanılmasına yönelik geleneksel yaklaşımlar yerine, bu çalışmada, betonarme tünelin ve çevresindeki kayanın doğrusal olmayan davranışını simüle etmek amacıyla Örtüşen Kafes Metodu - OLM (Overlapping Lattice Method) kullanılmıştır. İlk olarak, OLM'de kullanılan parametreler çatlak enerjisi, çekme dayanımı ve betonun elastisite modülü kullanılarak kalibre edilmiştir. Enerji dağılımının eleman uzunluğu ölçeğinden bağımsız olmasını sağlamak için bir normalleştirme kuralı geliştirilmiştir. Daha sonra ODTÜ'de yapılan yarı-statik tünel deneyleri simüle edilmiş, iç basınç-tünel açılma eğrilerinin yanı sıra sayısal çalışmalarda elde edilen çatlak dağılımları, deneysel gözlemlerle karşılaştırılmış ve OLM tahminlerinin deneysel verilerle uyumlu olduğu gösterilmiştir. Son olarak kalibre edilmiş model, basınçlı tünellerde dinamik etkiler altında çatlak oluşumlarını

ve yayılımlarını incelemek amacıyla kullanılmıştır. Deneysel gözlemler ve sayısal çıkarımlar doğrultusunda, tünel etrafındaki kayanın yerinde gerilme koşullarının, tünel kaplamasının davranışı üzerinde önemli bir rol oynadığı ortaya konmuştur. Tünel kaplaması ile etrafındaki kayanın arasında yeterli temasın olmaması ya da kayanın düşük saha gerilimlerine sahip olması, basınç tünellerinde gözlenen çatlakların olası nedenleri olarak gösterilmiştir. Bu çalışma kapsamında geliştirilen OLM'nin, tünellerin sismik davranışını değerlendirmek için de kullanılabileceği görülmüştür

Anahtar Kelimeler: Basınçlı Tüneller, Betonarme, Simülasyon, Kafes Modelleri, Çatlama Mekaniği

To My Family..

ACKNOWLEDGEMENTS

This work is supported by Scientific and Technological Research Council of Turkey, TUBİTAK under grant number: 215M870.

First of all, I would like to express my gratitude Prof. Dr. Kağan Tuncay. He always supported and encouraged me with his knowledge and criticism. Whenever I needed help or had a question about my study, his office door was always open for me.

I would like to thank my co-supervisor Prof. Dr. Yalın Arıcı, who helped me to start working for this study, and to project members Prof. Dr. Erdem Canbay and Prof. Dr. Barış Binici, for their guidance and support.

I would like to express my sincere thanks to Dr. Engin Karaesmen and Dr. Erhan Karaesmen for sharing knowledge and invaluable experiences with me. I would also like to thank Prof. Dr. Ayşegül Askan Gündoğan for her motivation and encouragement.

One of the biggest thanks belongs to my dearest colleague and beloved wife, Yağmur Topçuoğlugil Işık. Her sacrificing support and companionship through many late nights and weekends with numerous technical discussions contributed a lot to this work. Completing it would have been impossible without her love and friendship.

I would specifically like to thank my beloved mother Birgül Işık, my father Orhan Işık and my sister Gökçen Işık for their endless love and support. I would also like to thank my family members Berrin Özler, Cansın Özler and my second family members, Münevver Semen and Özge Topçuoğlugil.

I would like to extend my sincere thanks to my friends Mert Uluçay, Doğancan Aksu, Anıl Öztürkler, Koray Akça, Furkan Uyar and Okan Özmen for long-standing friendships and unforgettable moments we shared from the beginning of our high school years till today. I would also like to thank my colleagues Ezgi Çınar and

Mertcan Genç for their friendship and encouragements. It is great to know they will be with me throughout my life.

I would also like to thank all the members of Arup Ankara, especially my colleagues Caner Soydaş, Avnican Karadeniz and Engin Keskin for their support.

TABLE OF CONTENTS

LIST OF TABLES

TABLES

LIST OF FIGURES

FIGURES

CHAPTER 1

INTRODUCTION

1.1. General

Pressure tunnels, which are key components of hydroelectric energy systems, are subjected to high internal pressure due to hydraulic head difference between tunnel interior and exterior. Unlike conventional tunnels constructed as parts of transportation systems, internal pressure on the walls of the tunnel is the primary load for the tunnel lining. Internal pressure increases suddenly during filling and leads to tensile stresses on tunnel lining in the hoop direction. Properties of rock formations surrounding pressure tunnels and in-situ stresses are among the key factors in the design of tunnel lining. In this study, laboratory scale pressure tunnel experiments were computationally studied to enhance our understanding of quasi-static pressure tunnel behavior. The validated simulation tool was then used to get insight into the dynamic behavior of pressure tunnels.

1.2. Organization of Thesis

This thesis is divided into five chapters. First chapter is presented as an overview and includes the motivation of the study.

Second chapter provides a brief introduction of literature including previously studied pressure tunnels and a brief background on computational modelling of nonlinear behavior of reinforced concrete members.

The details of the simulation tool Overlapping Lattice Model (OLM) and the theoretical and numerical background of the model are explained in Chapter 3. Validation studies are also presented in this chapter.

In Chapter 4, the brief information about pressure tunnel experiments conducted at the Structural Laboratory of the Middle East Technical University are given. After providing numerical setup of the OLM simulations, quasi-static results are compared with the experimental data. Then, validated OLM is used to evaluate the dynamic behavior of the tunnel.

Chapter 5 summarizes the numerical findings for the pressure tunnels and provides recommendations for future work.

1.3. Objectives

This study aims to apply the OLM to predict the nonlinear behavior of reinforced and fiber-reinforced concrete tunnel linings for the first time in the literature. The emphasis is on the prediction of the nature of dynamic crack initiation and propagation. The major objectives of the study are listed as follows:

- Calibrate the OLM parameters for concrete and fiber-reinforced concrete
- Validate the OLM for crack initiation and propagation with experimental data
- Investigate the influence of the surrounding rock properties and in-situ stress on the quasi-static and dynamic behavior of reinforced concrete and synthetic fiber-reinforced concrete lining performance

The development of such a numerical model, calibrated with experimental results, which was obtained recently at METU, is the main outcome of this study. Based on the findings of this study, design and production stages of the pressure tunnel can be evaluated in depth. It is hoped that the research effort spent in this thesis will lead to novel design guides to assist practicing engineers.

CHAPTER 2

LITERATURE REVIEW

2.1. Pressure Tunnels

Dams are generally constructed to meet more than one purpose. These purposes may be irrigation, water-supply, flood control, food-supply (fishing) and energy production. With the development of hydropower projects to convert the energy of falling water to electricity, energy tunnels (or pressure tunnels) that are constructed to transmit water in reservoirs through turbines have become one of the most important concerns in such power plants. In general, requirements of these tunnels are quite simple: to convey water safely through to energy turbines without excessive water loss and residual materials, to transmit internal pressure to the surrounding rock body, and to remain operational for the life of the project without major maintenance costs. In Turkey, energy tunnels completed in recent years include Arkun (13655 m), Kandil (9513 m), Tefen (3200 m), Topçam (7460 m), Dim (4221 m) and Akkay (12430 m) energy tunnels. A large number of energy tunnels are also under construction as of today. Internal pressure in these tunnels are in the range of 0.3 to 3 MPa.

USBR Design Standard (2014) classifies the range of unlined pressure tunnels maximum velocities from 1.1 m/s to 2.7 m/s depending on whether paved inverts are built or not, and classifies concrete-lined pressure tunnels with a usual flow velocity of about 3.0 m/s and a maximum velocity of 6.1 m/s. Although, in every structural design, maximum flow velocity is limited, smooth water flow does not cause damage in the tunnel lining if a good quality of concrete surface is available. Sudden changes in tunnel cross section that may cause velocity jumps and pressure drops, result in formation of vapors bubbles (cavitation) and extensive erosion of rock or lining layers. Cavitation may also occur when rapid flowing water is in contact with rough surfaces.

In short, design flow velocity selection depends on hydraulic head loss calculations due to friction and erosion of tunnel lining.

Unlike dry tunnels, the basic structural design consideration in these tunnels is the internal pressure applied to the interior walls of the tunnel. This pressure increases with the filling of the tunnel and leads to tension in the tunnel lining. As the internal pressure may be as high as 2-3 MPa, the tensile stress exceeds the tensile strength of concrete resulting in cracks. This may cause host material fallout, infiltration, exfiltration of water and even cavitation. Therefore, performance criteria are required for the internal pressure tunnels.

In the tunnel design, it is generally assumed that the lining carries at least 30% of the internal pressure load (Sinha, 1989). In order to make this assumption, it is necessary to have sufficient tunnel lining-rock contact. Pressure tunnels are surrounded by rock formations and in-situ stresses are key factors affecting the lining behavior. In-situ stress conditions are generally assumed from overburden rock layers, since it is very difficult to obtain reliable measurements from deep boreholes or in-situ data using hydraulic fracturing tests, jacking tests, etc. For this reason, depending on the quality of rock mass, a reinforced lining can be preferred to provide crack control and limit water outflow from the tunnel. As described in Palmström and Stille (2015), the most preferable rock masses are fair and good quality crystalline, unweathered rocks such as granite, gneiss, basalt and quartzite. Although rocks are divided into three major classes according to their formation, there are different approaches to classify ultimate strength. In the Geological Strength Index (GSI) charts based on Hoek's descriptive catalogues (Hoek et al., 1998), classification depends on observations and visual impressions of the rock mass. This grading procedure requires qualified and experienced geologists. However, it is not precise and it is used as an initial estimate for the classification of rocks. In addition, rock quality can be investigated with modulus of deformation values, which is the ratio of stress to the corresponding strain including elastic and inelastic parts. It can be computed using the Rock Quality Designation method (RQD) by the degree of fracture in a rock mass (Coon and Merritt,

1969) or the Rock Mass Rating (RMR) (Bieniawski, 1978) considering six different parameters which are uniaxial compressive strength, RQD, spacing discontinuities, condition of discontinuities, orientation of discontinuities and groundwater condition. The sum of assigned values of these six parameters give RMR value which ranges between 0 and 100.

Tunnel materials that are recommended according to the magnitude of internal pressure are given in Table 1. Depending on the selection of tunnel lining material, pressure tunnels can be designed as impermeable, semi-permeable and permeable. Material used for the tunnel lining depends on the level of water pressure. Reinforced concrete linings are recommended for pressure levels up to 0.70 MPa (Table 1) excluding the dynamic amplification factor. Reinforced concrete tunnel linings are considered as semi-permeable. If the radius/thickness ratio is taken to be 4-5 (a typical value), with the dynamic amplification factor, this leads to tensile stresses in the order of 2-3 MPa in the tunnel lining. When horse-shoe shaped tunnel geometry is chosen, due to the stress concentration at the bottom corners, this value is expected to be exceeded further. Even for a circular tunnel geometry, this level of tensile stress is sufficient to cause cracking in concrete which is then infiltrated by water potentially further increasing crack widths.

Table 1. *Support systems according to internal pressure [Sinha, 1989]*

Support System	**Water Pressure**
Rock bolts, Shotcrete	up to 0.30 MPa
Concrete lining	0.30 - 0.70 MPa
Steel sets	0.70 - 1.50 MPa
Steel lining	More than 1.50 MPa

As seen in Table 1, it is suggested that impermeable linings (steel oriented) should be selected if internal pressure higher than 1.5 MPa. In Turkey, due to the economic reasons and constraints on construction time, most tunnels in energy systems have been constructed using shotcrete (wherein said shotcrete is acceptable as a support having a thickness greater than 75 mm, is not the one used as a protective coating) and

reinforced / non-reinforced concrete. Unlined pressure tunnels were even preferred. Although, for instance in Norway, there are more than 80 safely operating unlined, high head pressure shafts and tunnels, such designs without adequate geo-investigations and rock stress measurements may result in catastrophic consequences (Palmstrom, 1987). Different design solutions should be used for this type of applications like headrace tunnels to stabilize the pressure level until a certain point or pipelines to deal with high pressure in short distances (Figure 1).

Regardless of the tunnel type selection, in many cases, first filling, emptying and later refilling procedures should be done slowly to avoid permanent damages in the tunnel.

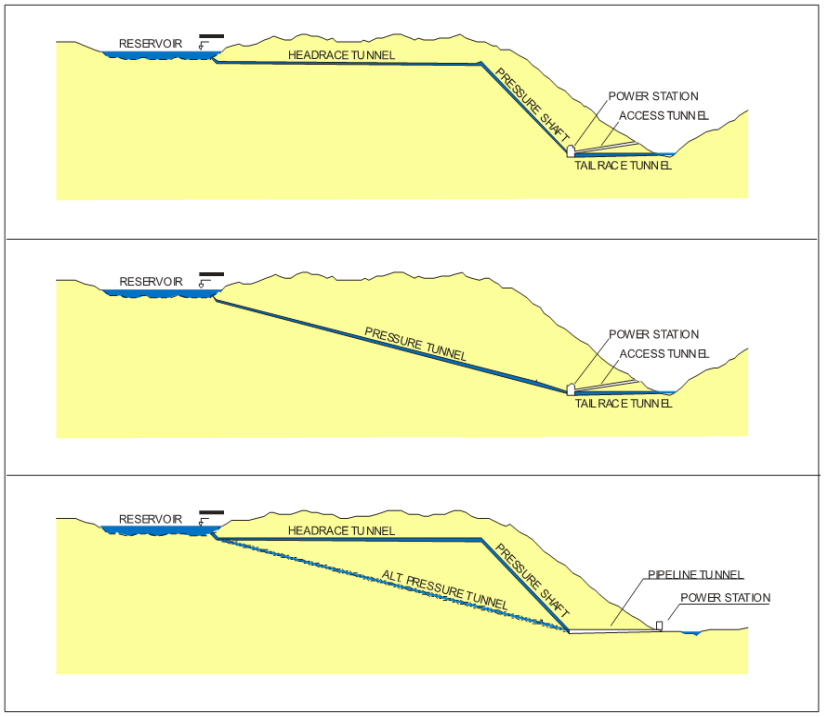

Figure 1. *Different design solutions for pressure tunnels and shafts [Palmstrom, 1987]*

Since underground tunnel shapes are influenced by their intended usage, hydraulic decisions and construction methods, circular and modified horseshoe shape geometries are the common ones. Circular tunnels are the most suitable to withstand internal and external forces since they do not have any stress concentration at the bottom corners and have better stress transfer to the surrounding rock body. In Turkey,

pressure tunnels are mostly horseshoe-shaped due to the fact that the flat floor gives enough working space in drilling and blasting applications. A comparative study evaluating the effects of different tunnel geometries on the behavior by Ng, Wang, and Boonyarak (2016) revealed that a tunnel with reverse horseshoe geometry experiences approximately 20% more vertical elongation than a tunnel with regular circular geometry. With a larger vertical expansion, more bending strains at the flat invert of the horse-shoe shaped tunnel develop as expected.

The seismic risk of underground structures increases closer to active fault zones with the increase in ground accelerations. Design loads of underground structures are calculated in estimating deformations and strains imposed on the structure by the surrounding ground depending on seismicity level. Therefore, the main variable affecting design is the free field movement of the ground and its interaction with the structure. This approach is admissible for relatively low energy motions and the structures constructed in relatively stiff mediums (Hashash et al., 2001). In the study of Dowding and Rozen (1978), rock-tunnel responses to earthquake motions were compared with selected ground motions (ground accelerations and peak ground velocities, PGAs and PGVs) for 71 cases to determine damage levels. It is concluded that moderate to heavy damages will occur in tunnels only if the PGAs are larger than 0.5 g (gravitational acceleration). In USBR (2014), it is reported that for PGA values lower than 0.19 g, there were no observable damage in the existing tunnels located in the stiff rock bodies. It is further indicated by Jaramillo (2017) that tunnels in rock are able to withstand moderate earthquake events.

2.1.1. Early Computational Studies

The stress distribution due to a point load on a two or three dimensional medium was given by the well-known formulae of Boussinesq (1877). It was based on the assumption of a linear–elastic, homogeneous, isotropic material behavior. Boussinesq's solution was integrated into the preliminary studies to estimate the stress distribution in tunnel lining design by Biot (1935) and Westergaard (1938). In the

proposed tunnel analysis, the radial displacement of the tunnel was determined under internal pressure and the required support was calculated.

In the 1980s, a number of studies were conducted assuming permeable or semi-permeable tunnel linings (Schlesis, 1986; Fernández, 1994; Schleiss, 1997), Hendron's potential failure modes of pressure tunnels have been presented as excessive leakage, excessive pore-water pressures in rock mass, collapse of openings and mechanical failure of linings (as cited in Fernández, 1994). Considering the potential failure modes, excessive flow out of the lining appear to be a major reason for the stability and strength loss of the tunnel. The water amount flowing out of cracked concrete changes the material behavior of concrete lining. Even the gaps in millimeters that are neglected in practice are effective in the propagation and distribution of cracks. Therefore, one of the most important parameters in the design of semi-permeable pressure tunnels is the crack width. Hydraulic and mechanical interaction between lining and rock boundaries have to be taken into account to accurately calculate the outflow rate. Vast majority of past failures observed in pressure tunnels were due to water flow through lining and loss of rock integrity. Brekke and Ripley (1993) reported that 59% of pressure tunnels failed due to excessive water loss whereas 22% of them failed due to the loss of rock integrity caused possibly because of excessive water loss. Hence, width and distribution of cracks are particularly important parameters in the design of concrete tunnel linings. Olumide et al. (2012) presented a seepage flow analysis, and found that the leaked-out water could be in accepted range in practice even though with higher internal water pressure if the crack widths are kept below a certain level. However, there is no design guide to determine the crack width limit for these energy tunnels. In today's existing regulations, the crack width limit is reported to be around 0.3 mm. TS-500 (2000) structure design regulation in force in Turkey gives the service crack width for humid conditions in the order of 0.2 - 0.3 mm, while ASTM C-76-15 (2009) (Standard Specification for Reinforced Concrete Culvert, Storm Drain, and Sewer Pipe) gives

the crack limit for pressurized reinforced concrete pipes as 0.25 mm, since cracks widths around 0.25 mm allow small silt and sand particles into the tunnel.

Until 2000s, there were very few studies on tunnel behavior and collapse risks due to developing cracks. They were based on estimations of the water pressure level in surrounding rock body and the crack widths evaluated with simple analytical models. However, in these studies, the objective was not to determine how and why the concrete lining is cracked. They focused on the risk of pieces falling into the tunnel from cracks (eg Chung et al., 2001). In the studies on the calculation of the stresses in the tunnel lining with finite element models, it is not possible to accurately predict the location or width of cracks since the concrete lining is modelled as a shell element (Olumide and Marence, 2012). Common deficiencies in these studies are that the numerical results were not validated with experimental results.

Even in properly designed and constructed pressure tunnels, due to shrinkage of concrete and cold joints caused by interruptions of the casting process, there might be a gap between the lining and rock body. Therefore, surrounding rock body does not provide adequate support to the bearing of the internal pressure. Sudden filling applications lead water to seep out from preformed gaps. On the other hand, filling/emptying the tunnel slowly allows pressure equalization and this limits the deformation of lining and rock body. Apart from this reason, to prevent the tunnel form permanent damages, filling rate is determined depending on erosion potential, cavitation risk, safe air escape velocity limits and pressure drops. Maximum filling rate is recommended as 15% of the design flow rate if air valves are used (USBR, 2014). In short, hydro-mechanical coupling of stress redistributions in watering and dewatering stages of the tunnel and seepage calculations become determining factors in tunnel ultimate strength (Olumide, 2013).

As mentioned earlier, there are very few studies in the literature that investigate the structural behavior of pressure tunnel linings with overburden stress from rock body (in-situ stress). Tuncay et al. (2016) stated that magnitude of expansion of the tunnel

lining that causes concrete cracks does not only depend on thickness and stiffness of the lining, but also depends on strength and stiffness of the surrounded rock formation. In order to estimate the effects of geological strength indexes (GSI) of rock formation, overburden heights and lateral to axial stress ratios (K_0) on performance of the horse-shoe shaped concrete tunnel lining, twelve nonlinear finite element analysis have been conducted in the first stage of the study. Based on these simulations, dynamic fracture propagation was estimated via peridynamic analysis and finally an equation was derived showing significant increase in crack width and number as the confinement effects of the rock body decrease.

2.2. Concrete Fracture Mechanics

In Egyptian and later Roman eras, first cementitious material was produced with combination of lime mortars and natural pozzolans to overcome the weakness of stone and brick materials in tension. Over the years, these concrete ingredients were improved upon, combined with other materials and chemical admixtures, and ultimately morphed into the modern portland cement concrete. After the use of steel reinforcement to overcome the tensile strength deficiency, concrete has become the second most used material in the world following water. About 10 billion tons of concrete is produced ever year. In today's world, concrete has many types varying in composition, fabrication and site applications. Normal strength concrete compressive and tensile strengths may range from 20 to 60 MPa and 1.5 to 4.5 MPa, respectively.

Considering its composite mixture, concrete is a typical example of a random heterogeneous material consisting of fine and coarse aggregates which have a wide range of size from a few millimeters to 30-40 millimeters in diameter. This random heterogeneous nature as a consequence of complex microstructure leads to complicated mechanical behavior. This behavior was first attempted to be introduced with linear constitutive models. Griffith (1921) developed the fundamental concepts of linear fracture mechanics. It is stated that fracture occurs when a reduction in

potential energy due to crack propagation becomes greater than the increase in surface energy due to new surfaces. Irwin (1958) further associated fracture theory with the release rate of strain energy and combined it with Weibull's (1939) statistical approach. Fracture parameters were introduced in the mid 1960's in the models of Wells (1961) for metals and were altered for a comparative model for concrete by Jenq and Shah (1985). Starting from the 1960s, a large number of studies have been carried out to shed light on this nonlinear behavior investigating development and propagation of cracks with multi-linear softening material models.

Since the classical linear elastic fracture approach was insufficient to predict progressive failures, cohesive crack models were initiated in the works of Dugdale (1960) and Barenblatt (1959) evaluating stress distribution across cracks in polymer, metal and ceramic types of materials. In the models, it is assumed that the material behaves in a linear-elastic manner until the tensile stress reaches its strength and crack initiates afterwards. With the inspiration of these softening models, fracture energy concept was introduced further for concrete by Hillerborg et al. (1976). It is defined with the G_F denotation as the area under the complete softening stress-displacement curve. G_F was further linked to the area under the initial tangent of the diagram by finding $G_F \approx 2.5G_f$ from the test results (Guinea, Planas, and Elices, 1992). During the crack propagation, this formulation was consistent with the cohesive crack models with fixed softening laws.

Fracture process zone, a region of damage around crack tip, (FPZ) was proposed to overcome crack tip shielding mechanism due to heterogeneous aggregate resistance and to overcome crack propagation accelerating mechanism due to void formation (Bazant and Oh, 1983). Length of fracture process zone which is generally considered as a material property was evaluated over three main behaviors. 1- Negligible size of FPZ in which the behavior approaches to linear elastic fracture mechanics, 2- Significant size of FPZ in which the behavior reaches to ultimate strength or yielding point, 3-Intermediate size of FPZ in which the behavior is in transitional between strength and linear elastic fracture. Size effect law is incorporated with intermediate

size of FPZ which is determined by the size of the inhomogeneity in the microstructure, such as the maximum grain size in rock or the maximum aggregate size in concrete. Rao and Prasad (2001) reported that the size of FPZ increases with coarse aggregate size up to 16 mm, and thereafter it starts to decrease. Cement ratio is also another concrete-mix property which effects the FPZ size, thus it effects the crack branching.

2.2.1. Finite Element-Based Models

With the development of the finite element method for finding numerical solutions to boundary value problems, discrete crack models and two types of smeared crack models came to the forefront to predict crack formation; rotating crack models (Collins and Vecchio, 1986; Rots, 1988) and fixed cracking models (Willam et al., 1987). As the names imply, while the orientation of the crack can change in the rotating crack models, in the fixed crack models it remains constant throughout process. The main disadvantage of finite element-based methods which are developed based on the continuity principle is that the crack cannot be represented in the model in a realistic manner by operating with average strains over a measurement length instead of the actual crack openings. On the other hand, in discrete crack models (Ngo and Scordelis, 1967), crack growth is implemented by nodal split (when the nodal force exceed a tensile strength limit, the node split into two nodes and procedure is repeated in every step). Similar fracture models were developed by using contact elements and springs between discrete finite elements (Ingraffea and Saouma, 1985; Kwak and Filippou, 1990; Rots and Blaauwendraad, 1989). Despite the advantages of the modeling of cracks through discrete elements, as the location of the cracks is not predetermined, the numerical mesh has to be repeatedly reproduced in the simulation process. The need for different structural models in the fracture zone and in the regions where the continuity continues, is another disadvantage of the discrete crack models.

In the following years, a method to determine material fracture parameters, independent of the size effects and remeshing procedures, was developed (Bazant and Planas, 1997). This approach was used to reduce mesh dependency commonly observed in computational studies. However, the formula in the method was not smooth and did not include the statistical part for crack initiation. In the more recent studies (Fantilli et al., 2014; Trivedi et al., 2015), three-point bending tests are used to validate numerical methods of the size independent fracture energy calculations. Although it was shown that bilinear softening models based on size independent fracture energy yield consistent finite elements results, existing continuum based finite element modeling via smeared and discrete crack methods have limitations in capturing the local nature of cracking (Olumide, 2013; Zhou et al., 2015). Alternatively, the extended finite element method (XFEM) has been developed by Belytschko et al. (2000) to capture crack propagation without remeshing and post processing by adding enrichment functions to the displacement-based formulations. The main advantage of this local mesh-free method was that nodes can be easily manipulated around vicinity of the crack tip, adding and removing nodes do not affect crack propagation.

2.2.2. Lattice Based Models

Before the development of finite element-based approaches, numerous researchers endeavored to clarify the behavior of heterogeneous materials using analog models. The easiest way could be thought as characterizing a structure by a truss system, dating back as early as 1900s with the introduction of the truss analogy originally proposed by Ritter (1899). Mörsch (1909) introduced the famous truss case analogy for shear transfer in reinforced concrete beams. Wagner (1929) developed a similar approach to explain the behavior of thin metal beams when they had a higher shear load than the first buckling loads. Weibull (1939) have studied the rupture probability in solids with different mathematical expressions. Hrennikoff (1941) used a truss model to

solve elastic problems. Aforementioned approaches have been developed for the approximate engineering solution in the years when numerical work on a mechanics continued with a focus on the finite element method based on the continuity principle. Due to this continuity limitation of such models, the use of lattice-based models was also continued for simplified nonlinear analysis. In particular, a new truss system named as strut and tie model (STM) (Schlaich et al., 1987) found wide application in the design of deep beams, corbels and pile caps (Figure 2). Fundamental objective of the model was to distribute the load on elements by utilizing the compression and tension stress fields together. Stress trajectories were defined either as B fields (Bernoulli or beam) where stresses are easily derived from sectional forces or D fields (discontinuity or disturbance) where distributions of strains are nonlinear and required capacity calculations. Modeling method has been encouraged for more widespread use, guidelines being included in modern concrete specifications such as Eurocode 2 and ACI 318. Conceptual design of an element or quantitative checks of structural systems can be carried out in a rather easy way using STM.

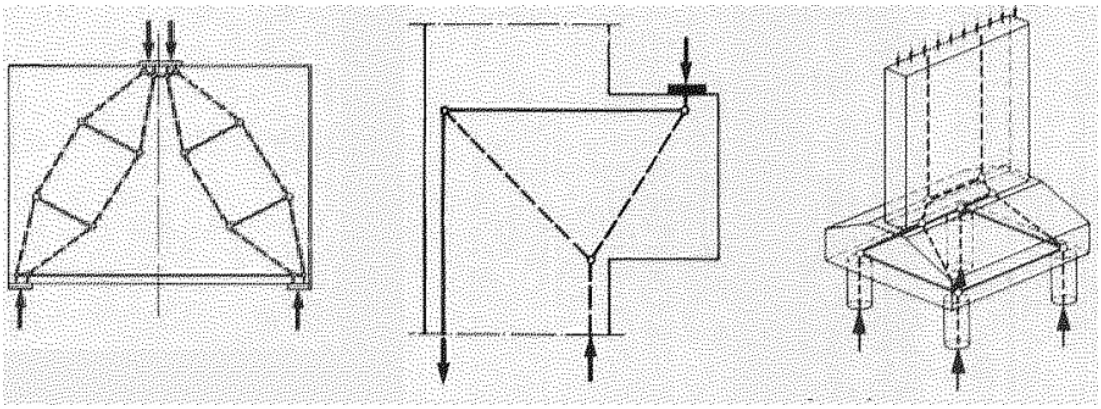

a) Deep beam STM b) Corbel STM c) Pile cap STM

Figure 2. *Strut and tie models [Schlaich et al., 1987]*

First theoretical studies which share a common approach to the modeling of the structure and force flow using a truss system have showed that lattice type models are quite successful for the simulation of concrete behavior. This success encouraged researchers to further investigate lattice-based models to simulate concrete fracture in

detail. For instance, in Herrmann (1988), crack growth was simulated by performing a linear elastic analysis and removing (or partially removing) an element from mesh that exceed threshold tensile strength value. Random heterogeneous nature of concrete was implemented to models in beam strength and stiffness. A three dimensional lattice model was used to simulate mechanical behavior of concrete by connecting aggregates centers in Cusatis et al. (2003). Lattice elements were also used to model cement, aggregates and interfacial transition zones separately with different material constants (Van Mier, 2012). These multi-scale numerical results were in good agreement with the experimental data.

Concrete fracture in previously mentioned studies used lattice or mesh elements considering small springs or beams. Similarly, the peridynamic theory (PD), which was developed by Silling (2000) based on particle interactions has been used to solve many complex engineering problems in recent years. In the bond-based PD, each point connects with adjacent points within a specific distance by a pairwise force function, and damage is incorporated in this pairwise force function by allowing the bonds to break when the elongation exceeds the threshold value. This specific distance that brings nonlocality to the system was called the horizon (δ). It enabled the particles to interact with many particles and capture cracks in arbitrary orientations. Within this horizon, particles continued to carry load even after failure (softening). Particle interaction (bond strength) was integrated to the model as a nonlinear function of extension. For brittle materials that do not exhibit tension softening, after a bond breaks, points at the ends of the bond are disconnected from each other. For materials that exhibit tension softening, the bond force is a nonlinear function of the elongation. The bond forces are continuously updated and the resulting load redistribution is calculated through Newton's equations of motion which enables the consequential anisotropy in material behavior. In Gerstle et al., (2005), PD was employed for plain and reinforced concrete elements. Both rectangular and hexagonal node patterns with different horizon selections were successfully applied to two-dimensional plain strain

problems (Figure 3). It was reported that models with hexagonal node patterns might have rapid convergence and improved material isotropy.

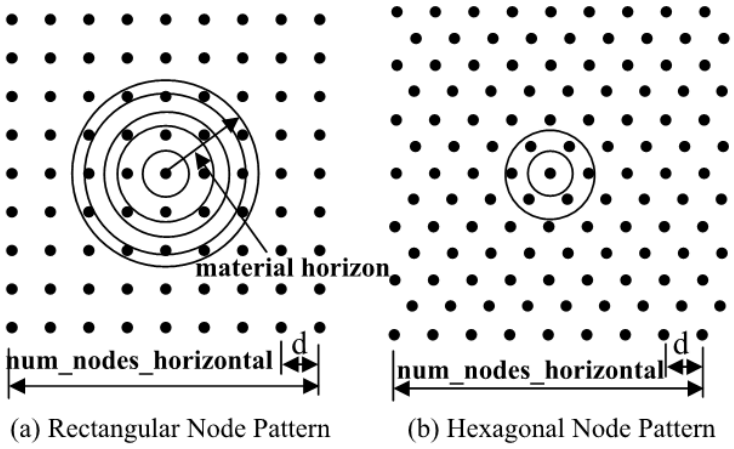

Figure 3. *Node patterns and horizon levels [Gerstle et al., 2005]*

Major shortcoming of the original bond-based PD was the limitation of the representation of poisson's ratio (v) which is 1/3 for two and 1/4 for three dimensional problems in this formulation. Later in Silling et al. (2007), this issue was addressed by introducing rotational degrees of freedom into a bond-based PD and the state based PD theory was introduced. PD models were compared with both experimental and other numerical studies in many applications and it has been validated with experimental data, especially for dynamic crack formation prediction (Gerstle et al., 2009; Madenci and Oterkus, 2014; Mitchell, 2011).

2.3. Fiber-Reinforced Concrete

Fibers have long been used to suppress the weakness of construction materials in tension in composite materials. Historically, naturally available engineering materials including glass, plastic, ceramic and asbestos were used as fibers to reinforce bricks and masonry mortar. Because of health hazards related with asbestos fibers which were widely used in constructions until 1970s, alternate fiber types such as steel and synthetic fibers have been developed. The effect of these fibers on ultimate behavior

were studied by many researchers (Shah and Naaman, 1976; Swamy, 1975). Although moment capacities were not increased significantly, early studies (Henager and Doherty ,1976) showed that using steel fibers in beams improved the flexural behavior by decreasing the crack width and crack spacing. Similarly, in ACI Committee 544, it was reported that randomly distributed steel fibers increases the tensile toughness and ductility of concrete. Use of steel fiber-reinforced concrete in tunnel lining segment is a common method to minimize the cracking for underground rail and road tunnels, since the durability of a tunnel is highly dependent on concrete permeability (Sorelli and Toutlemonde, 2005). Due to the lack of guidelines and manuals in this area, studies (Bakhshi and Nasri, 2016; Johnson et al., 2017) were mostly focused on providing design recommendations for both production and construction stages. In Nitschke et al. (2017), it is demonstrated that macro synthetic fiber-reinforced concrete offers same long term behavior and durability for tunnel linings but better corrosion resistance in aggressive exposure conditions.

As a summary, although finite element and lattice based models were used to predict nonlinear behavior of reinforced and fiber-reinforced concrete beams or columns up until today, very few studies exist to evaluate concrete pressure tunnels in the literature. For the first time, a new computational approach named as the overlapping lattice model used to simulate crack initiation and propagation compared with experimental results.

CHAPTER 3

OVERLAPPING LATTICE MODELLING

3.1. Theory

Overlapping Lattice Model (OLM) is a numerical tool developed in the Civil Engineering Department of the Middle East Technical University. Validation studies of the OLM were reported in Aydın (2017). A computational platform, written in Fortran programming language, following simple rules for the force-deformation response of bonds between nodes was developed. The collective dynamics of damage and complex bond connectivity dictates the OLM response. As in the bond-based peridynamics approach, each material point (node) is assumed to interact with all nodes within a certain distance. This distance is called horizon. If a uniform lattice is used, then horizon is chosen to be proportional to the shortest distance between the nodes, i.e., $\delta = a \times d$ where d represents uniform distances between nodes. Choosing a = 1.5 gives the simplest lattice with 8 bonds for each node whereas choosing a = 3.01 yields 28 bonds with many nonlocal interactions (Figure 4). OLM is not a micro-scale approach that accounts for the distribution of the concrete constituents.

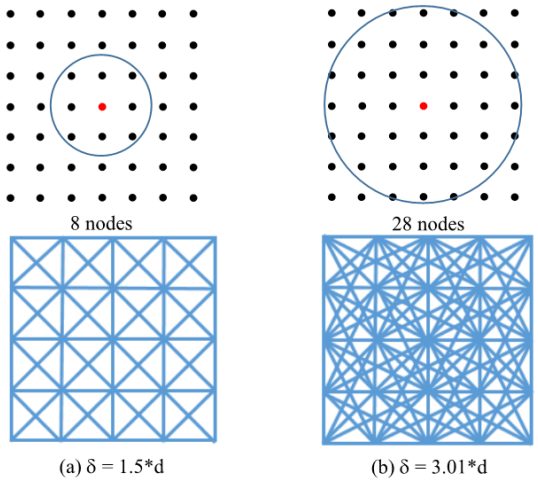

Figure 4. *Lattice system for (a) δ = 1.5 * d and (b) δ = 3.01 * d [Aydın, 2017]*

In the OLM, for an initially linearly elastic isotropic medium, elasticity modulus times cross sectional area (EA_t) is taken to be same for tension and compression of concrete. It is calculated by utilizing the strain energy density approach as presented in Aydın (2017). To calculate the energy in the original geometry $Energy_{original,}$ a deformation field is created by giving an arbitrary deformation field ($\varepsilon_x = \text{constant while } \varepsilon_y = 0$) to every bond. (It was stated that results would be more or less the same if the same procedure applied for other direction) $Energy_{original}$ is expressed as

$$Energy_{original} = \frac{E \times \varepsilon_x \times w \times A}{2 \times (1 - v^2)} \qquad [3.1]$$

where the geometrical properties w and A are the width and the area, respectively. v is the poisson ratio, and E is the actual modulus of elasticity.

Summation of energies of all lattice element forces gives the total elastic energy stored in the domain. While EA was taken as 1 for the unit deformation field, energy stored in a single truss member is expressed as

$$Energy_{OLM} = \frac{N^2 \times L}{2} \qquad [3.2]$$

where element force is represented with N and length of it is represented with L. Accordingly, EA_t is obtained as the ratio of the total energy calculated analytically [3.1] to the total energy stored in the analog lattice model.

$$EA_t = \frac{\text{Energy}_{\text{original}}}{\Sigma\ \text{Energy}_{\text{OLM}}} \qquad [3.3]$$

OLM is calibrated for the homogenized properties of concrete and it conveniently allows one to solve for the autonomous creation and propagation of cracks. Bonds are assumed to behave like truss elements, i.e., direction of force was along the direction connecting the nodes. As most practical problems faced in concrete mechanics involves tension and shear failures, bonds are assumed to be linearly elastic in compression and assumed to soften in tension. In this way, the number of parameters are kept to a minimum while providing a global match of the force-deformation response along with the crack propagation pattern for most practical problems.

Nonlinear tension softening part is assumed to be in the form of a stepwise linear softening function as shown in Figure 5. This shape is chosen only for convenience and other alternatives could be utilized as well. Concrete behavior in compression is assumed to be linearly elastic as none of the investigated problems failed due to concrete crushing. The input material properties needed for the overlapping lattice simulations are the modulus of elasticity (E_t), tensile strength (f_{cr}) and the fracture energy (G_F) are usually obtained from material tests depending on five constitutive model parameters which are multipliers of tensile strength (b_1 and b_2) and critical strain (a_1, a_2 and a_3). Elements connecting both steel and concrete nodes (i.e. bonding materials) have to carry at least 70 % of tensile strength of the concrete to stop pullout steel from concrete (Figure 6).

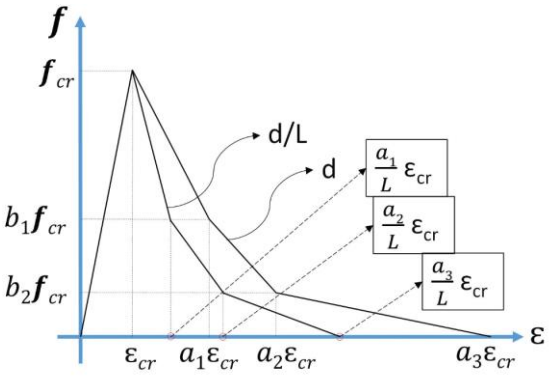

Figure 5. *Idealized constitutive model for concrete [Aydin et al., 2018]*

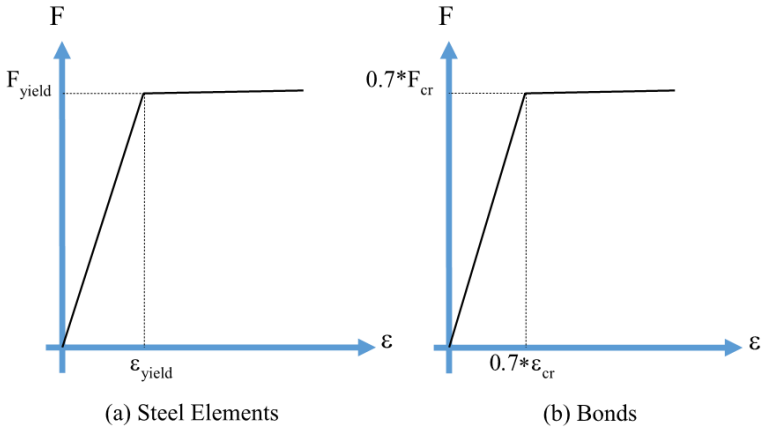

Figure 6. *Idealized constitutive models for steel and bond elements [Aydin et al., 2018]*

In Aydin et al. (2018), the calibration procedure for these material coefficients were provided in depth. Fracture energy was defined as energy dissipated per unit fracture area. When bond lengths were small, it was assumed that there is a single crack in each bond. Then, the area under force-deflection diagrams were forced to be same regardless of bond length. This required a normalization of force-strain diagrams so that area under the force-deflection diagram was constant for all bonds regardless of their lengths. In this case, a different lattice element having the same material properties but whose length was longer than d_s was addressed. The length of the lattice element (h) was considered to be sufficiently small, it was assumed that there is a single crack in each lattice element. The critical strain for all elements were taken as ε_{cr}. However, as the crack opened, the force carried by the crack was reduced, thus

reducing the deformation value of the region in the elastically acting region. In this case, the values of a_1, a_2, a_3 were calculated by Eq. 3.4 for the length of a lattice of h.

$$a_1' = \frac{b_1 \times (h - d_s)}{h} + \frac{a_1 \times d_s}{h}$$
$$a_1' = \frac{b_1 \times (h - d_s)}{h} + \frac{a_1 \times d_s}{h} \qquad [3.4]$$
$$a_3' = \frac{a_3 \times d_s}{h}$$

For instance, if the OLM horizon is selected as δ = 3.01d, there are six different element lengths (d, 1.41d, 2d, 2.24d, 2.83d, 3d). In Figure 7, sample stress-unit deformation curves are given for a_1, a_2, a_3, b_1, b_2 values which were 3, 40, 240, 0.6 and 0.2 respectively. When d_s = 0.005 m, d = 0.025 m, E_c = 35 GPa, ε_{cr} = 1.10e-04, w = 0.2 m values are used, the crack energy G_F value is calculated as 142 N/m. Element lines shown in the Figure 7 are obtained for their lengths in such a way as to decrease the area under them as their length increases. However, their total fracture energy contributions do not change as this area is multiplied by the total length of the element.

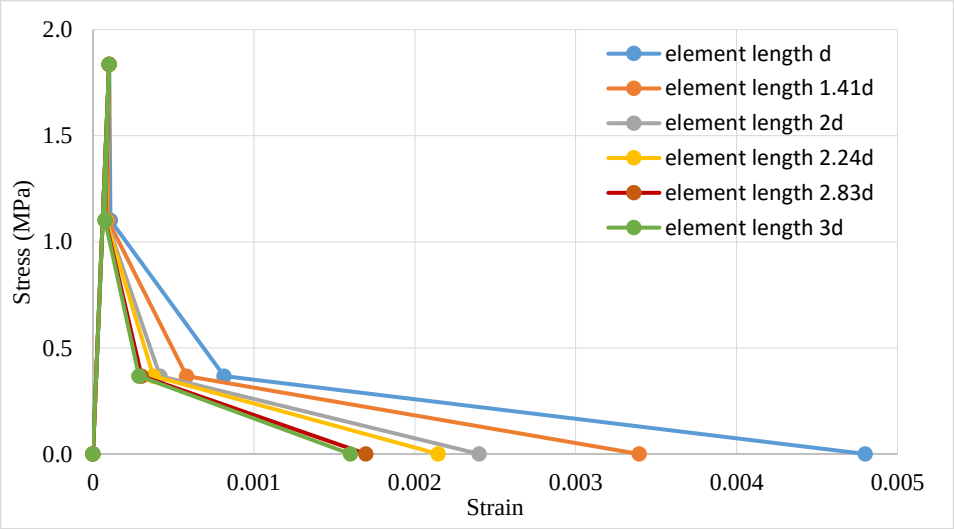

Figure 7. *Stress vs strain curves obtained by fracture energy normalization rule for lattice elements with six different length*

In previous versions of the OLM, the force - displacement behavior of the system modeled for the problems was investigated using the SLA - Sequentially Linear

Analysis solution algorithm proposed by Rots (2001) for mainly quasi-static effects. SLA is an easy-to-program approach that requires elastic analysis without any repetitions. It provides a solution to the snapback behavior that may occur in force-displacement curves. The results of the analysis included ups and downs due to the successive elastic analysis and the monotonic behavior was considered to be the envelope of the load-displacement curve (Aydın, 2017). However, for large systems with large horizon values, too many linear analyzes are required for convergence.

In this study, the OLM is used for the solution of nonlinear dynamic problems, explicit integration method is preferred instead of the implicit integration method to this end. Explicit integration makes it necessary to use relatively small time steps for a stable solution, but allows the modeling of nonlinear crack formation and propagation without any convergence problems. The well-known differential equation (equation of motion) used in dynamic analysis can be written as follows:

$$M\ddot{u}(t) + C\dot{u}(t) + Ku(t) = f(t) \qquad [3.5]$$

where M, C and K are the mass matrix, damping matrix and stiffness matrix respectively. u defines the displacement vector and f is the external dynamic force vector. For damping matrix, mass and stiffness proportional Rayleigh approach is preferred. ($C = \alpha M + \beta K$). For explicit integration, the algorithm proposed by Chung and Lee (1994) is preferred. The algorithm consists of the following steps:

1. Calculate diagonal M matrix and nonlinear internal force vector $N(u_0, \dot{u}_0)$

$$N = f - Ku - C\dot{u}$$

2. Calculate the initial values of u_0, $\dot{u}_0$, $N(u_0, \dot{u}_0)$, f_0 and $\ddot{u}_0$

$$\ddot{u}_0 = \left(f_0 - N(u_0, \dot{u}_0)\right)$$

3. Select the integration parameter β value ($1 < \beta \leq 28/27$) and appropriate time step Δt , then calculate the following specified parameters

$$\beta_1 = \Delta t^2(1/2 - \beta)\,, \quad \beta_2 = \Delta t^2(\beta), \quad \gamma_1 = -\Delta t/2\,, \quad \gamma_2 = 3\,\Delta t/2$$

4. Calculate the following values for each step

$$\ddot{u}_{n+1} = M^{-1}(f_n - N(u_n, \dot{u}_n))$$
$$u_{n+1} = u_n + \Delta t\dot{u}_n + \beta_1\ddot{u}_n + \beta_2\ddot{u}_{n+1}$$
$$\dot{u}_{n+1} = \dot{u}_n + \gamma_1\ddot{u}_n + \gamma_2\ddot{u}_{n+1}$$

5. Go to the next time value, n = n + 1 and repeat first four steps until the simulation is complete.

This method is efficient particularly for non-linear dynamic analyses with the proper selection of the β value.

Although explicit integration is a better choice for nonlinear dynamic problems, it is not suitable for simulations of experiments performed under displacement controlled and/or slow loading speeds. To tackle this problem, PID control loop mechanism which takes its name from first letters of Proportional (P), Integral (I) and Derivative (D) was added to enhance the capability of explicit solution of the OLM. This control algorithm was previously applied to dynamic analysis of a concrete frame system and validated with experimental results (Kocamaz, 2018).

Continuous modulated control type enables to control by generating a signal to the output according to the error difference. A PID controller compares signal of measured process variable (PV) with signal of desired set-point (SP). The difference between them is recorded as error. According to this error, the PID controller makes an impact by trying to minimize the error and sends it to the output. In this way, errors are determined with continuous feedback from output to input until the error is minimized, and the error is reduced by sending the controller effect to the output. Assuming that the desired change of the control parameter is determined as u (t) and the value from the model output is expressed as u_p (t), the difference between them gives the error at time t, e (t) = u (t) – u_p (t). The time variation of the external load F is controlled by an integral-differential equation as follows

$$\frac{dF}{dt} = K_p e + K_i \int_0^t e dt + K_d \frac{de}{dt} \qquad [3.6]$$

where K_p, K_i and K_d are the proportional, integral and derivate parameters respectively. K_p parameter produces proportional control and monitors output. The K_i parameter controls the accumulation of errors and increases the amount of static accuracy at the risk of error in the dynamic response. K_d increases dynamic behavior and forces a return according to the rate of change of the error. This equation is solved in the OLM simulation at the same time in each step taken in time and the F value is updated. When behavior changes from linear to non-linear, the time-dependent derivative of F starts to take negative values and this ensures that the softening behavior is correctly modeled.

OLM analysis engine with the PID control was tested and validated with experimental results before being applied to tunnel simulations. Although results are very close to experiments, the solution time of OLM is greatly increased if a large number of nodes and elements are used. Results obtained from simply reinforced concrete beam tests are presented in section 3.2.

An approximate method which is similar to the sequentially linear analysis (SLA) solution algorithm was developed to decrease computational time in quasi-static simulations. In this method, while load is increased in each step, every element exceeding the threshold tensile strength was softened according to the material model. Same procedure is repeated in each step. Unlike SLA, method was not focused on a single element. Method is appropriate for force control systems and has no convergence problem. This provides an important advantage over the PID method. As the load increment decreases, accuracy of the solution increases. Validation study and comparative results are given in section 3.2.

3.2. Validation of OLM for a Simply Supported Reinforced Concrete Beam

Walraven (1978) performed a four-point flexural test of a reinforced concrete beam which had a height of 150 mm and a length of 2300 mm with 2Ø10 + 1Ø8 tension reinforcement and 25 mm bottom clear cover. The modulus of elasticity E_c and tensile strength f_{cr} values for concrete were taken as 25 GPa and 2.5 MPa, respectively. The modulus of elasticity E_s and yield stress f_y were taken as 210 GPa and 440 MPa, respectively, for steel. External force was applied 600 mm away from both ends of the beam and the deflection was measured at the middle point of the beam. Geometry of the beam is shown in Figure 8.

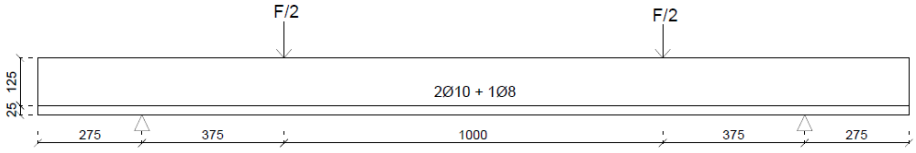

Figure 8. *Four-point beam bending experiment [Walraven, 1978]*

Reinforced concrete beam was simulated with 2405 nodes, 30124 elements, a grid size of d = 12.5 mm with 3.01d horizon (δ). Elastic-softening based force displacement models was employed to this study as multipliers of strain (a_1, a_2 and a_3), and critical force (b_1 and b_2) were taken as 3.1, 30, 200, 0.6, 0.2 respectively. These values correspond approximately to a fracture energy G_F = 68 N/m. Elements between steel and concrete nodes were assumed to have a strength of $0.7f_{cr}$ and show an elastoplastic behavior as suggested by Aydin et al. (2018). First, the parameters of the PID solution algorithm integrated to the OLM model were calibrated as $K_p = 6 \times 10^9$, $K_i = 3 \times 10^7$ and $K_d = 1.35 \times 10^4$ for minimum error and oscillation. Then, the aforementioned approximate method was used as an alternative solution algorithm. In order to minimize the computational error, after the evaluation of different load increments shown in Figure 9, lowest load increment that provides reasonable computational time, 0.1 kN per step was used. The comparison of the measured and computed deflections as a function of the applied load is given in Figure 10 showing an excellent match. While analysis with PID solution algorithm lasts almost a day, analysis with

approximate method takes at most an hour with the same personal computer. This shows the superior performance of approximate method with a reasonable accuracy.

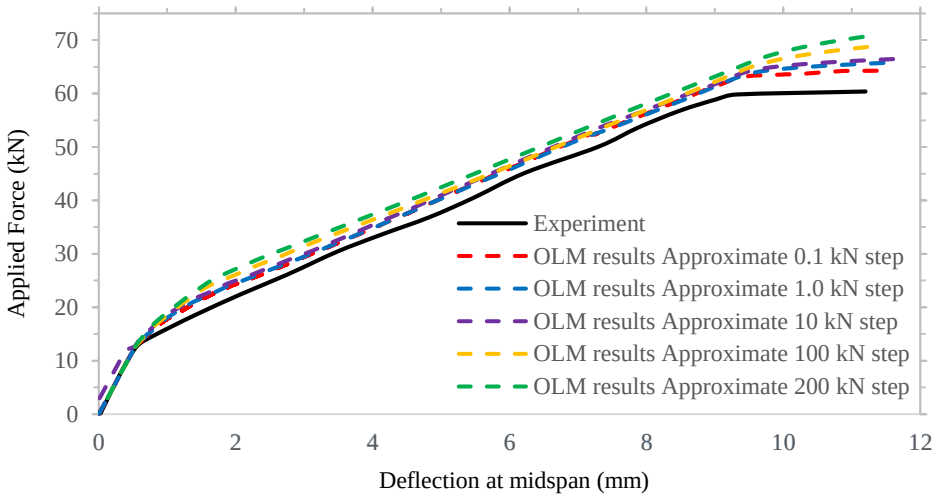

Figure 9. *OLM computed force-deflection diagrams for different load increments*

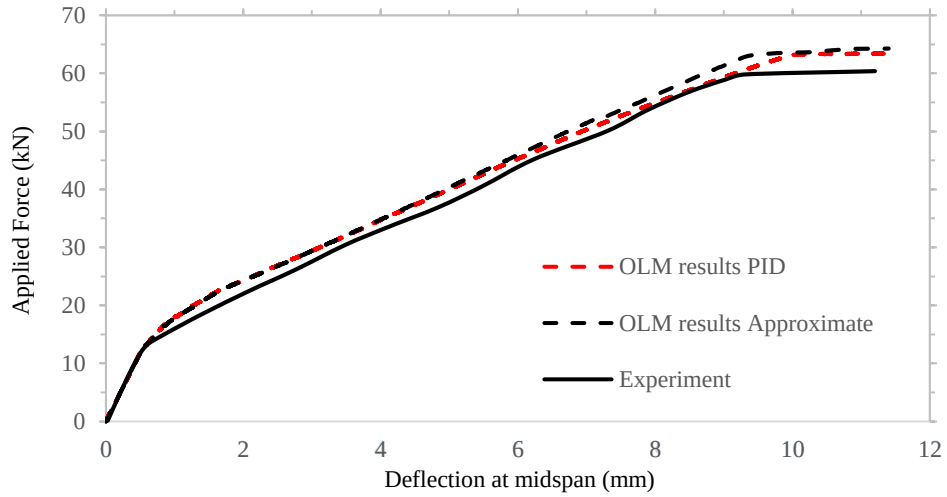

Figure 10. *Experimental and OLM computed force-deflection diagrams*

Figure 11 and Figure 12 illustrate both OLM PID and OLM approximate predicted damage patterns. More validations of OLM for plain concrete and reinforced concrete structural elements were documented in Aydin et al. (2018).

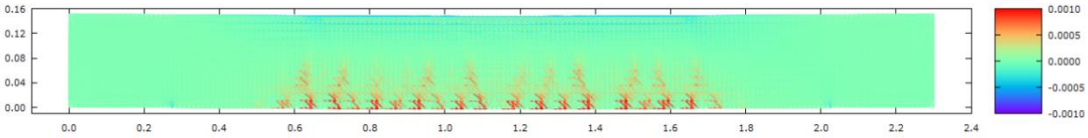

Figure 11. *Damage pattern for 2.5 mm mid span deflection (OLM PID). Color contours shows normal strain*

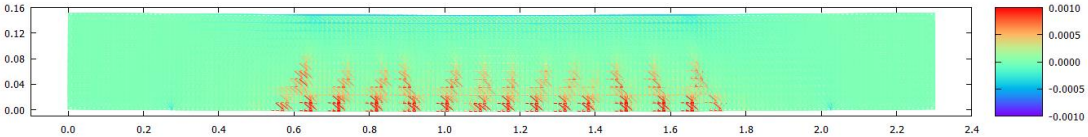

Figure 12. *Damage pattern for 2.5 mm mid span deflection (OLM Approximate). Color contours show normal strain*

3.3. Validation of OLM for a Steel Fiber-Reinforced Concrete Beam

To increase the ductility of concrete exhibiting brittle behavior under tension, one of the preferred methods is to use steel and synthetic fibers. It is frequently used in tunnel linings, shotcrete and retrofit applications. In this study, simply supported beam test results were used to evaluate the performance of steel fiber-reinforced pressure tunnel linings, to obtain the most suitable fiber concrete mixture ratios for linings design and to calibrate OLM parameters. The experiments were performed by Sengun et al. (2016) in the Middle East Technical University Materials Laboratory. In the experimental study, four-point bending tests were performed with the samples of 150 mm x 150 mm x 600 mm (Figure 13). The concrete pressure strength values used in the experiments were reported in the range of 40-45 MPa. The modulus of elasticity of the fiber-reinforced concrete was measured as 37 GPa. Two different lengths of 30 mm (0.55 mm thickness) and 60 mm (0.75 mm thickness) fibers were used in the

experiments. Four-point bending tests were performed by taking these fiber dosages at 30, 60 and 90 kg/m^3. At the end of the experiments, the energy values calculated for the 25 mm beam deflection are given in Table 2.

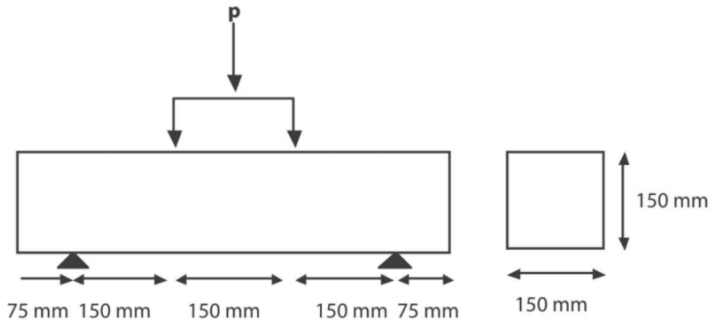

Figure 13. *Four-point bending test experimental [Sengun et al., 2016]*

The bending tests were modeled using the OLM analysis engine with 12.5 mm mesh, 637 nodes, 7820 elements and a 3.01d horizon (δ). The rate of change of the magnitude of the vertical force required for constant speed change of the vertical displacement of the midpoint of the beam in the OLM analysis engine was found using the PID control equation. Simulations were repeated at different speeds and the results were independent of speed. The vertical displacement velocity is taken as 0.001 m/s. The PID parameters were calibrated as $K_p = 10^9$, $K_i = 10^7$ and $K_d = 10^4$. An example OLM simulation results showing strain values of the elements which was obtained with a 30 mm long fiber, 30 kg/m^3 fiber dosage is given in Figure 14.

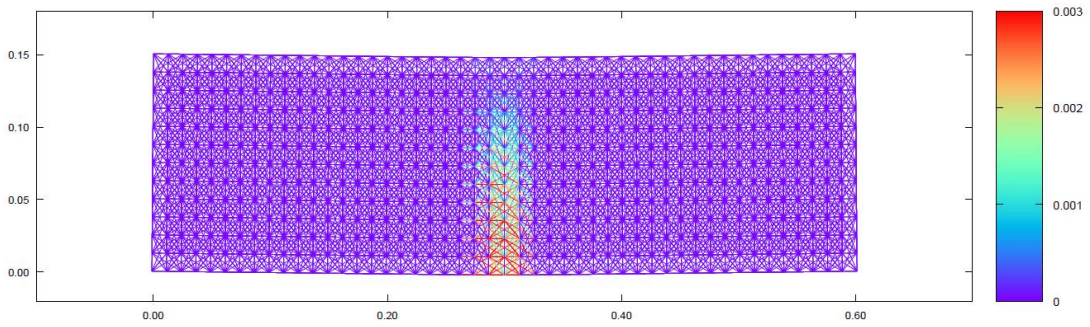

Figure 14. *Four-point bending test results obtained with the OLM (30 mm fiber, 30 kg/m^3)*

OLM total force-displacement curves are compared in Figure 15 with experimental results for different lengths and dosages. The parameters, calibrated with curve-fitting method, used in the OLM material model and G_F values corresponding to these parameters are given in Table 2. OLM curves are very close to experimental curves except for the inconsistency in experimental results using 60 mm long fibers with 30 kg/m^3 fiber dosage (60 kg/m^3 and 90 kg/m^3 results were almost the same).

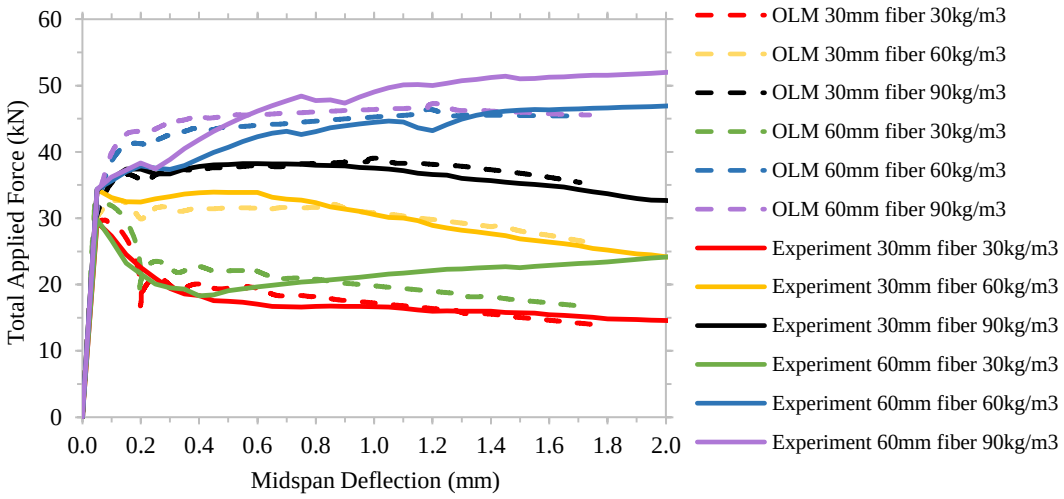

Figure 15. *Experimental vs OLM results for steel fiber-reinforced concrete beams*

Table 2. *OLM parameters and fracture energies for steel fiber-reinforced concrete*

Fiber Length	Dosage	Energy with respect to 25mm midspan deflection (N.m)	ε_{cr}	a_1	a_2	a_3	b_1	b_2	G_F fracture energy (N/m)
30 mm	30 kg/m^3	116462	0.0001	1	1500	5000	0.15	0.1	1260
30 mm	60 kg/m^3	201911	0.0001	1	2000	5000	0.25	0.2	2535
30 mm	90 kg/m^3	274158	0.0001	1	3000	5000	0.30	0.25	3630
60 mm	30 kg/m^3	496032	0.0001	1	2000	7000	0.13	0.5	6355
60 mm	60 kg/m^3	682444	0.0001	1	5000	15000	0.35	0.3	10570
60 mm	90 kg/m3	651541	0.0001	1	5000	15000	0.37	0.27	9971

3.4. Validation of OLM for a Synthetic Fiber-Reinforced Concrete Beam

Due to the corrosion problem that may be caused by the use of steel fibers in pressure tunnels, macro synthetic fibers were used as the second option in laboratory experiments. Identical tests on simply supported beams with macro synthetic fiber concrete performed by Sengun et al. (2016) were used for the calibration of the OLM parameters. The concrete compressive strength values used in the experiments were reported in the range of 40-45 MPa. The modulus of elasticity of the fiber concrete was measured to be 37 GPa. The modulus of elasticity of forta-ferro synthetic fiber used in the experiments, which has 54 mm in length and 0.677 mm in diameter, is in the range of 550 - 750 MPa. Detailed synthetic fiber properties are given in Table 3.

In OLM, same nodes and elements were used with same 12.5 mm mesh and 3.01d horizon (δ) as in steel fiber-reinforced simulations. The vertical displacement velocity is taken as 0.001 m/s same as steel fibers. The PID parameters were calibrated as $K_p = 10^9$, $K_i = 10^7$ and $K_d = 10^4$. OLM total force-displacement curves are compared in Figure 16 with experimental results for dosages of synthetic fibers. It shows that simulation results are fairly well agreements with the experimental data. The parameters used in the OLM material model and the crack energy values corresponding to these parameters are given in Table 4.

Table 3. *Synthetic fiber properties*

Tensile Strength	570-660 MPa
Length	54 mm
Material	Pure Copolymer
Melting Point	162-168 °C
Modulus of Elasticity	5.75 GPa
Quantity	220000 per kg
Surface Texture	Deformed
Acid / Alkali Resistance	Excellent

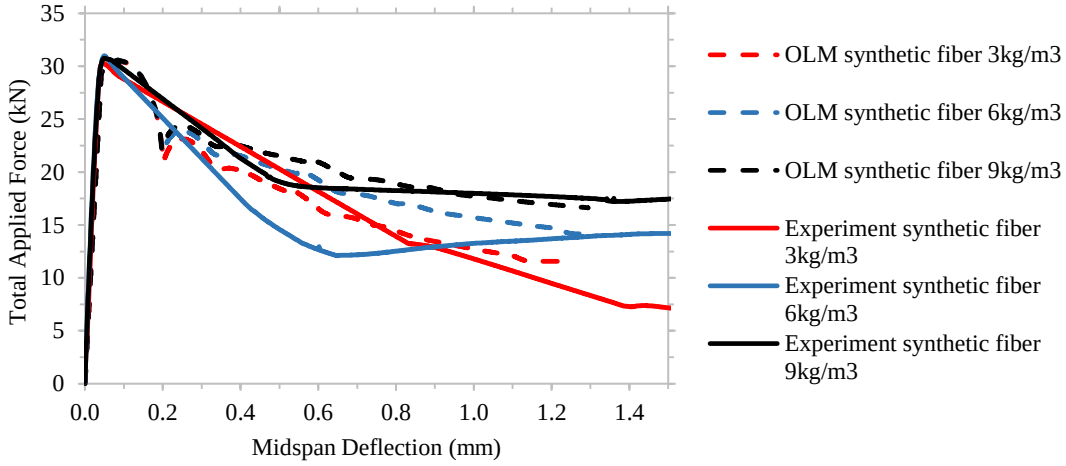

Figure 16. *Experimental and OLM results for synthetic fiber-reinforced concrete*

Table 4. *OLM parameters and the fracture energies for synthetic fiber-reinforced concrete*

Dosage	Energy with respect to 25mm midspan deflection (N.m)	ε_{cr}	a_1	a_2	a_3	b_1	b_2	G_F fracture energy (N/m)
3 kg/m^3	84402	0.0001	1	1000	5000	0.2	0.1	1184
6 kg/m^3	121392	0.0001	1	1000	8000	0.2	0.1	1691
9 kg/m^3	203878	0.0001	1	1000	12000	0.2	0.1	2367

3.5. Validation of OLM with Transparent Boundary Conditions

As the goal of the study is to analyze dynamic tunnel behavior placed in an infinite environment, new boundary conditions were required for proper absorption of the travelling waves. These boundary conditions are known as conductive / transparent / absorbing boundary conditions in the literature. In the transparent boundary condition approach, instead of using the original governing equation at the boundary, anti-reflection one-way wave equations are implemented to prevent wave reflection at the edges. The objective is to minimize the contamination in the numerical solution due to reflections. The simplest transparent boundary conditions for plane waves are implemented in the OLM. Transparent boundary condition is formulated in Eq. 3.7 as follows.

$$\begin{aligned} &\text{Shear Modulus} && G = \frac{E}{2 \times (1 + v)} \\ &\text{Bulk Modulus} && K = \frac{E}{3 \times (1 - 2 \times v)} \\ &\text{P –Wave Velocity} && V_p = \sqrt{\frac{K + {}^{4}/_{3} \times G}{\rho}} \\ &\text{Transparent Boundary Condition} && \frac{\partial u}{\partial x} = -\frac{1}{V_p} \times \frac{\partial u}{\partial t} \end{aligned} \qquad [3.7]$$

where E, v and ρ are the modulus of elasticity, poisson ratio and density respectively. u defines the displacement vector.

1D wave propagation in a uniform beam is used for the simulations of transparent boundary condition definition. The geometry used to check whether energy is dissipated properly in the boundary is shown in Figure 17.

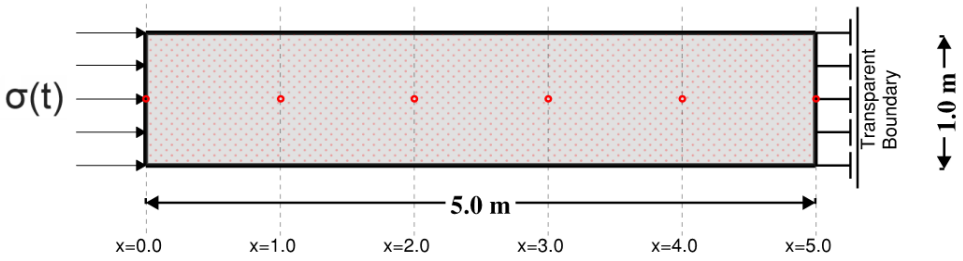

Figure 17. *Transparent boundary condition test study setup*

2121 nodes and 8120 elements were used in the model. The thickness was selected as 1 m and mesh size (d) was selected as 5 cm. Using the modulus of elasticity of concrete (E) as 25 GPa and Poisson ratio (v) as 0.33, shear modulus, bulk modulus and P-wave velocity were obtained as 9.4 MPa, 24.5 MPa and 3928.6 m/s respectively. External normal stress of magnitude 0.1 MPa load was applied as a short duration pulse as shown in Figure 18.

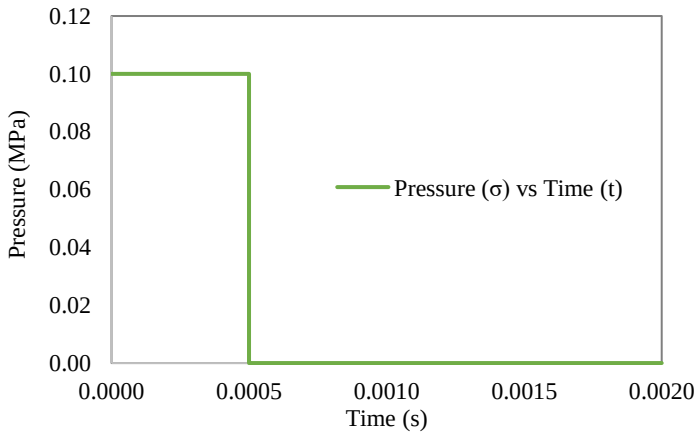

Figure 18. *Normal stress as a function of time applied on the test problem*

The displacements and velocities at 5 different points were tracked. The pressure wave travelled though the beam and radiated away at the transparent boundary; the model worked appropriately. In Figure 19, the displacements at the boundary are reported showing no reflection condition.

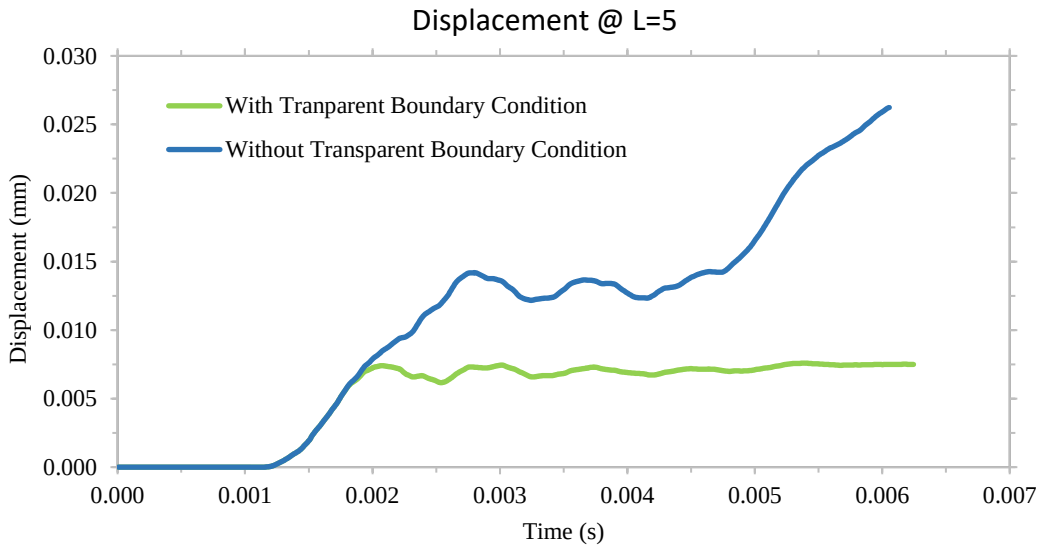

Figure 19. *Displacement vs time at L= 5 m*

CHAPTER 4

PRESSURE TUNNEL EXPERIMENTS

4.1. Summary of the Laboratory Experiments

Physical experimentation is a preferred way to gain insight and improve understanding of complex behaviors, supply data sets for developing and validating numerical models and testing proposed designs. As field experimentation does not seem to be feasible for pressure tunnels, laboratory experiments seem to be the only realistic choice. For this reason, a laboratory-based scaled experimental study focusing on the behavior of reinforced concrete tunnel linings was conducted at METU Structural Engineering Laboratory (Kalaycıoğlu, 2019). The testing programme consisted of seven different scenarios which were simulated with OLM. In all of the cases in this study, a reverse horse-shoe shaped lining was adopted from an existing pressure tunnel in Turkey (Topçam Dam, Ordu) with a scale factor of 0.4. The thickness of the laboratory model was 0.20 m. The thickness of the reinforced concrete lining was 16 cm on the laboratory corresponding to a 40 cm thick liner at real size. The setup was built horizontally on top of polytetrafluoroethylene and nylon sheets floor. Inner radius of the test apparatus was 72 cm. The surrounding rock media, which was planned to simulate weak rock conditions, was built in a special setup. In order to have an equivalent rock elastic modulus of approximately 8 GPa, two 5 cm thick concrete layers were designed to sandwich 10 cm thick autoclaved aerated concrete blocks. This composite rock substitute was built around the tunnel. There were also four screws connected to each aerated concrete block to work together to transfer loads as a shear key. For the low confinement case, this rock body outside the tunnel lining is approximately 1 meter thick in perfect decagon shape shown in Figure 28. The reinforcement of the concrete tunnel lining is given in Figure 20.

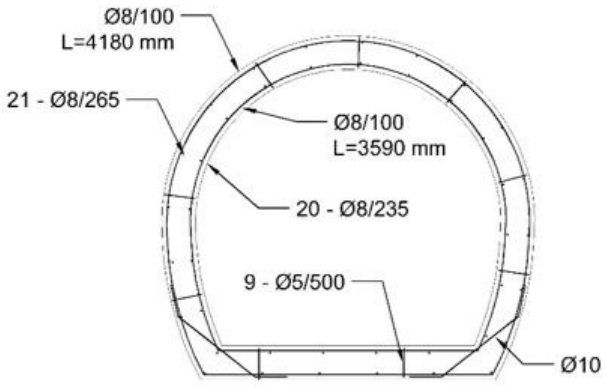

Figure 20. *Scaled reinforcement arrangement [Kalaycıoğlu, 2019]*

A novel loading system to simulate uniform water pressure to the inner walls of the tunnel lining was used in the program consisting of the hydraulic loading pistons (1) and load transfer steel plates (2) as shown in Figure 21. The system was designed to have a load capacity of each 300 kN in each direction. This capacity was sufficient to raise the internal pressure up to 1.30 MPa. Thin rubber sheets, 1 cm thick, were attached between these plates and the reinforced concrete lining to ensure uniform load distribution, in order to prevent concentrated point loadings due to rough concrete surface. In order to observe and measure the lining behavior better, the force in the pistons was increased by 10-20 kN in each step during the experiments. Details of the experiments were provided in Kalaycıoğlu (2019).

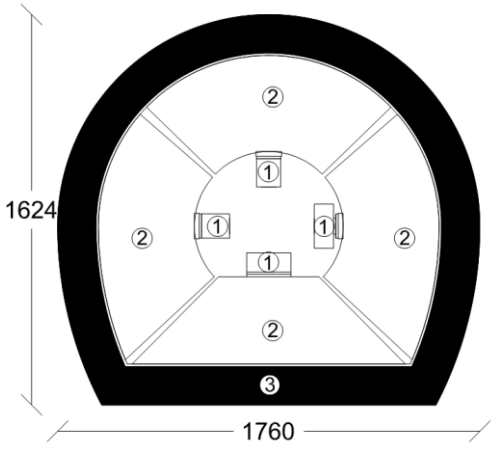

Figure 21. *Geometry of the loading system 1) loading pistons, 2) load transfer plates, 3) reinforced concrete tunnel lining*

Table 5. *Experimental and theoretical concrete properties*

Test Name	Material	Experimental Compressive Strength, fc (MPa)	Experimental Modulus of Elasticity, Ec (GPa)	Experimental Split Tensile Strength (MPa)	Theoretical Split Tensile Strength (MPa) $0.50\sqrt{fc}$	Correction Factor C $\frac{\text{Actual}}{\text{Thereotical}}$	Direct Tensile Strength, F (MPa) $C \times 0.35\sqrt{fc}$	Critical Strain, ε_{cr}	a_1	a_2	a_3	b_1	b_2	Fracture Energy, G_F (N/m)
1) No Confinement	RC	24.7	24.3	-	2.48	-	1.45	0.000060	5	80	300	0.6	0.2	45
2) Low Rock Confinement	RC	24.9	23.3	-	2.49	-	1.40	0.000060	5	80	300	0.6	0.2	41
3) Full Rock Confinement	RC	39.4	33.8	3.1	3.14	0.988	2.17	0.000064	5	80	300	0.6	0.2	70
4) Partial Rock Confinement	RC	39.4	33.8	3.1	3.14	0.988	2.17	0.000064	5	80	300	0.6	0.2	70
5) No Confinement	Fiber-RC	29.7	36.8	2.7	2.72	0.991	1.89	0.000051	1	1000	10000	0.2	0.1	527
6) Partial Rock Confinement	Fiber-RC	37.3	31.8	2.5	3.06	0.818	1.75	0.000055	1	1000	10000	0.2	0.1	530
7) Partial-Full Rock Confinement	Fiber-RC	37.3	31.8	2.5	3.06	0.818	1.75	0.000055	1	1000	10000	0.2	0.1	530

During concrete pouring stage of each experiments, cylindrical samples with a radius of 150 mm and height of 300 mm were prepared from same mixture in order to obtain compressive strength, split tensile strength and modulus of elasticity of concrete (Kalaycıoğlu, 2019). OLM requires the direct tensile strength of concrete. Due to challenges in the experimental determination of the direct tensile strength of concrete, split tensile strength was experimentally determined. Direct tensile strength was calculated using the relationship between the compressive strength and direct tensile strength ($0.35\sqrt{fc}$). Similarly, the split tensile strength was also calculated ($0.5\sqrt{fc}$). The direct tensile strength used in the simulations was calculated by correcting the estimate $0.35\sqrt{fc}$ with a correction factor (C) given by the ratio of the actual split tensile strength with the estimate of split tensile strength as indicated in Table 5.

4.2. Quasi-Static OLM Simulations of the Laboratory Experiments

4.2.1. First Experiment: No Confinement

This experiment was conducted to investigate the nonlinear behavior of tunnel in case of inadequate rock support outside the tunnel, which is frequently encountered in practice. The overall geometry of the experiment is shown in Figure 22. During the experiment, when the total applied force was around 100 kN (internal pressure 0.1 MPa), first cracks occurred in the lower right corner of the specimen. When the total applied force was around 375 kN (internal pressure 0.4 MPa), the cracks extremely widened and therefore the test was terminated. Vertical and horizontal expansions of the tunnel lining were reported in Kalaycıoğlu (2019). In vertical and horizontal directions, the relative displacements in the same directions coincided with the sum of absolute displacements showing that the measurements were consistent with each other. The similarity of the movement of the tunnel left and right shows that the experiment provided a symmetrical deformation state. Due to the reverse horse-shoe geometry, the tunnel lining deformed mainly downwards in the linear invert part expected.

Figure 22. *The setup of the first experiment with no rock confinement*

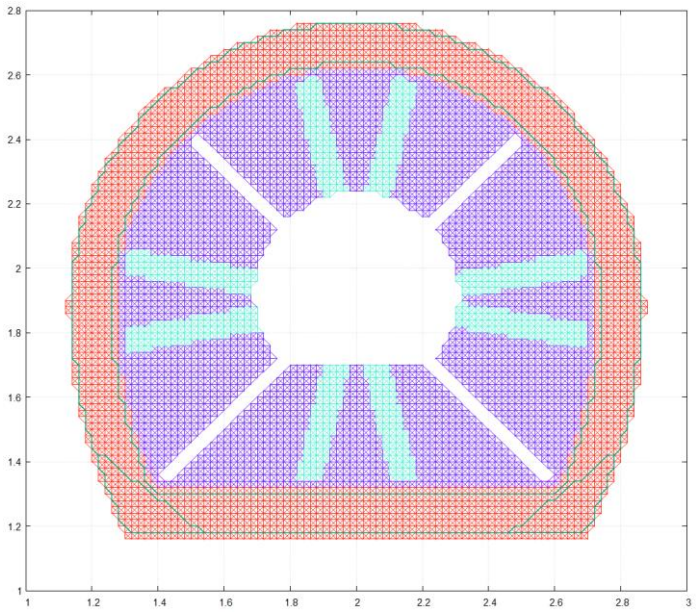

Figure 23. *OLM elements used in the modeling of the first experiment*

The experiment was simulated with 5341 nodes, 20531 elements and a horizon of 1.5d horizon (δ). The experimentally measured modulus of elasticity (24.3 GPa) was used for the concrete lining. The OLM parameters for the lining were ε_{cr} = 6e-05, a_1 = 5, a_2 = 80, a_3 = 300, b_1 = 0.6, and b_2 = 0.2. These values correspond approximately to a G_F value of 45 N/m (fracture energy). Tensile strength was taken as 1.45 MPa. In the

model, the modulus of elasticity of rubber was assumed to be 1 GPa. A low critical strain value ε_{cr} for the rubber was chosen to allow rubber to separate from the lining in the numerical simulations. The modulus of elasticity and yield strength of the reinforcement were 200 GPa and 420 MPa, respectively. The loading plates, local stiffeners on the plates, the rubber sheets between the plates and the interior of the tunnel lining, steel reinforcement and the tunnel lining are shown in the OLM model given in Figure 23. While velocity is kept constant as 0.001 m/s in simulation with the PID analysis method, maximum 20 kN force steps is used in simulations with approximate method.

Figure 24 and Figure 25 show comparisons of the numerical and experimental horizontal/vertical tunnel expansions for the PID analysis method and approximate method, respectively. The numerical results are close to the experiment except perhaps for the initial stiffness. Figure 27 shows the computed damage distribution for four different stages of loading. Predictions agree reasonably well with the experimentally observed cracks shown in Figure 26.

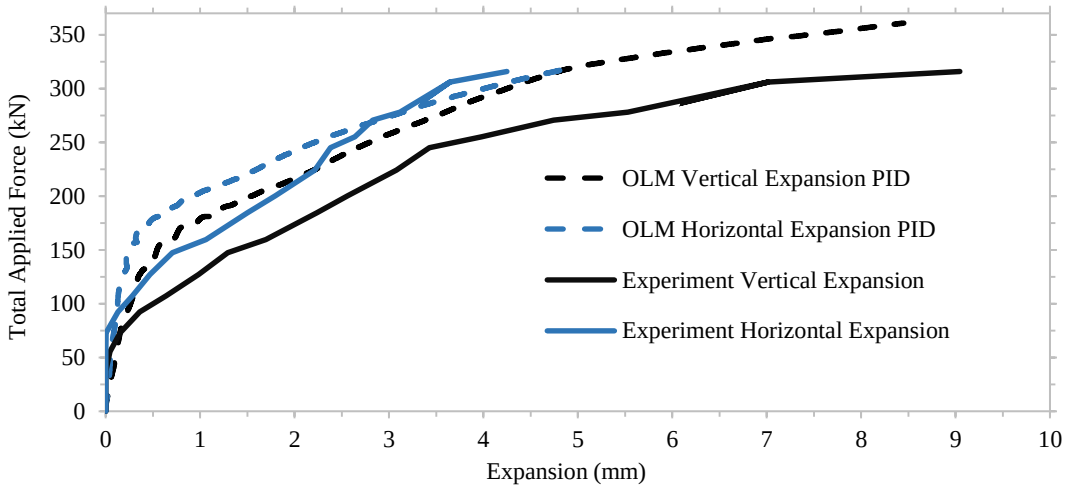

Figure 24. *Computed (PID Method) and measured tunnel expansions as a function of the applied load (total force is multiplied by 0.00107 to obtain the internal pressure in MPa)*

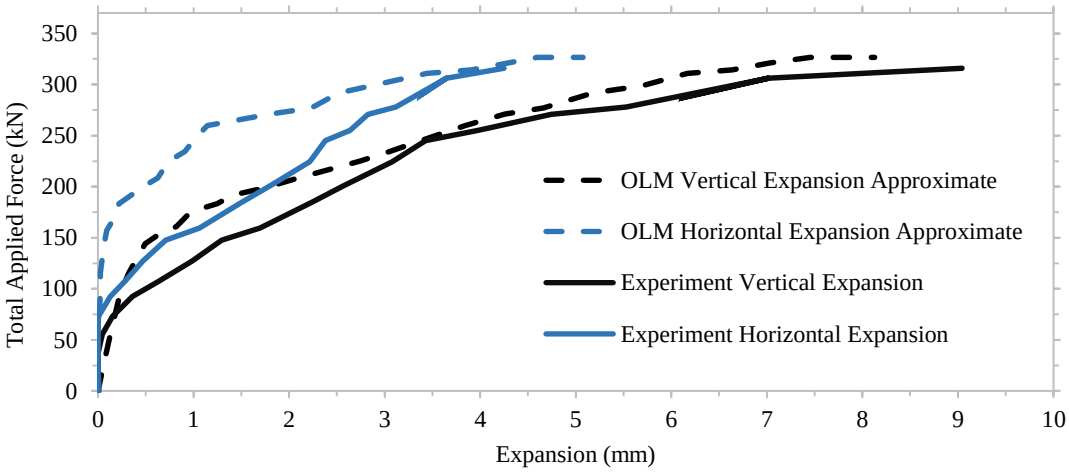

Figure 25. *Computed (Approximate Method) and measured tunnel expansions as a function of the applied load*

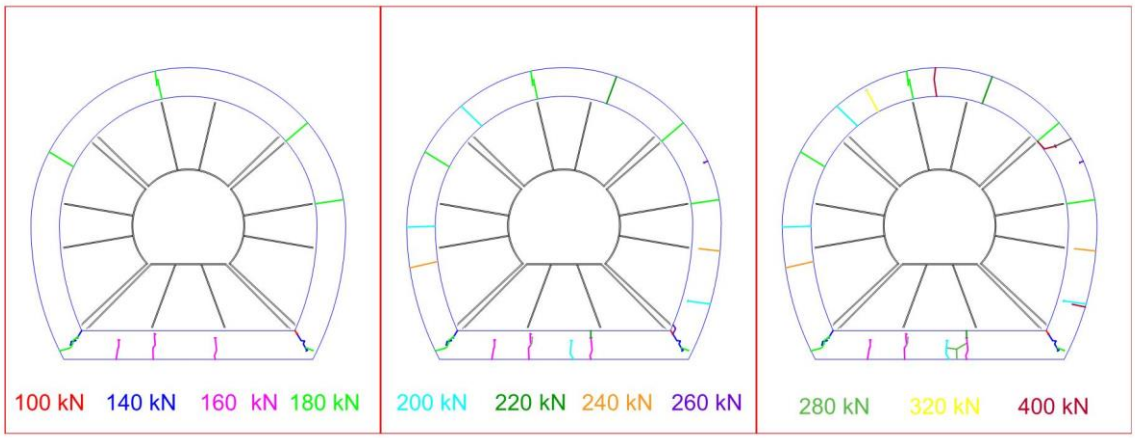

Figure 26. *Cracks observed in the first experiment [Kalaycıoğlu, 2019]*

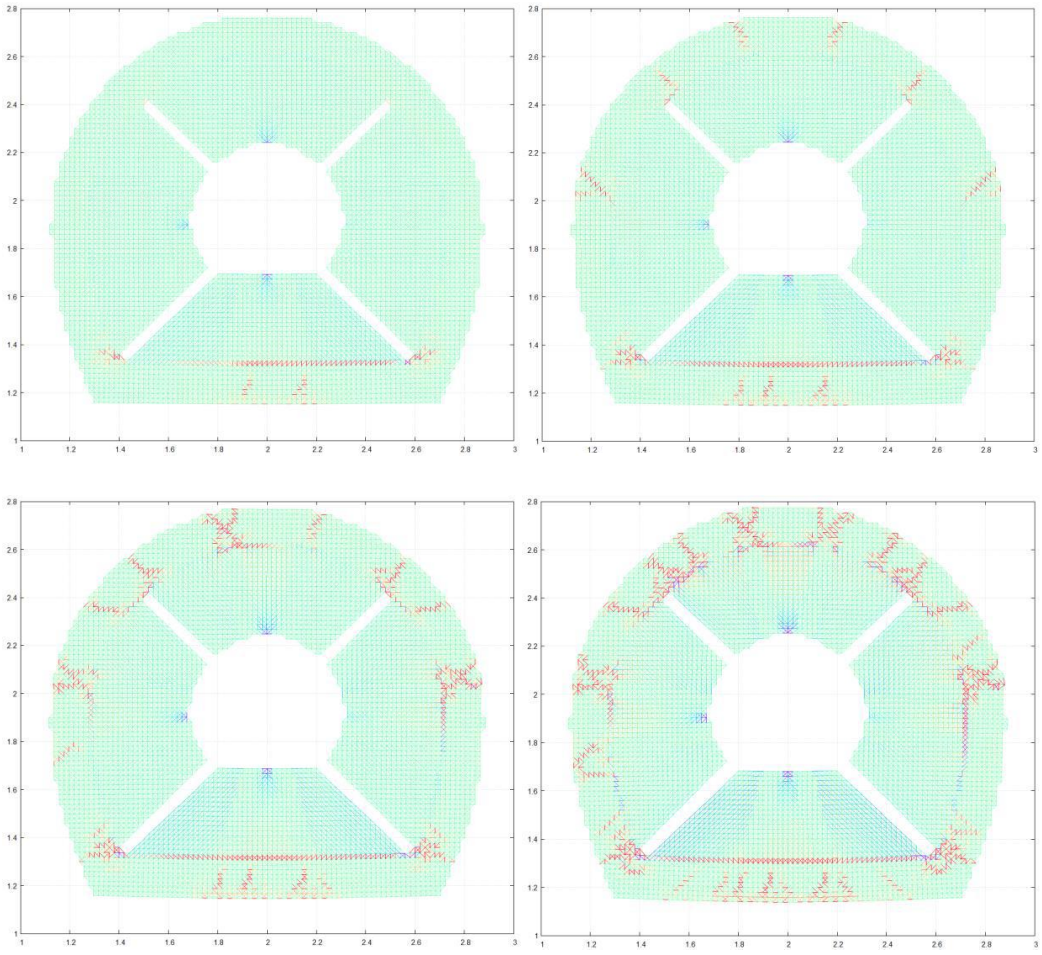

Figure 27. *Strain values when total applied force is 160 kN, 180 kN, 220 kN and 250 kN. Color scaled adapted to values between -0.0005 (blue) and 0.001 (red). (Approximate Method)*

4.2.2. Second Experiment: Low Rock Confinement

In this experiment, the tunnel lining was in continuous contact with the surrounding rock body; but in-situ confining stress was negligible. The overall geometry of the experiment is shown in Figure 28. During the experiment, the first crack was observed just outside the tunnel lining, when internal pressure value reached to 0.34 MPa. Confining stress vanished immediately after the crack reached the outside boundary. When the loading corresponded to an internal pressure of about 0.50 MPa, the test ended with an increase in the crack width and the rupture of the right lower reinforcement.

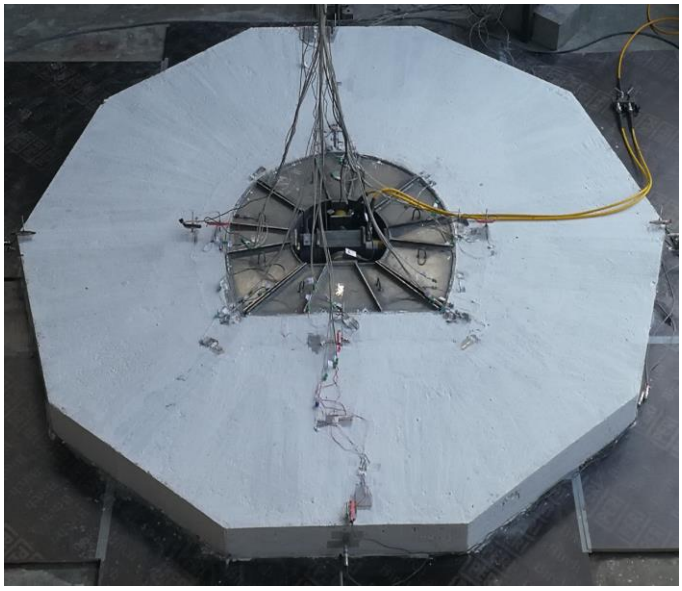

Figure 28. *The setup of the second experiment with low rock confinement*

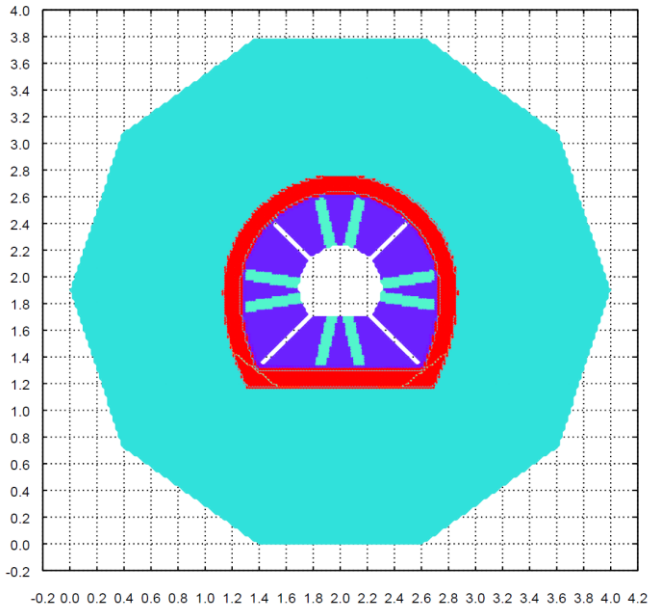

Figure 29. *OLM elements used in the modeling of the second experiment*

The experiment was simulated with 28582 nodes, 112986 elements and a horizon of 1.5d with the model shown in Figure 29. Modulus of elasticity was adjusted to 23.3 GPa and 8.37 GPa according to experimentally measured values for reinforced concrete and rock body respectively. The same OLM material parameters were used for the reinforced concrete corresponds to a G_F value of 43 N/m (fracture energy). OLM parameters for the rock body was ε_{cr} = 5e-05, a_1 = 10, a_2 = 30, a_3 = 40, b_1 = 0.6, and b_2 = 0.2 corresponding to a low fracture energy (3 N/m). Tensile strength was taken as 1.40 MPa for reinforced concrete and 0.42 MPa for the rock body. The modulus of elasticity and the yield strength of the reinforcement were taken as the same with the previous experiment. The experimentally observed 10% difference between applied forces in two orthogonal directions by the pistons was also considered in the numerical modeling studies.

Until cracking started, the rock body provided stiffness to the tunnel lining in the OLM model. With the initiation of cracking in the rock body as there were no confining in-situ stress, in the medium surrounding the tunnel was lost suddenly causing a brittle tunnel behavior. This was captured by the OLM as illustrated by the experimental and computed damage patterns shown in Figure 31.

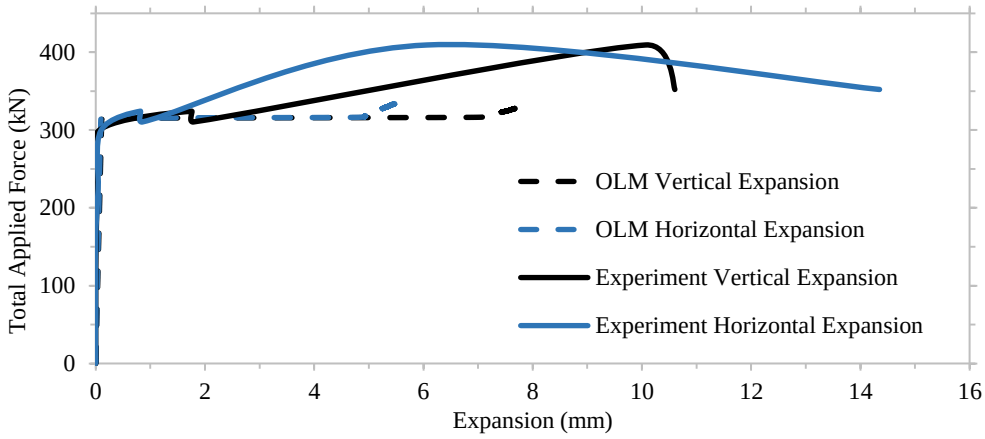

Figure 30. *Computed and measured tunnel expansions as a function of the applied load*

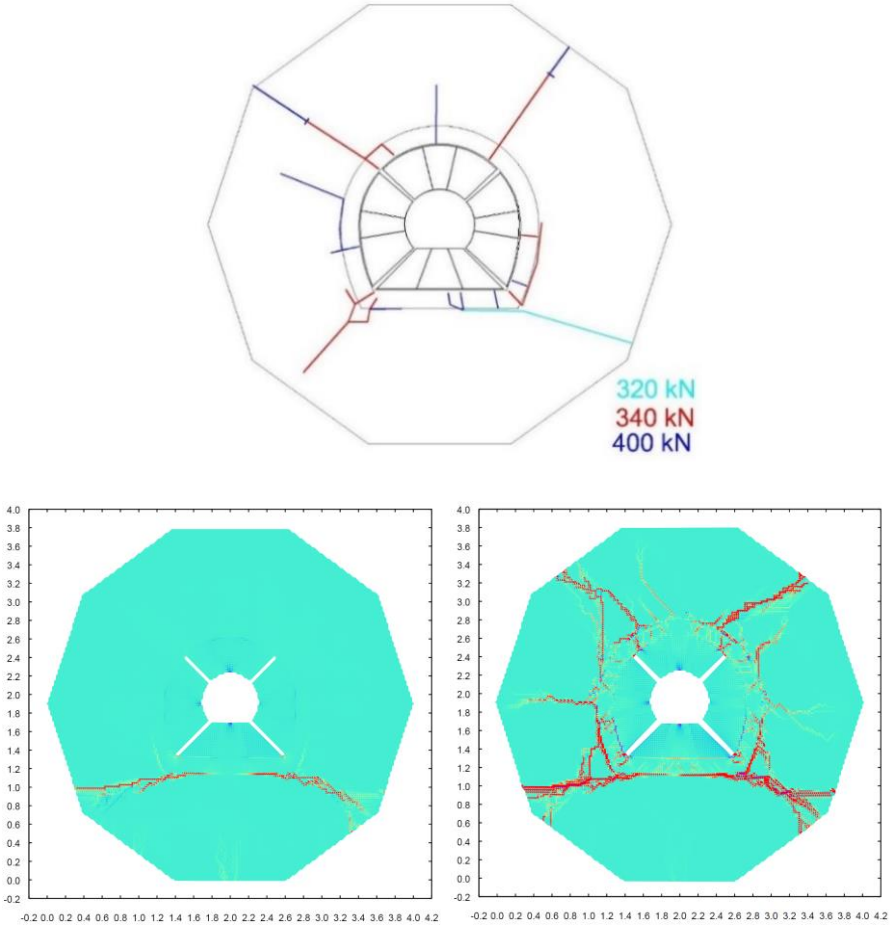

(a) (b)

Figure 31. *Observed and computed damage patterns for (a) 1 mm vertical expansion and (b) 8 mm vertical expansion*

4.2.3. Third Experiment: Full Rock Confinement

In this experiment, the tunnel lining was in perfect contact with the surrounding rock body. The goal of the test was to investigate the nonlinear behavior of tunnel lining under in-situ confining stresses. Confinement creates a compression field in the rock body which eventually stops crack propagation in the rock body. In-situ stresses were created using post-tensioned rock setup shown in Figure 32, (details reported by Kalaycıoğlu, 2019). Decagon rock shape used in the second experiment was converted into a rhombic shape to enable symmetrical post-tensioning application. In addition to the first and second experiments, this setup included post tensioning tendons (two tendons in each axis with 125 kN tension) corresponding to a soil depth of 60-100 m (horizontal and vertical confining stresses were assumed equal, $K_0 = 1$). Tendons were fixed to I-shaped HEA360 steel beams. Four reinforced concrete transition layers (beams) were placed between I beams and the rock substitute to prevent local crushing at the contact areas. The three-layer composite material was used on the inside of this concrete beam with screws (shear key) as it is in the previous experiment (Figure 32). No damage was observed on the rock substitute other than the local crushing of the transition RC beams adjacent to the steel beams.

Figure 32. *The setup of the third experiment with full rock confinement*

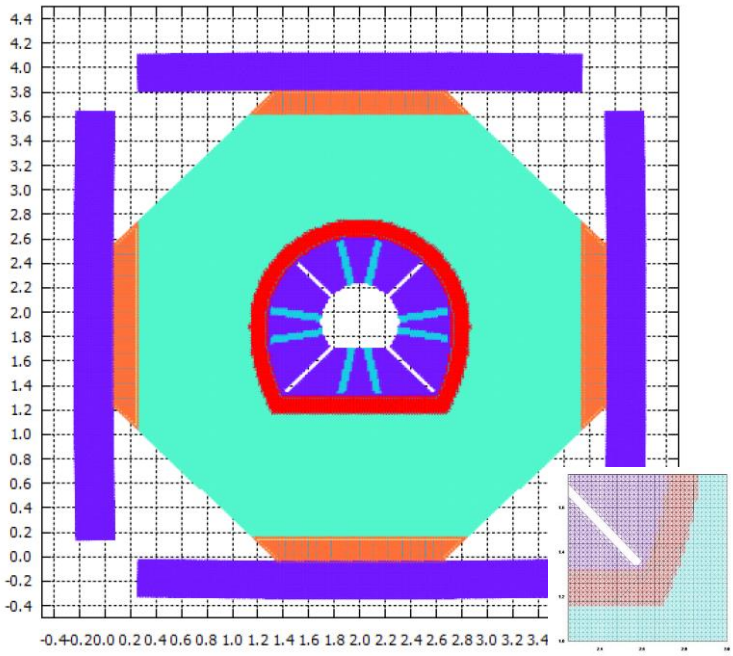

Figure 33. *OLM elements used in the modeling of the third experiment*

In the OLM simulations, six different materials (load transfer plates, concrete lining, rubber between load transfer plates and lining, rock body, 20 cm thick reinforced concrete layer between I beams and rock body, I beams) were used. Number of elements and nodes were 39638 and 155349, respectively while the horizon was selected as 1.5d. The experimentally measured modulus of elasticity (33.8 GPa) was used for the concrete lining. The parameters used in the OLM material model were ε_{cr} = 6.4e-05, a = 5, a_2 = 80, a_3 = 300, b_1 = 0.6, and b_2 = 0.2 for the lining and ε_{cr} = 5e-05, a_1 = 10, a_2 = 30, a_3 = 40, b_1 = 0.6, and b_2 = 0.2 for the rock layer. These values correspond approximately to G_F = 70 N/m and G_F = 3 N/m, respectively. Tensile strength was taken as 2.17 MPa. Modulus of elasticity of the rubber sheets was taken as 1 GPa same as the first two experiments. Post tensioning performed in the experiment was carried out in the first loading phase in the OLM analysis. The load transfer of each tendon was carried out via 4 OLM nodes in order to eliminate local stresses caused by the post tensioning effect at a single point. In addition, the tunnel lining was not allowed to take any load during the post tensioning stage (Figure 34).

There was no damage to the rock materials computed other than the local crushing of adjacent RC beam elements as shown in Figure 35. In the second phase, the experimental setup was loaded with perfect contact between the lining and rock body. As anticipated, pressure levels over 1 MPa was reached with no visible cracks showing the importance of the contact condition. The computed and measured tunnel expansions are compared for the vertical/horizontal directions in Figure 36. The numerical results are very close to the observed values for vertical expansions considering that experiment was almost in the linearly elastic range. In contrast, local stiffness changes are seen in the horizontal expansion curve that may be related with early cracks due to the uneven post tension application. Strain values and damage patterns for this test are shown in Figure 39 and Figure 38.

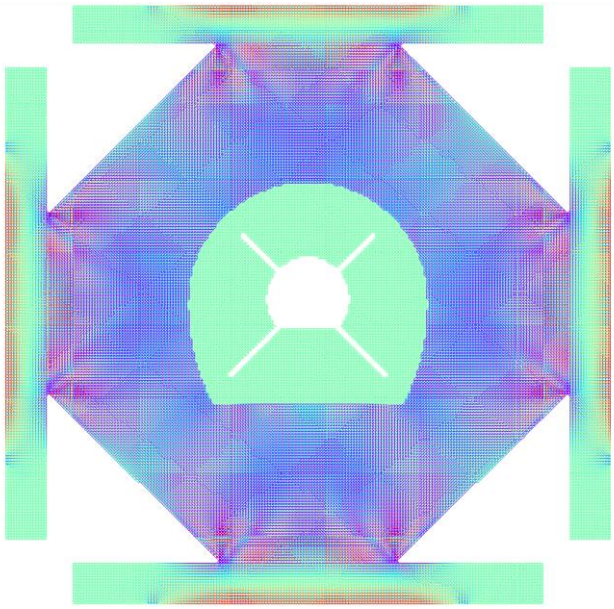

Figure 34. *Strains that occur after the post tensioning was completed. Color scaled adapted to values between -0.0001 (blue) and 0.0001 (red)*

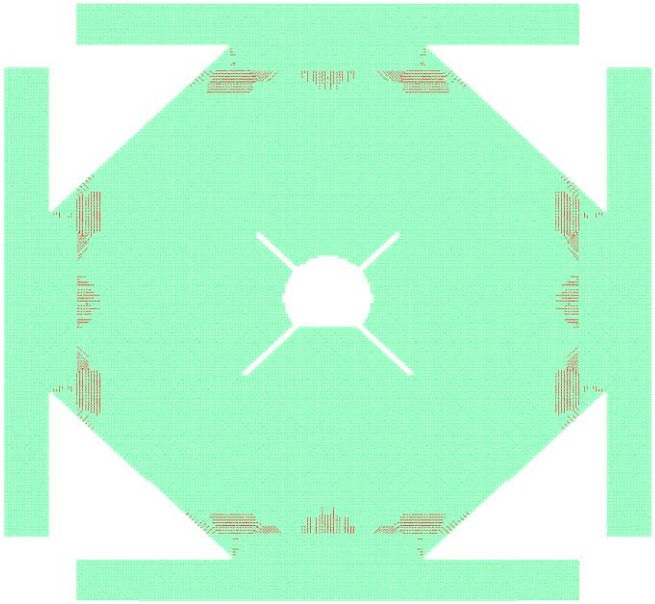

Figure 35. *OLM damage patterns after post tensioning*

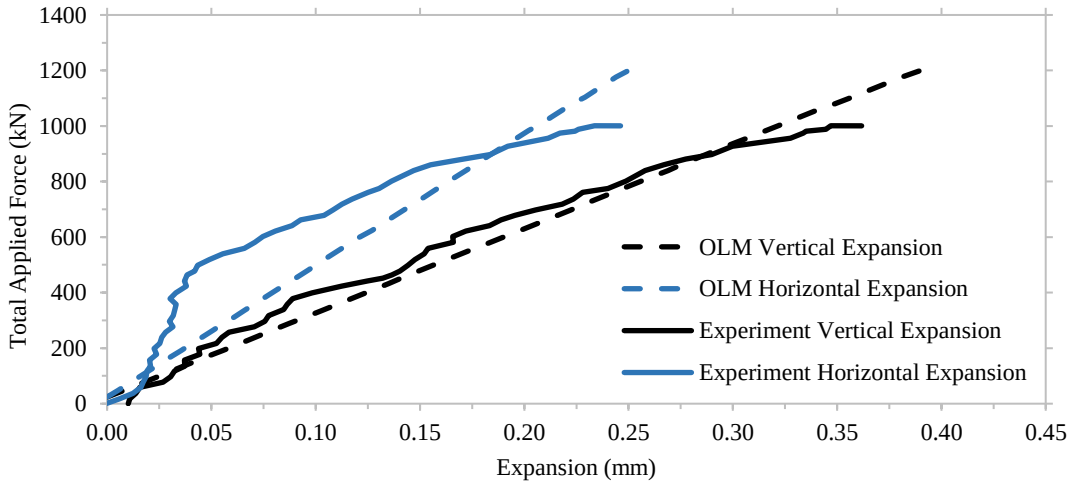

Figure 36. *Computed and measured tunnel expansions as a function of the applied load*

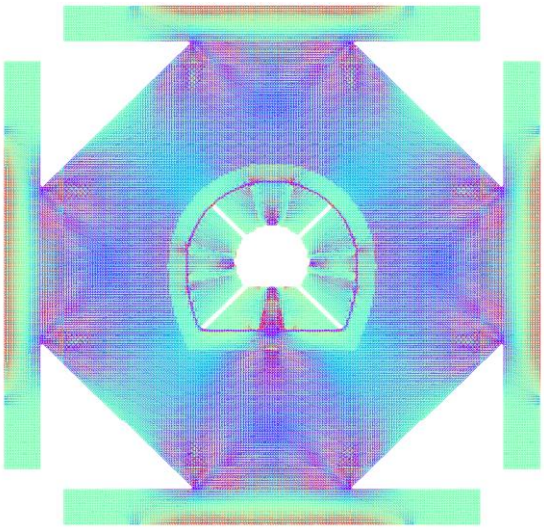

Figure 37. *Strain values when total applied pressure was around 1 MPa*

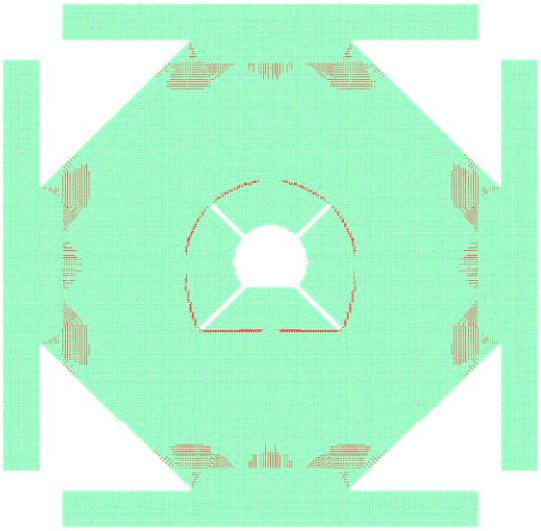

Figure 38. *OLM damage patterns*

4.2.4. Fourth Experiment: Partial Rock Confinement

In this experiment, a partial contact condition was obtained by creating a void between the tunnel lining and the rock body in order to evaluate the effects of local imperfections (Figure 39). Due to local loss of confinement in the tunnel, as expected, damage was seen mainly at locations where the contact was lost. During the

experiment, first cracks were observed when the internal pressure value reached 0.43 MPa. When the loading corresponded to an internal pressure of about 0.59 MPa, upon finding that the lining did not carry any more load and with rapidly increasing displacements, the experiment was ended.

Figure 39. *The setup of fourth experiment with partial in-situ confining stresses*

In OLM, six different materials were used as in the third experiment with a gap created by removing elements between the lining and the rock body (Figure 40). The parameters a_1, a_2, a_3, b_1, b_2 and b_3 used in the OLM material model and the calculated G_F crack energy were same as those used in the modeling of the third experiment. Post tension load (250 kN for each axle direction) was handled as in third experiment and the tunnel lining was kept free of loading during the first phase.

In post tensioning part (first OLM loading phase), no damage was shown other than same local crushing. Internal pressure was applied in the second loading phase. Experimentally measured and computed tunnel expansions in the vertical and horizontal directions are in good agreement as shown in Figure 41. The observed and computed damage patterns are provided in Figure 42.

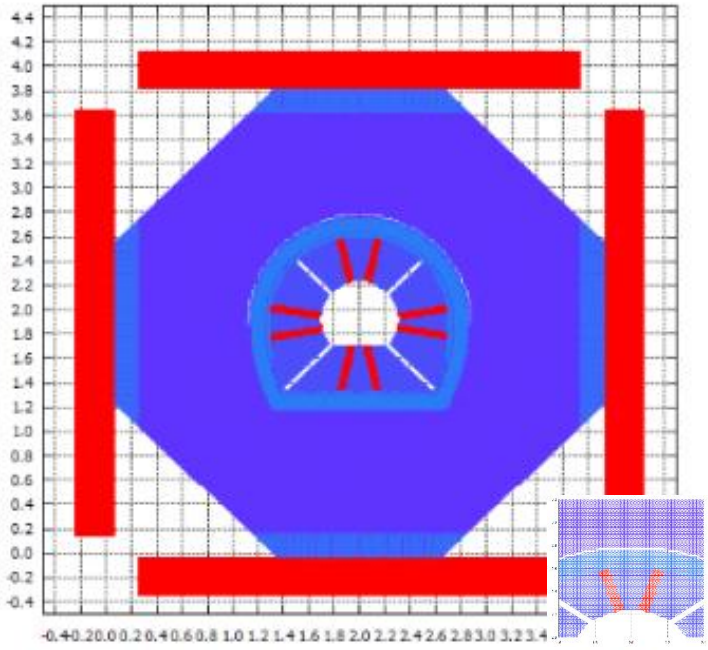

Figure 40. *OLM elements used in the modeling of the fourth experiment*

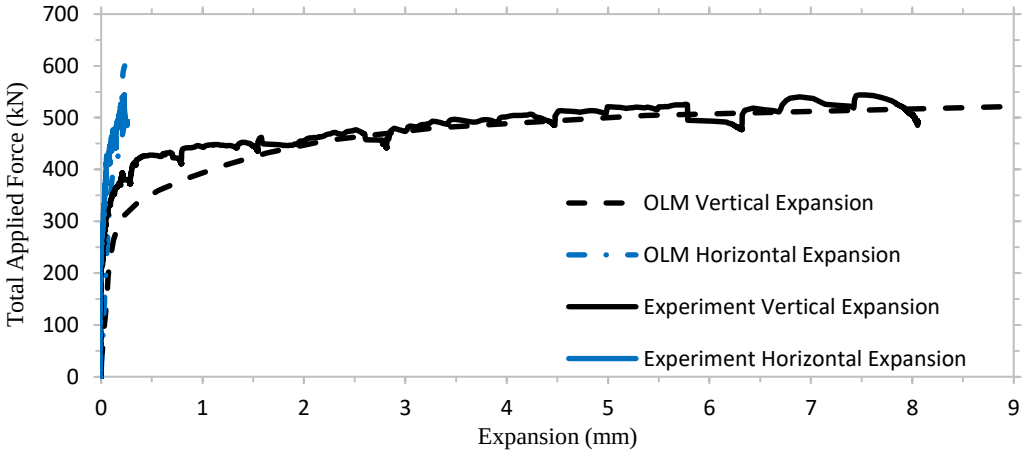

Figure 41. *Computed and measured tunnel expansions as a function of the applied load*

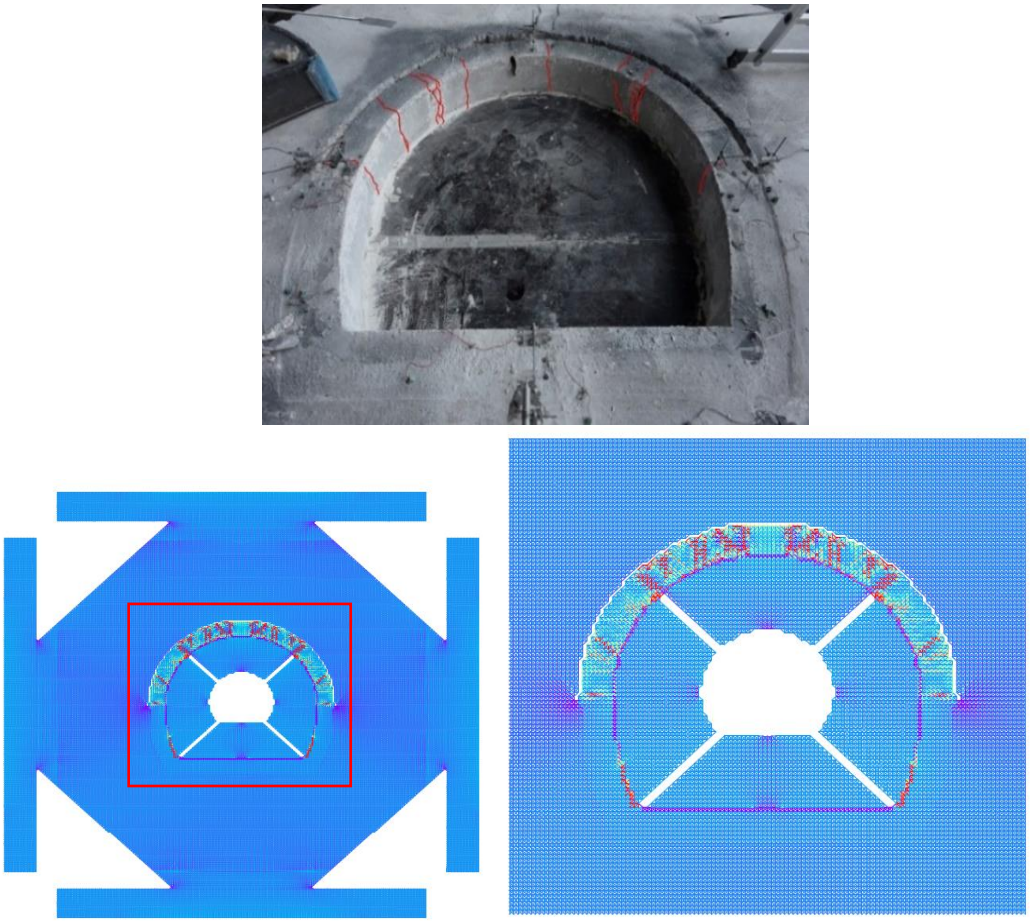

Figure 42. *Experimental and computed damage for the experiment with partial contact between tunnel lining and rock body under in-situ confining stresses. Color scaled adapted to values between -0.0005 (blue) and 0.002 (red)*

4.2.5. Fifth Experiment: No Confinement with Fiber-Reinforced Lining

This experiment is similar to the first experiment carried out without the rock support. The main difference between the two experiments is the addition of fibers and super plasticizer to the concrete mixture. The second important difference is that the loading plates are filled with concrete in order to increase the rigidity of the plates and lead to better uniform load transfer to the lining. The stiffness differences in the plates has thus been removed. The specific gravity of the fibers used in the experiment was

reported to be 910 kg/m^3. The tensile strength of synthetic fibers was reported as 570 MPa. As expected, the vertical expansion of the tunnel lining initiated prior to the horizontal deformation and increased faster than the horizontal expansion. The initial cracks were seen in the stress concentration zones when force was around 150 kN (internal pressure 0.16 MPa) at the right and left lower corners. Later, the cracks occurred in all directions of the lining and the distribution was relatively homogeneous (Figure 45). Similar to first experiment, it was seen that the bottom segment forming the lower part of the tunnel had a beam-like behavior.

The experiment was simulated with 5341 nodes, 20531 elements and 1.5d horizon as in the first experiment. The experimentally measured modulus of elasticity (36.8 GPa) was used for the concrete lining. In OLM model, according to simple beam tests, material model parameters were determined as ε_{cr} = 5.1e-05, a_1 = 1, a_2 = 1000, a_3 = 10000 and b_1 = 0.2, b_2 = 0.1 for 14 kg / m^3 macro synthetic fiber mixing ratio. These values correspond to a fracture energy (G_F) value of 527 N/m. Tensile strength was taken as 1.89 MPa. While loading plates, rubber sheets and steel reinforcements were used in exactly the same fashion with previous experiment, local stiffness changes of the loading plates were removed from the model since these plates were filled with concrete before this experiment as shown in Figure 43.

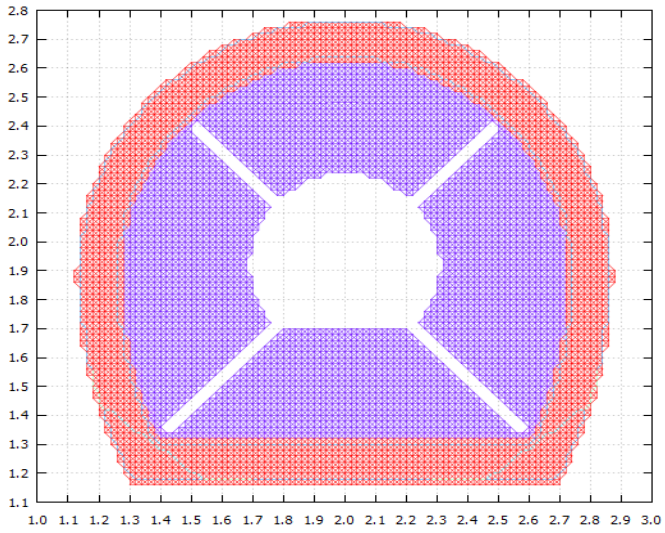

Figure 43. *OLM elements used in the modeling of the fifth experiment*

Figure 44 shows a comparison of the numerical and experimental horizontal and vertical tunnel expansion. The results of the simulations compare well with the measured displacements. When the numerical and experimental results obtained for this experiment are compared with the first experiment, it is understood that fiber-reinforced concrete helps to spread cracking along to the lining (Figure 45 and Figure 46). While maximum applied load is increased by around 15%, expansions are increased by 40%.

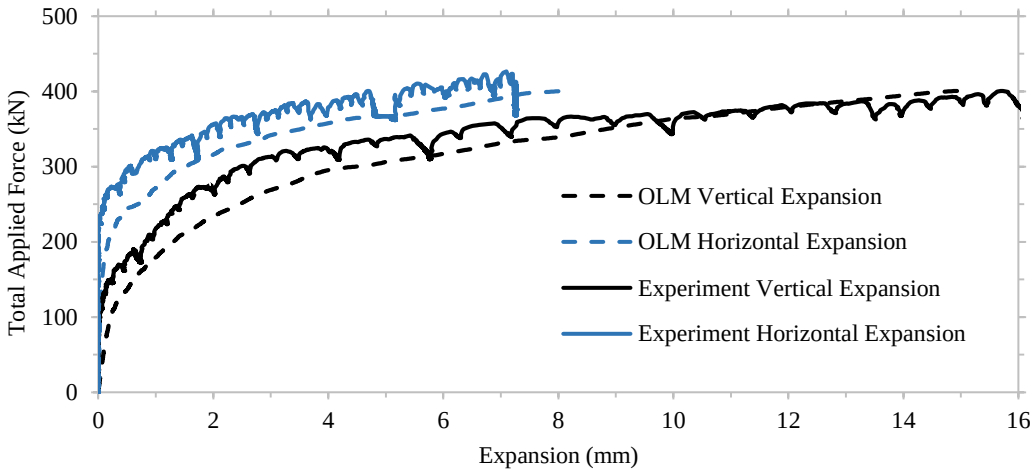

Figure 44. *Computed and measured tunnel expansions as a function of the applied load*

Figure 45. *Experimental damage pattern [Kalaycıoğlu, 2019]*

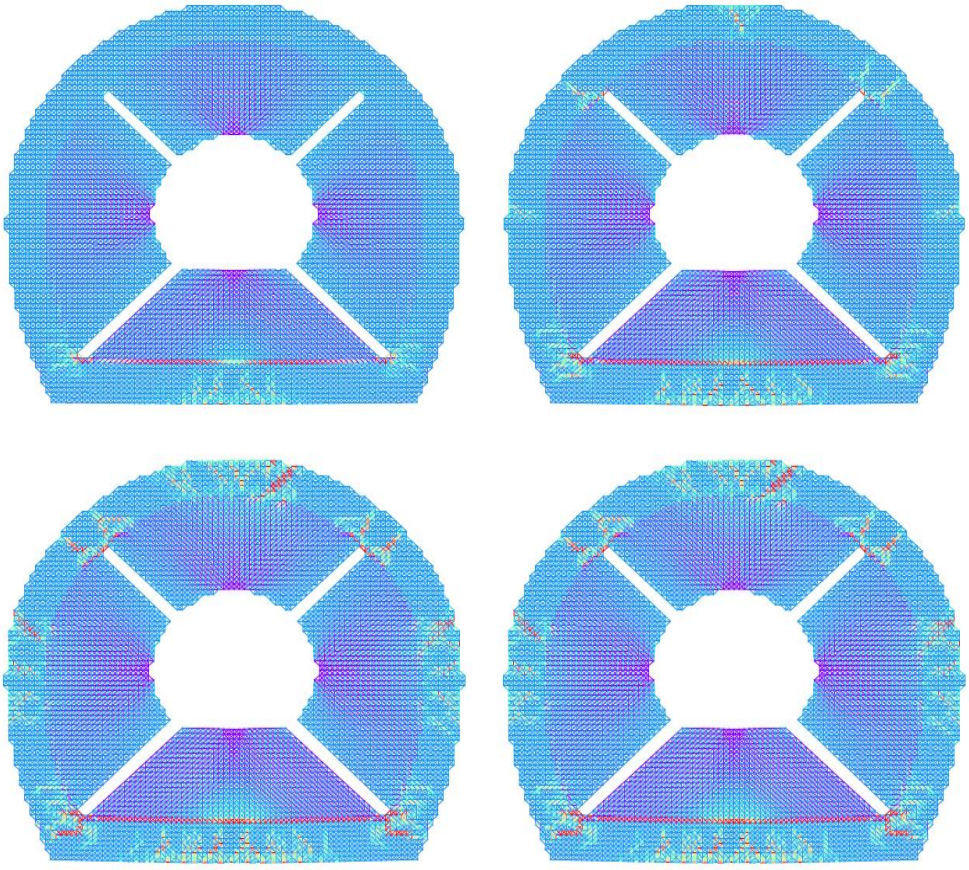

Figure 46. *Damage patterns when total applied force is 160 kN, 180 kN, 220 kN and 250 kN Color scale indicates strain of elements between -0.0005 (blue) and 0.002 (red)*

4.2.6. Sixth Experiment: Partial Rock Confinement with Fiber-Reinforced Lining

The sixth experiment, similar to the fourth, was conducted to examine the behavior of reinforced concrete lining in partial contact with rock under high field stresses. Fiber-reinforced concrete usage was the only difference from the fourth experiment. During the preparation of the experiment, an inner mold was formed similar to the previous ones. There was a rock layer outside of the lining, which was under tension with the post tensioning tendons. As in the fourth experiment, a gap was introduced between the upper side of the lining and the rock. Non-contact area was created by placing foams before concrete casting which was removed after casting the lining (Figure 47). Concrete mix was the same as those used in the fifth experiment. During the experiment, cracks in the stress concentration zones started almost simultaneously. The cracks began to wıden when the internal pressure was in the order of 0.3 MPa. When the internal pressure reached 0.65 MPa, crack widths increased extensively and the experiment was terminated.

Figure 47. *The setup of sixth experiment with partial in-situ confining stresses*

In OLM model, six different materials were used similar to those used in the fourth experiment. Similarly, a gap was placed between the fiber-reinforced lining and the rock medium at the top of the tunnel. The main difference between the two

experiments was the use of the material model considering the fiber and superplasticizer admixture added to the concrete mixture content. In this model, the material parameters of the OLM model obtained from the synthetic fiber-reinforced beam tests and used in fifth model were utilized (elasticity modulus E_c = 31.8 GPa, ε_{cr} = 5.5e-05, a_1 = 1, a_2 = 1000, a_3 = 10000 and b_1 = 0.2, b_2 = 0.1). These values correspond a fracture energy of G_F = 530 N/m. Tensile strength was taken as 1.75 MPa.

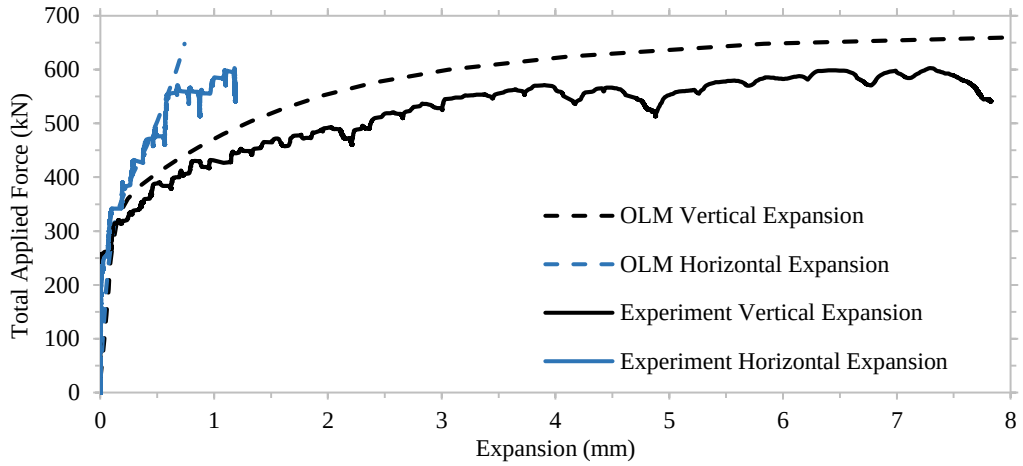

Figure 48. *Computed and measured tunnel expansions as a function of the applied load*

Figure 48 shows a comparison of the numerical and experimental horizontal and vertical length changes in the interior of the tunnel. It is seen that the results are quite close to each other. Although fibers do not change the tensile strength of concrete considerably, they provide a more ductile behavior after cracking. This leads to more frequent but narrower cracking. It can also be said that OLM results are similar to the results of the fourth experiment. When the numerical and experimental results obtained for this case are compared with the fourth experiment, it is seen that fibers spread the damage along the lining.

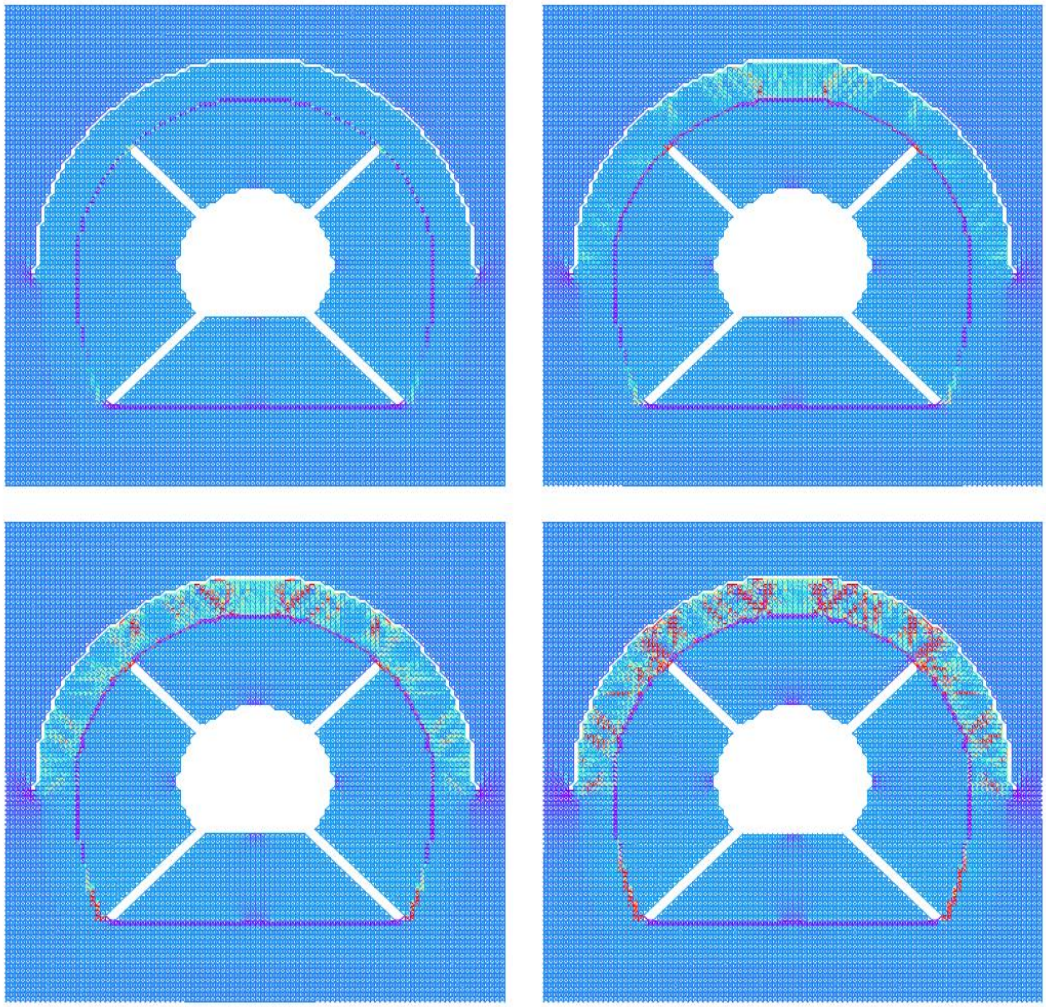

Figure 49. *Strains when total applied force is 200 kN, 300 kN, 350 kN and 450 kN. Color scaled adapted to values between -0.0005 (blue) and 0.002 (red)*

4.2.7. Seventh Experiment: Partial Contact-Full Rock Confinement with Fiber-Reinforced Lining

The last experiment was carried out to investigate the behavior of the reinforced concrete lining in partial contact with rock under high field stresses, similar to the fourth and sixth experiments. The difference from the sixth experiment is that the contact with the rock in both upper parts of the tunnel lining is partially achieved since additional concrete was poured as shown in Figure 50. Concrete mixing ratios were the same as those used in the fifth and sixth experiments. During the experiment, the

tunnel lining was loaded and unloaded to three different load levels (0.4 MPa, 1.05 MPa and 0.9 MPa). Due to the closure of the cracks observed in the first unloading cycle, only first loading cycle of the experiment was modeled with the OLM.

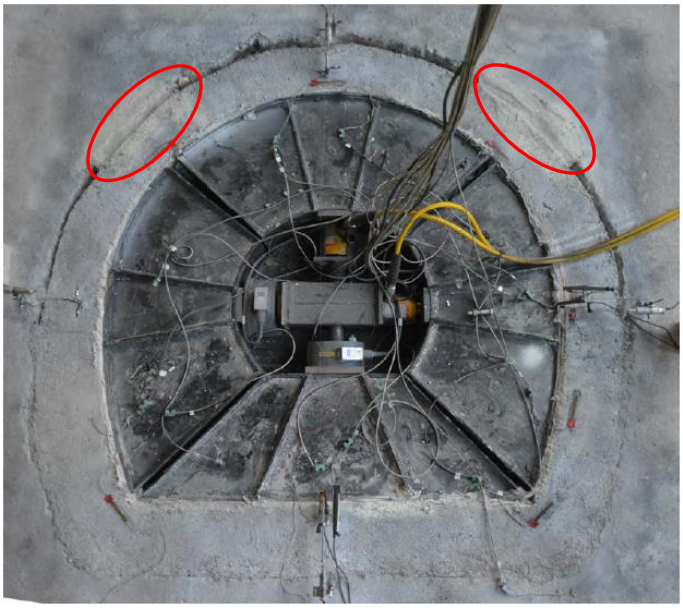

Figure 50. *The setup of the last experiment with additional concrete layers*

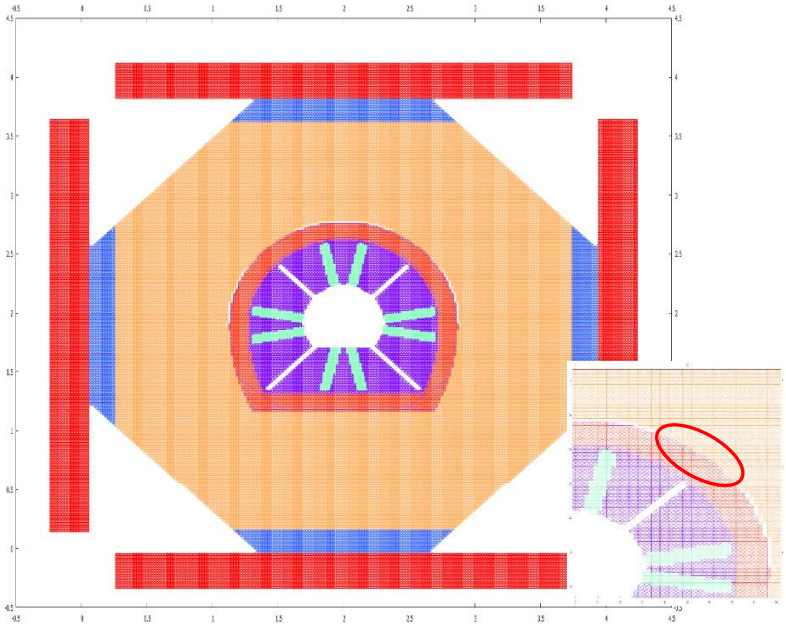

Figure 51. *OLM elements used in the modeling of the seventh experiment*

OLM simulation model for the final experiment included, similar to the fourth and sixth experiments, 6 different materials as shown in Figure 51. The main difference of this experiment from the sixth experiment was to provide increased rock interaction by adding concrete filling to a part of the cavity formed in the previous experiments. This fill layer was added to the model and analyzes were performed. For this layer, OLM material parameters were assumed as ε_{cr} = 5e-05, a_1 = 10, a_2 = 30, a_3 = 40 and b_1 = 06, b_2 = 0.2, similar to material parameters of rock body. The OLM material parameters for the lining were elasticity modulus E_c = 31.8 GPa and ε_{cr} = 5.5e-05, a_1 = 1, a_2 = 1000, a_3 = 10000 and b_1 = 0.2, b_2 = 0.1 corresponding to a fracture energy (G_F) of 530 N/m. Tensile strength was taken as 1.75 MPa.

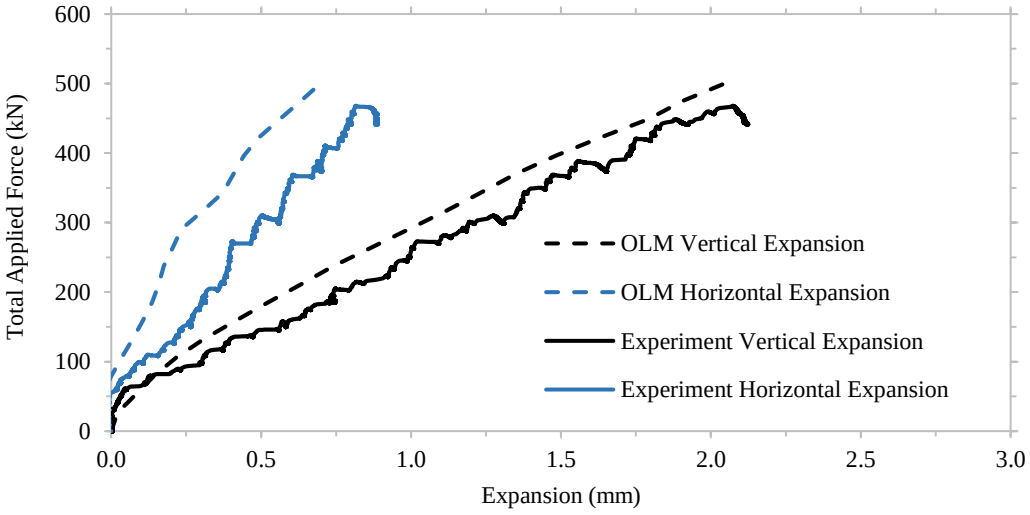

Figure 52. *Computed and measured tunnel expansions as a function of the applied load*

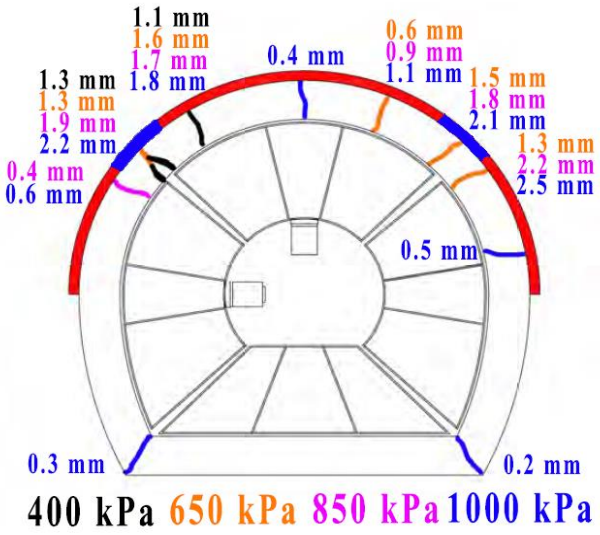

Figure 53. *Experimental damage pattern [Kalaycıoğlu, 2019]*

The horizontal and vertical tunnel expansions from the experiment are in good agreement with the OLM computed expansions (Figure 52). Figure 54 shows the damage distribution obtained from the simulation at four different values of total load. When OLM results and experimental results are compared, it is seen that the damage on the fiber-reinforced concrete lining is concentrated in the parts where rock contact is lost at the top (Figure 53 and Figure 54).

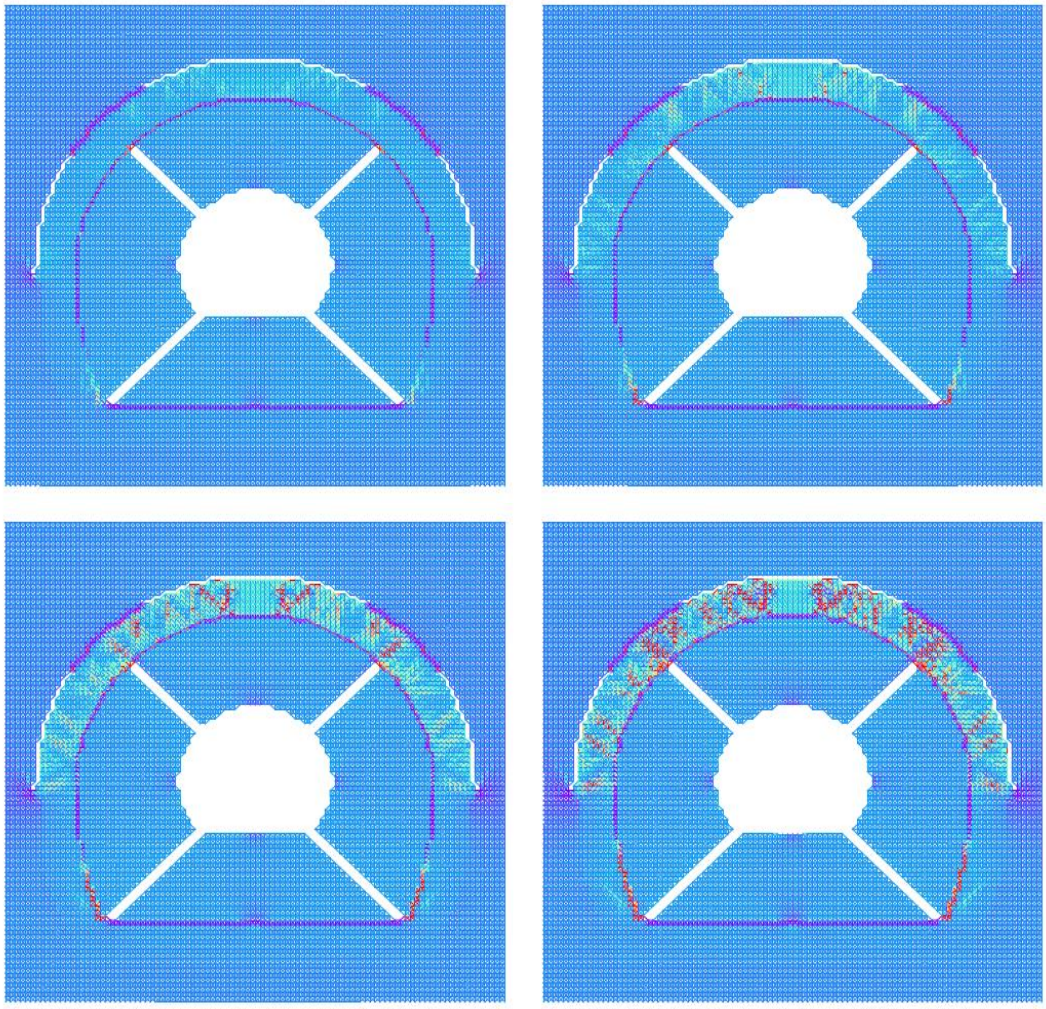

Figure 54. *Strains when total applied force is 200 kN, 300 kN, 350 kN and 450 kN. Color scaled adapted to values between -0.0005 (blue) and 0.002 (red)*

4.3. Dynamic OLM Simulations

In this part, behavior of pressure tunnels under dynamic loads is examined by using the OLM model calibrated and validated with the experimental results. Since it is not possible to carry out such experiments in the laboratory, numerical analysis seems to be the only way to comprehend the dynamic behavior.

While approximate method or PID control method given in Section 3.1 were used to solve quasi-static problems, explicit integration method is preferred to simulate dynamic behavior due to the difficulty in solving equilibrium equations by iterations due to the major and sudden changes caused by the cracks in the system stiffness matrix. When explicit integration is used, the damping matrix, which has little effect on slow loading rates, becomes quite important in dynamic analysis. The damping matrix is chosen as Rayleigh energy damping matrix as described in Section 3.1. Damping was kept below 1% with an α value of 0.1, and β value of 0.0001.

In the previous sections, it was shown that all the experimental results can be predicted reasonably with the help of the developed constitutive relations in OLM. Therefore, the numerical results given in this section were obtained by using the identical material parameters with the models used for the laboratory experiments. The OLM parameters for the lining were ε_{cr} = 6e-05, a_1 = 5, a_2 = 80, a_3 = 300, b_1 = 0.6, and b_2 = 0.2, whereas the OLM parameters for the rock body were ε_{cr} = 5e-05, a_1 = 10, a_2 = 30, a_3 = 40, b_1 = 0.6, and b_2 = 0.2.

In order for the transparent boundary conditions to work successfully, the boundary must be located at a sufficiently far distance from the tunnel lining. For this reason, after carrying out test simulations, transparent boundary conditions were placed four times the inner radius of the tunnel from the center of the tunnel. Tunnel geometry was taken as the same geometry used in the experimental studies. The internal radius used in the experiment was 0.72 m, the boundary conditions were placed at a distance of 2.88 m (Figure 56). In the dynamic analysis for circular tunnels, the inner radius

was taken as 0.72 m and the boundary conditions were again placed at a distance of 2.88 m (Figure 74).

In dynamic analysis part, internal normal pressure load was applied up to five different value ranged from 0.2 MPa to 1.0 MPa as shown in Figure 55 with a very small time step $\Delta t = 5x10^{-8}$.

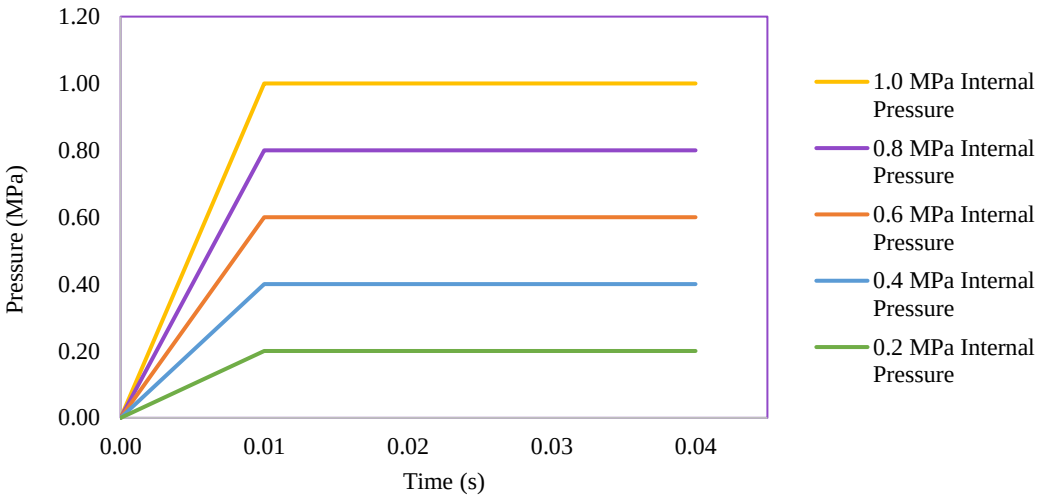

***Figure 55**. Internal pressure values vs time*

4.3.1. Results of Different Rock Qualities

First, dynamic analyzes were performed for the case where in situ stresses were negligible. Modulus of elasticity (24.3 GPa) measured experimentally in the first experiment was used for the concrete lining. With the aforementioned OLM material parameters, concrete fracture energy (G_F) for the lining were taken as 45 N/m. These lining parameters were used in all dynamic simulations. On the other hand, three different rock modulus of elasticity values (2 GPa, 4 GPa and 8 GPa) were used. In the analyses, since there was no loading plate and rubber sheet in these experiments, the uniform internal pressure was applied on the tunnel wall in the normal direction corresponding to real field conditions.

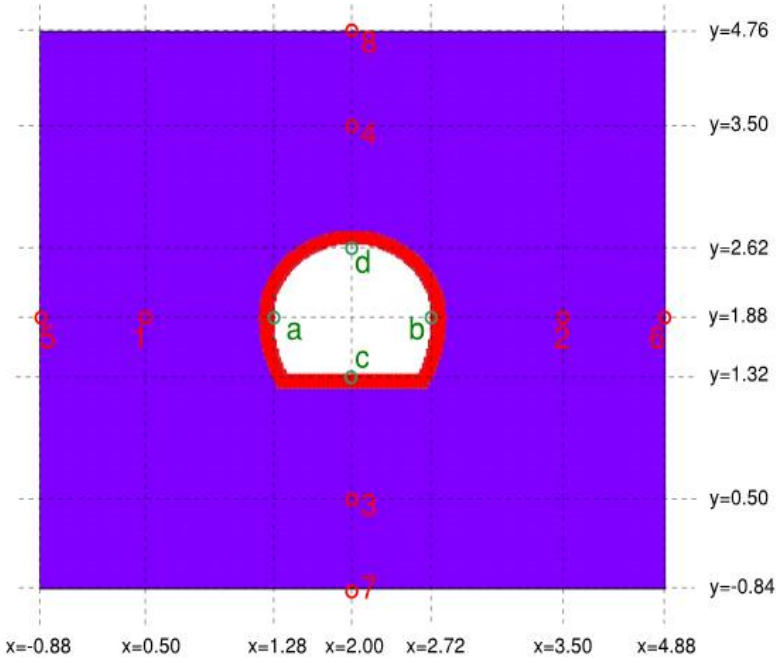

***Figure 56**. OLM elements and corresponding data points for the horse-shoe shaped lining*

First, the results the low stiffness rock (E = 2 GPa) are presented. The vertical and horizontal expansions of the tunnel over time are presented in Figure 57 and Figure 58. The tunnel lining exhibits a nearly linear behavior up to an internal pressure of 0.2 MPa, and above this value the damage is progressively increasing, and after about 0.6 MPa the tunnel is subjected to major deformations due to the severe damage to both the rock and the tunnel lining. Vertical and horizontal length changes are given in Figure 59 depending on internal pressure. Dashed lines show that the tunnel continues to deform when the internal pressure is greater than 0.4 MPa. That is, as observed in the second experiment, rock cracks and the tunnel undergoes severe damage under extreme internal pressure. The strain distributions which indicates the cracks estimated by the OLM are given in Figure 60. In Figure 61, all elements exceeding tensile strength are shown in red. It can be seen in both figures, when the internal pressure is 0.2 MPa, although tensile strength is exceeded in the left and right bottom corners of the tunnel, no observable cracks occur (crack widths below 0.2mm). When the internal pressure reaches 0.6 MPa, a significant part of the tunnel exceeds the tensile strength and many cracks begin to open.

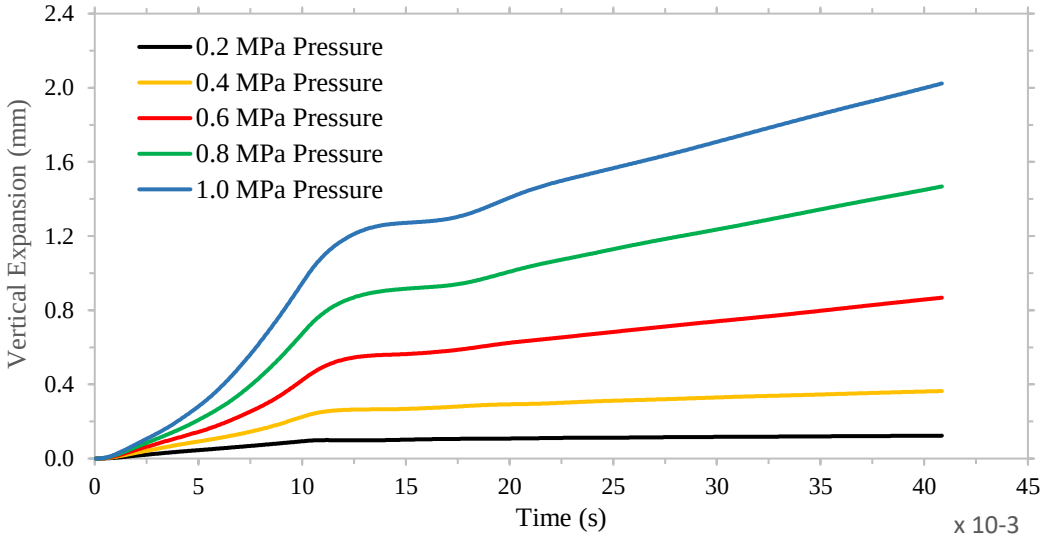

Figure 57. *Vertical expansions over time (E = 2 GPa)*

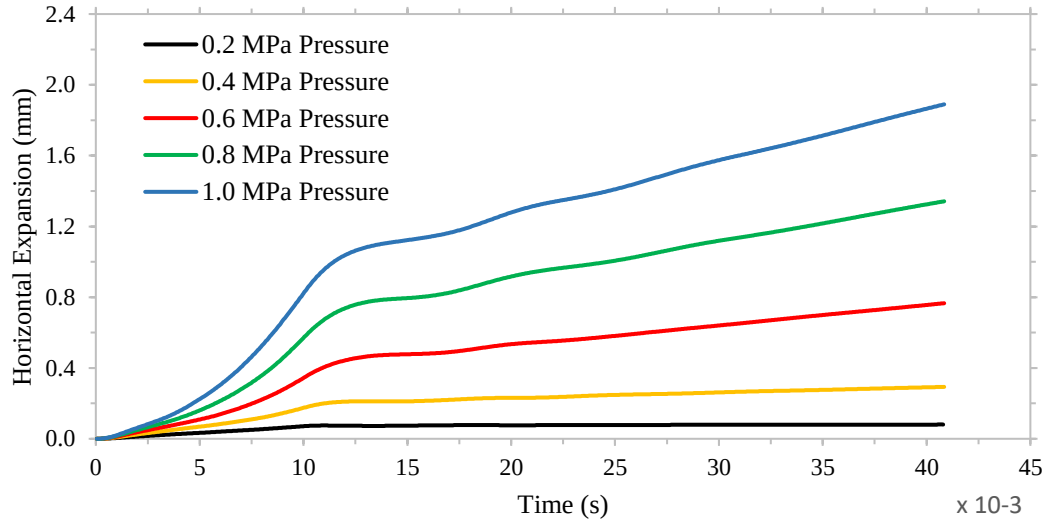

Figure 58. *Horizontal expansions over time (E = 2 GPa)*

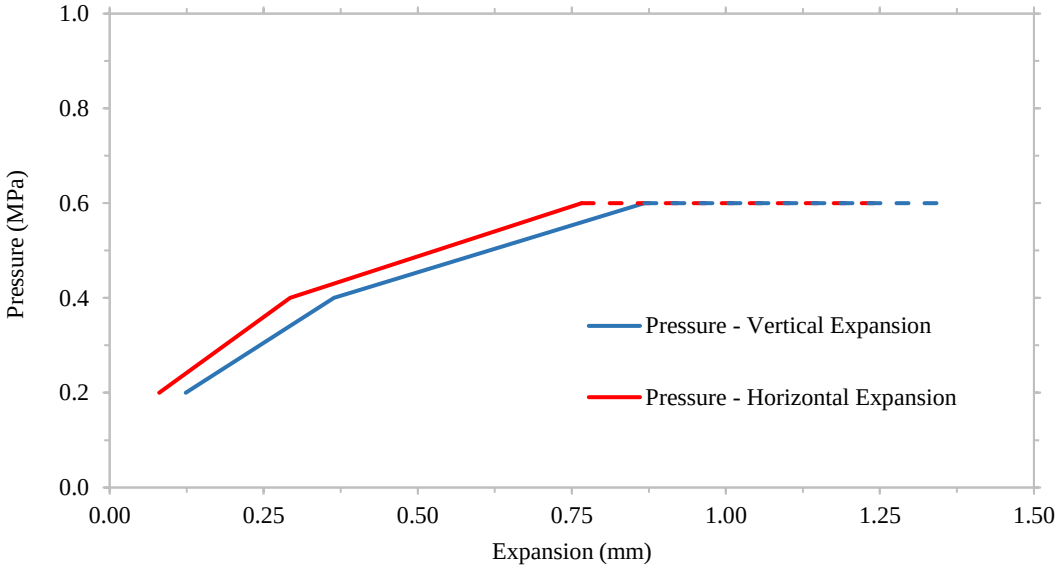

Figure 59. *Vertical and horizontal expansions according to internal pressure. The dashed lines indicate that the tunnel continues to take damage (E = 2 GPa)*

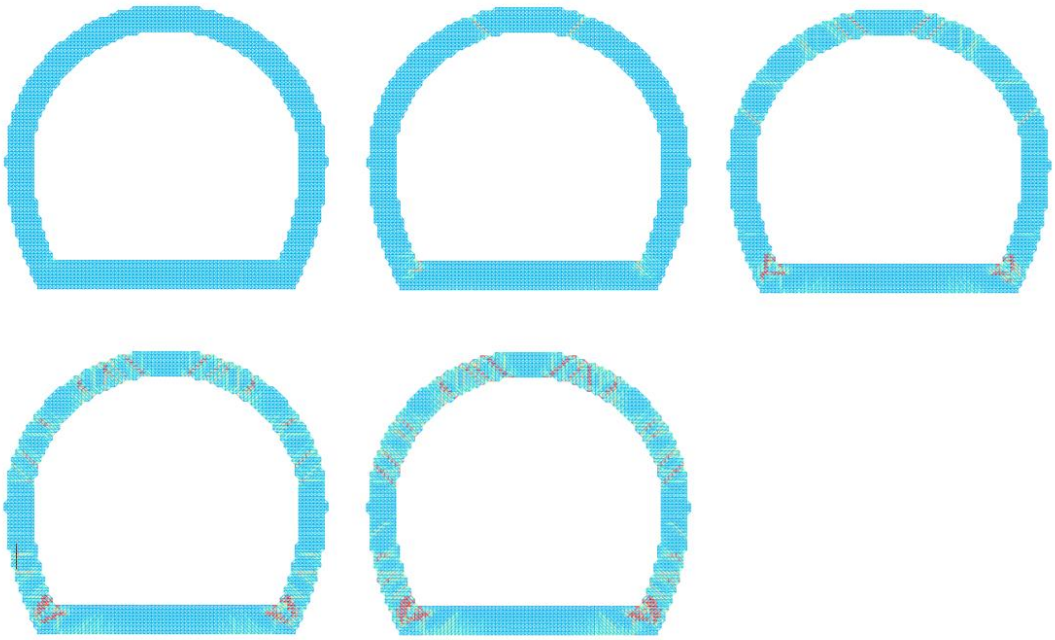

Figure 60. *The strain distribution estimated by the OLM for the internal pressure values of 0.2 MPa, 0.4 MPa, 0.6 MPa, 0.8 MPa and 1.0 MPa (color scale: blue = -0.001, red = 0.003, E = 2 GPa)*

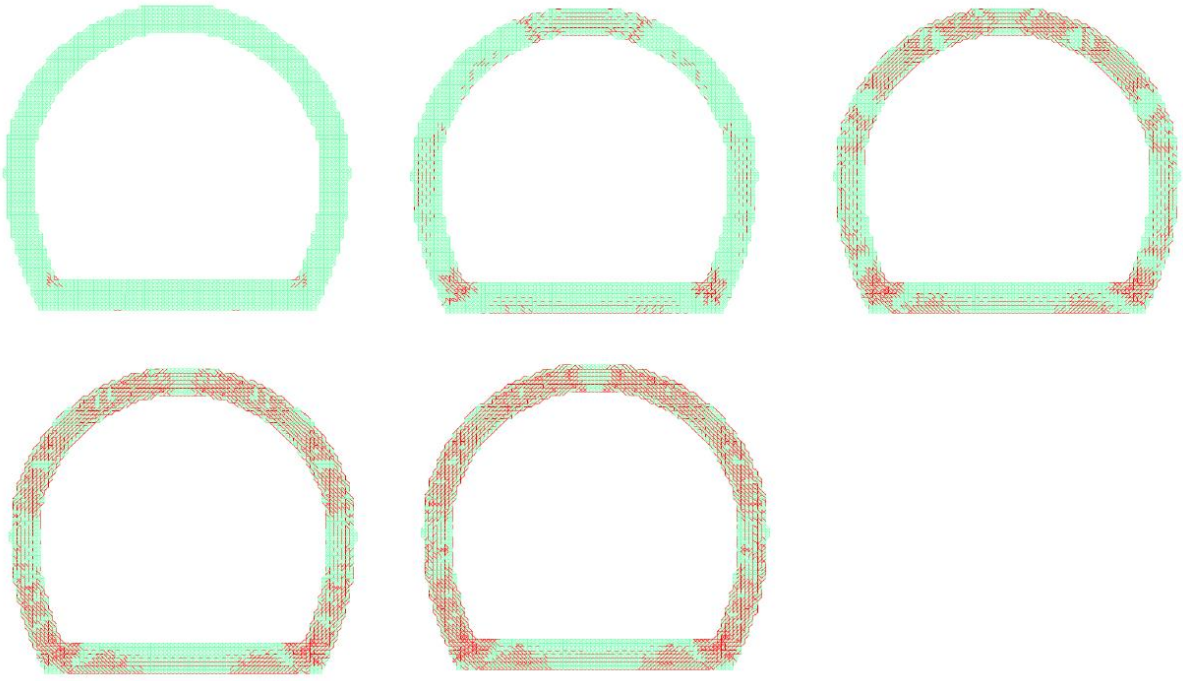

Figure 61. *Elements exceeding the tensile strength for internal pressure of 0.2 MPa, 0.4 MPa, 0.6 MPa, 0.8 MPa and 1.0 MPa shown in red (E = 2 GPa)*

The results obtained with elasticity modulus 4 GPa and 8 GPa are given in Figure 62 and Figure 65, respectively. Similar to the previous results, it should be noted that dashed lines represent continuation of the tunnel deformation, thus the distribution of damage given for these internal pressure values is not the final distribution of damage. As the load increased is far beyond the acceptable level, the final distribution of damage is not of interest. As the rock modulus of elasticity increases, it is seen that the number and the width of the cracks in the tunnel lining decrease Figure 66. In Figure 68, where all the results are compared, it is clearly observed that nonlinear behavior starts at smaller internal pressure values as the rock stiffness decreases. In the second experiment, when the internal pressure reached about 0.45 MPa, the rock surrounding the tunnel started to crack and the tunnel was severely damaged due to the pressure applied exceeding the tunnel lining capacity and the experiment was terminated. Taking rock modulus of elasticity as 8 GPa, it is observed that the formation of the first crack and the progression of this crack are quite similar with the

experimental observations (Figure 31 and Figure 69). In the second experiment, when the internal pressure reached about 0.50 MPa, the rock surrounding the tunnel started to crack and the tunnel was severely damaged due to exceeding the tunnel lining capacity and the experiment was terminated. Although pressure is slightly smaller than the internal pressure value in which severe damage occurs in Figure 68, it should be noted that the test was surrounded by a limited rock body. Numerical results were obtained as a tunnel placed in an infinite environment, therefore the numerical values were higher than experimental values.

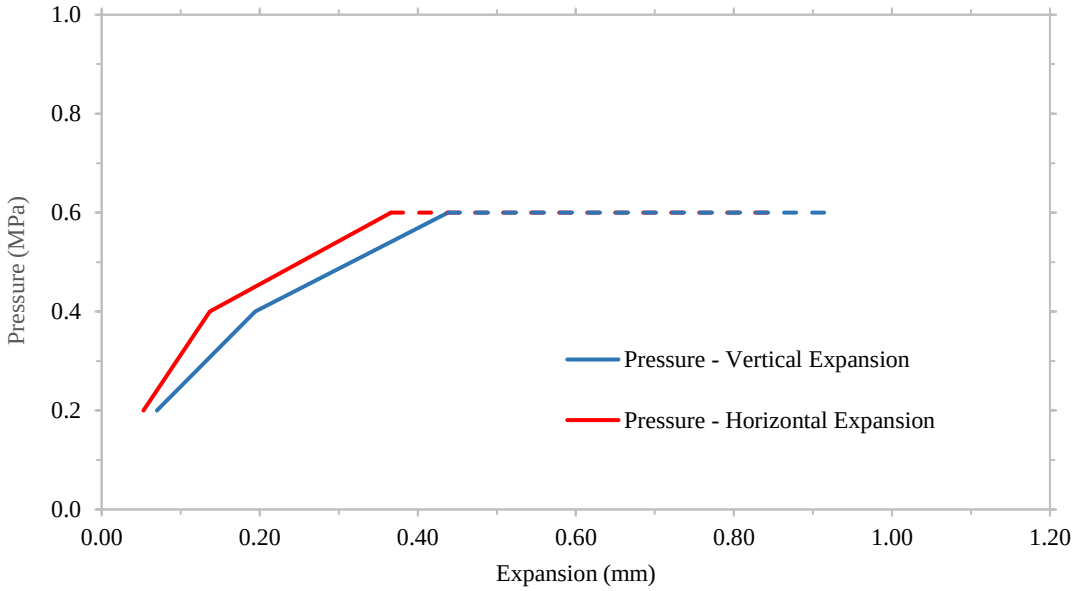

Figure 62. *Vertical and horizontal expansions according to internal pressure. The dashed lines indicate that the tunnel continues to take damage (E = 4 GPa)*

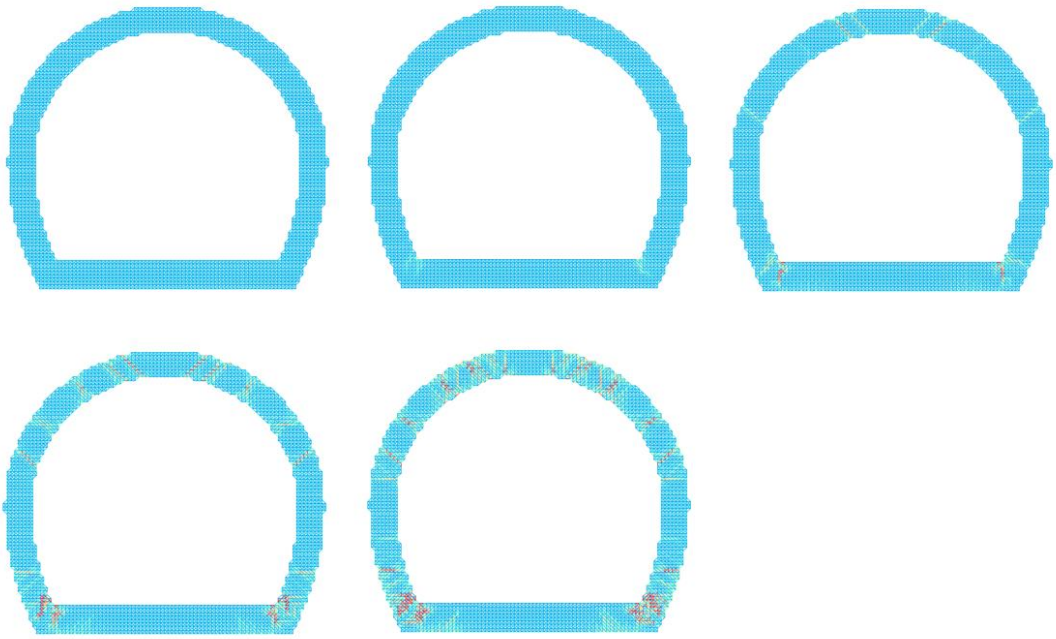

***Figure 63**. The strain distribution estimated by the OLM for the internal pressure values of 0.2 MPa, 0.4 MPa, 0.6 MPa, 0.8 MPa and 1.0 MPa (color scale: blue = -0.001, red = 0.003, E = 4 GPa)*

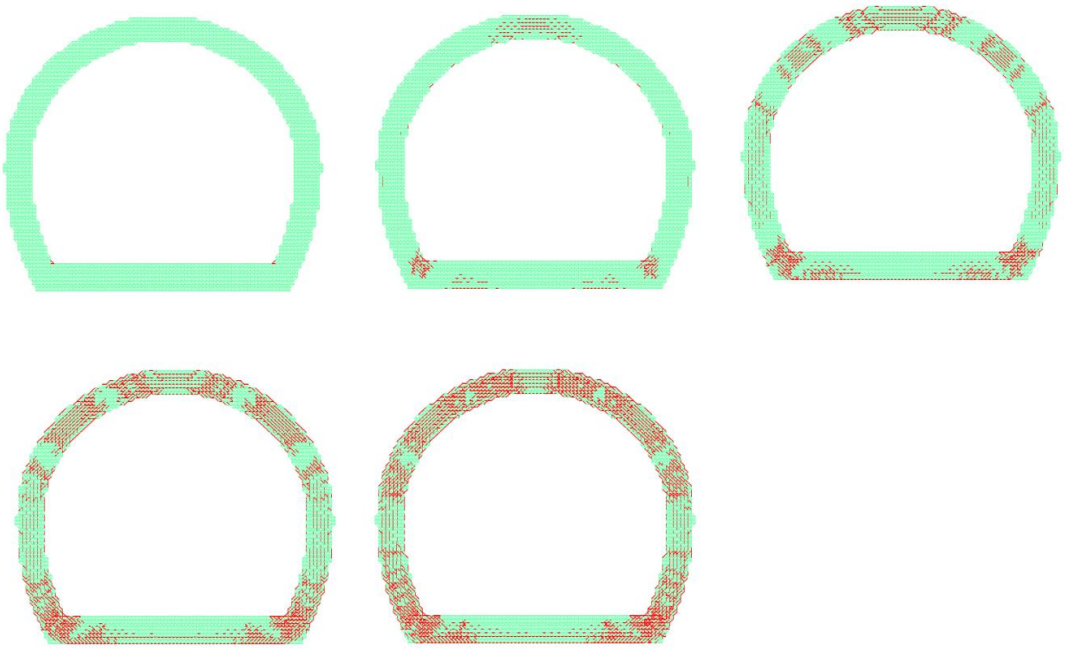

***Figure 64.** Elements exceeding the tensile strength for internal pressure of 0.2 MPa, 0.4 MPa, 0.6 MPa, 0.8 MPa and 1.0 MPa shown in red (E = 4 GPa)*

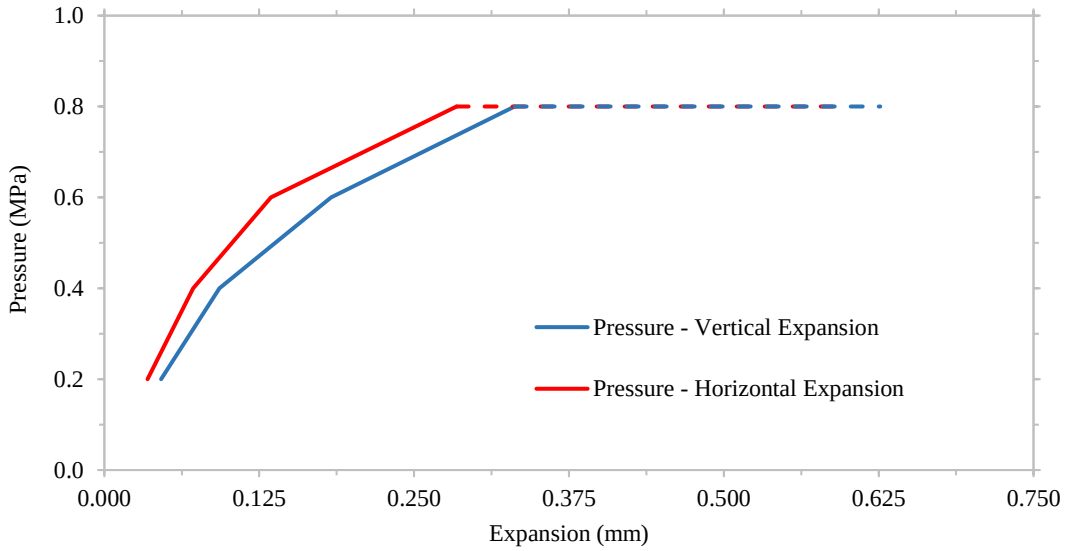

Figure 65. *Vertical and horizontal expansions according to internal pressure. The dashed lines indicate that the tunnel continues to take damage (E = 8 GPa)*

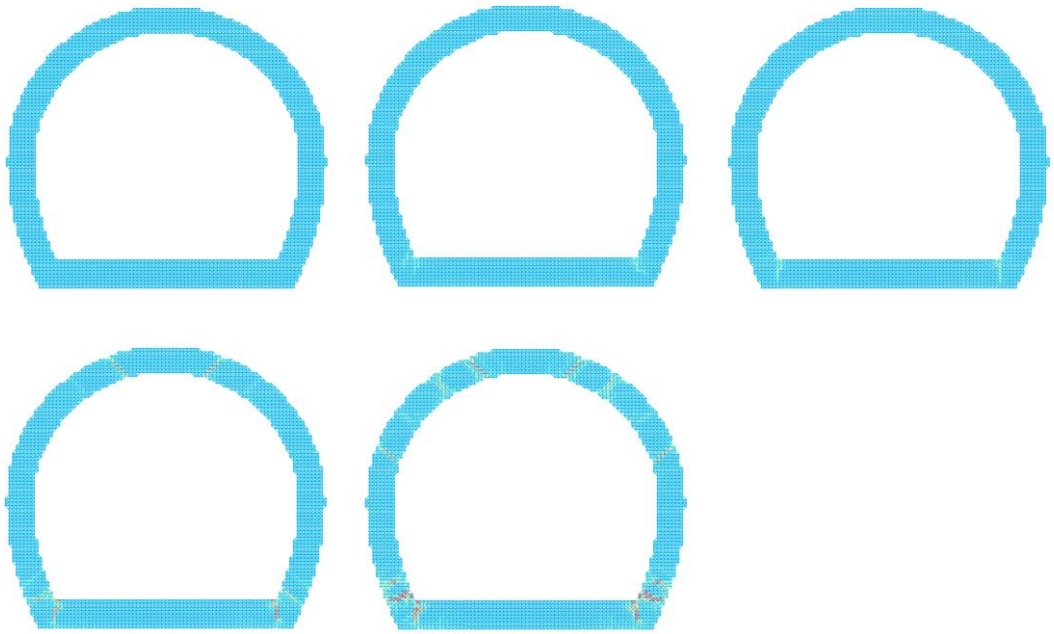

Figure 66. *The strain distribution estimated by the OLM for the internal pressure values of 0.2 MPa, 0.4 MPa, 0.6 MPa, 0.8 MPa and 1.0 MPa (color scale: blue = -0.001, red = 0.003, E = 8 GPa)*

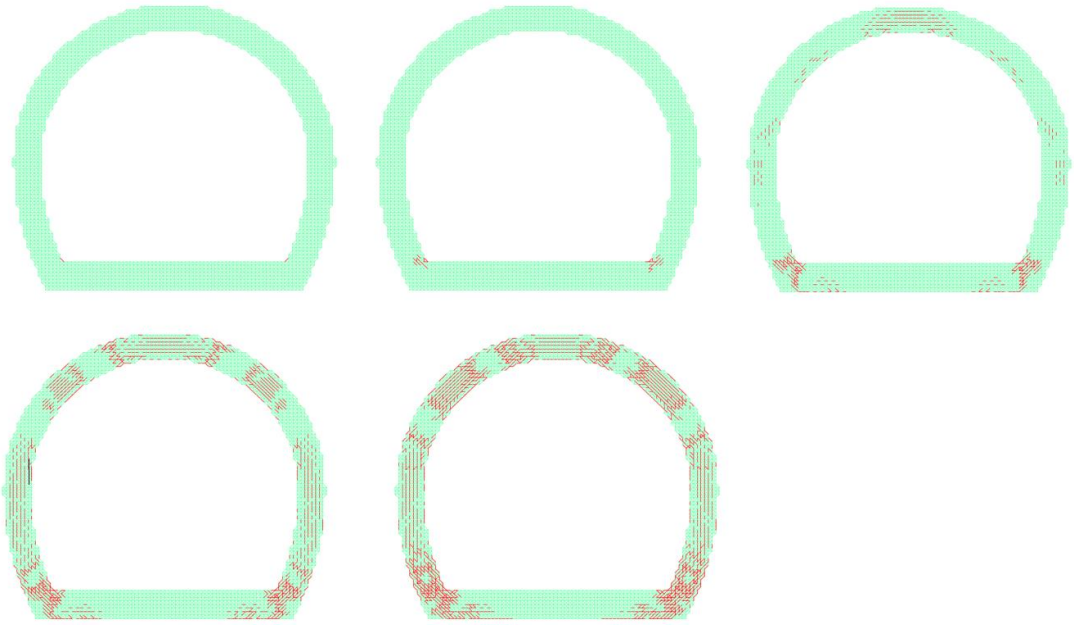

Figure 67. *Elements exceeding the tensile strength for internal pressure of 0.2 MPa, 0.4 MPa, 0.6 MPa, 0.8 MPa and 1.0 MPa shown in red (E = 8 GPa)*

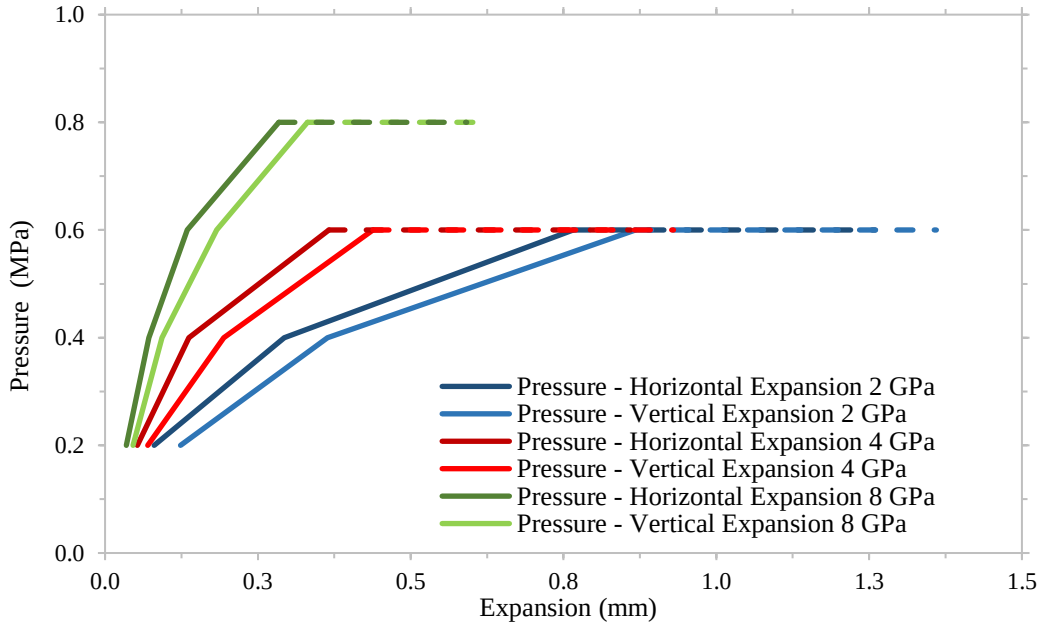

Figure 68. *Vertical and horizontal expansion for rock stiffness E = 2 GPa, 4 GPa and 8 GPa*

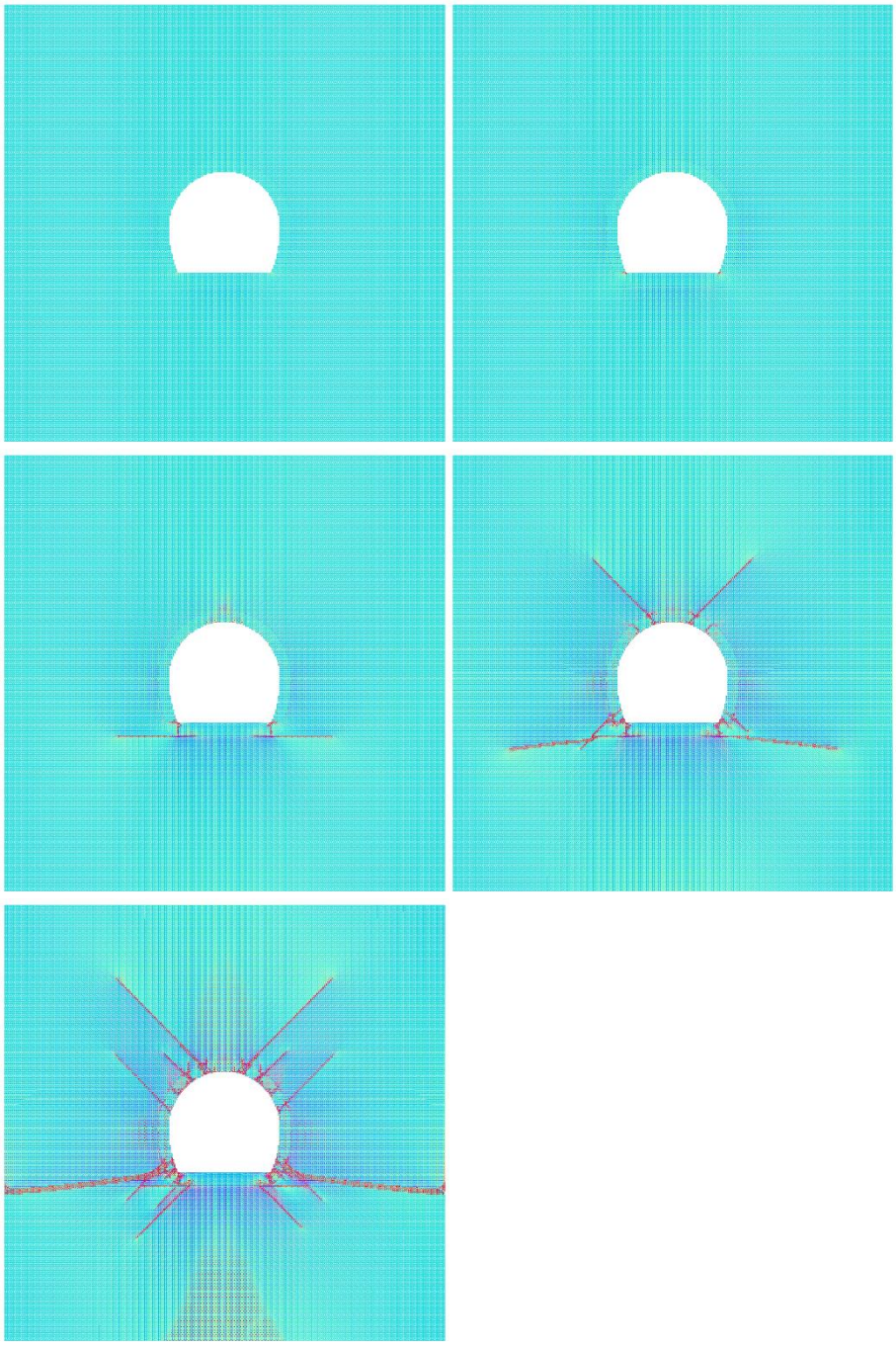

Figure 69. *Strain distribution estimated by OLM when total applied force is 0.2 MPa, 0.4 MPa, 0.6 MPa, 0.8 Mpa and 1.0 MPa respectively (E = 8 GPa) (color scale: blue = -0.0001, red = 0.0002)*

4.3.2. Effects of In-situ Stress

The overburden stress on the tunnel is one of the important parameters affecting the behavior of the tunnel lining. Experimental studies with in-situ stress have clearly demonstrated this effect (Kalaycıoğlu 2019). As the tunnel is placed deeper, the in-situ stress delays the cracking of the rock and helps to maintain the rigidity of the rock. In cases where the tunnel is placed too deep, the stresses caused by the opening of the tunnel may cause the rock to show plastic deformation. However, this behavior is expected to be at very high depths which is beyond the scope of this study.

In this study, considering the absence of in-situ stress testing of such structures, the gravitational in situ stress due to overlying rock is derived by the application of theory of elasticity with the tunnel depth and the tensile strain limit of rock (Equation 4.1). Poisson ratio is taken as 0.25. This approach can be used for rocks which do not lose their stiffness due to plastic deformation. Assuming that the vertical and horizontal stresses are equal (K_0 =1) depending on the depth of the tunnel, previous simulations were repeated by increasing this critical unit deformation capacity of the rock at the same rate. Therefore, the results given in the previous section correspond to the situation where the tunnel is very close to the surface.

$$\sigma_v = \gamma \times z = \sigma_h \ (K_0 = 1)$$

$$\overline{\varepsilon} = \frac{\sigma_h \times (1 - 2 \times \nu)}{E_{rock}} \qquad [4.1]$$

$$\overline{\varepsilon} = \gamma \times z \times \frac{0.5}{E_{rock}}$$

$$\overline{\varepsilon}_{cr} = \overline{\varepsilon} + \varepsilon_{cr}$$

where γ is the unit weight of the rock and z is the depth of tunnel. σ_v defines the vertical stress and σ_h is the horizontal stress. In Figure 70, the horizontal and vertical length changes are given for the case where the elastic modulus of the rock is 2 GPa and the internal pressure is 0.8 MPa. The parameters used in the simulations are the

same as those given in the previous section. The only difference is the increase in cracking strain (ε_{cr}) of the rock as a function of depth and unit weight. As it is clearly seen in the figure, increasing the depth of the tunnel causes the rock to crack less and this leads to the reduction of cracks caused by the transfer of internal pressure to the rock and to maintain rock rigidity. After a depth of approximately 50 m, the rock hardly loses its rigidity. A similar behavior can be observed in cases where the rock modulus of elasticity is 4 GPa and 8 GPa (Figure 71 and Figure 72).

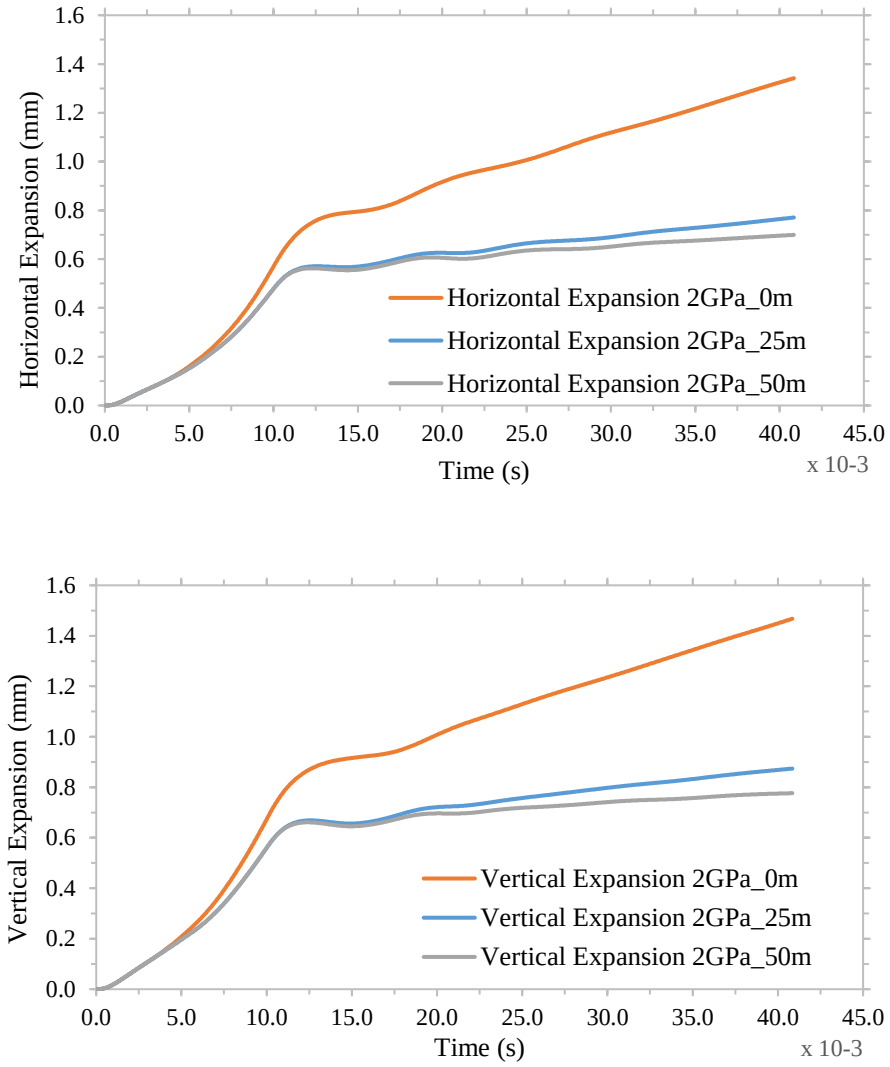

***Figure 70**. Variation of horizontal and vertical expansions over depth (E_{rock} = 2 GPa) for internal pressure 0.8 MPa*

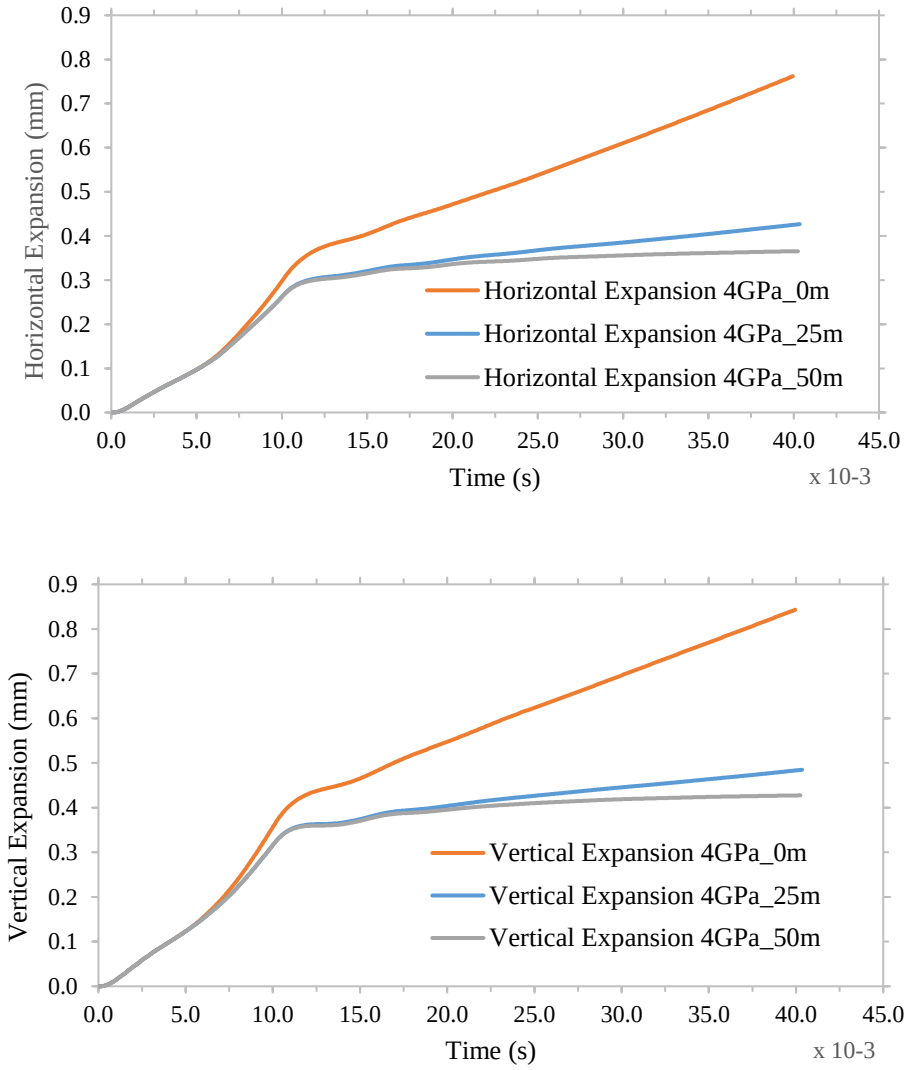

Figure 71. *Variation of horizontal and vertical expansions over depth (E_{rock} = 4 GPa)*

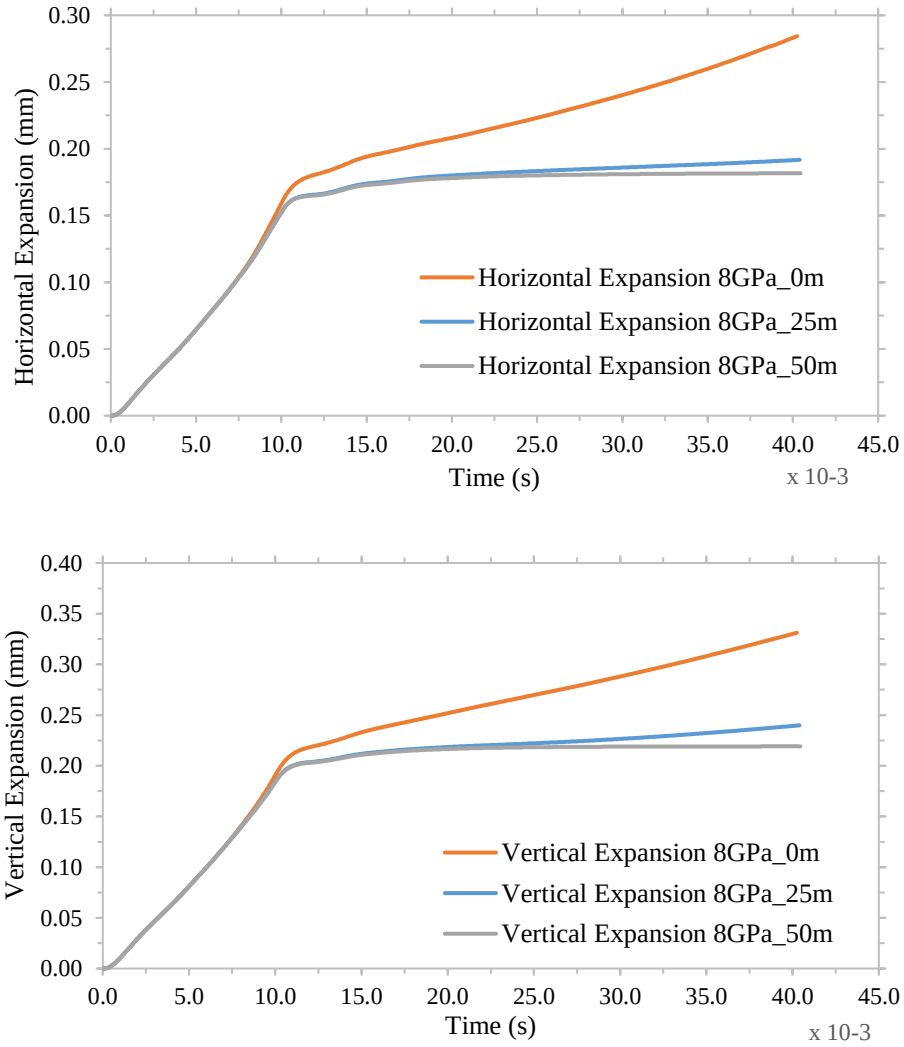

Figure 72. *Variation of horizontal and vertical expansions over depth (E_{rock} = 8 GPa)*

The damage in the tunnel lining in the simulation is shown in Figure 73. Damage on tunnel lining decreases as in-situ stress increases. However, it should also be noted that even if the tunnel is surrounded by rock that does not lose its rigidity, cracks occurs depending on the ratio of tunnel and rock stiffness.

With the help of numerical simulations, it can be said that the rock will behave almost elastic after a depth of 50 m. It is understood that for weak rock and / or rock environment that are expected to be damaged during the pressurization, therefore the design will be on the safe side without taking the field stresses into account.

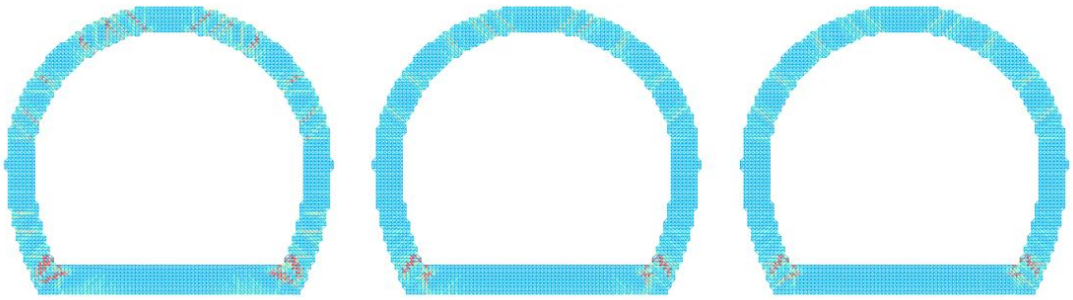

(a) E = 2 GPa

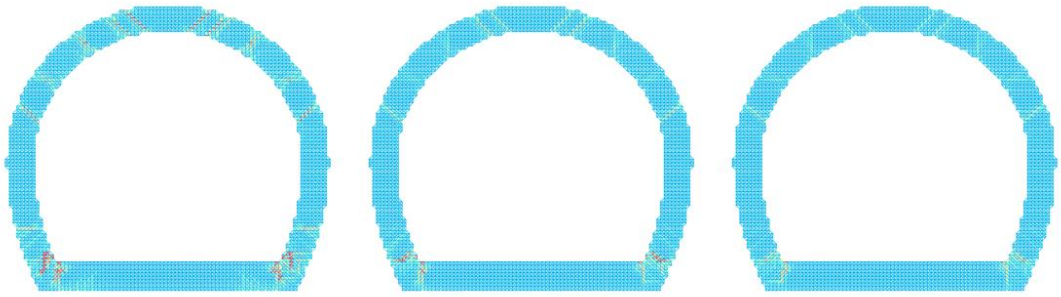

(b) E = 4 GPa

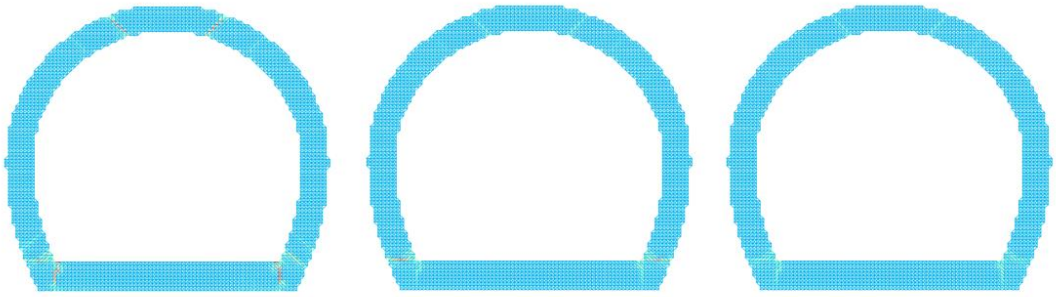

(c) E = 8 GPa

Figure 73. *Estimated strain distribution according to the elasticity modulus of rock (E = 2 GPa, E = 4 GPa, E = 8 GPa) from top to bottom and the increasing depth from left to right (0 m, 25 m, 50 m) (color scale: blue = -0.001, red = 0.003, 0.8 MPa internal pressure).*

4.3.3. Effect of Geometry

In this study, reverse horse-shoe tunnel geometry was used in experiments and numerical simulations. The reason for this choice is the widespread use of this type of internal pressure tunnel geometry in Turkey due to the advantages it provides in the construction process. The high tension zones in the left and right corners of the reverse horse-shoe shaped tunnel have come to the fore as the first cracking part in both experimental and numerical studies. Therefore, it can be said that the geometry used has a significant disadvantage. In this section, the reverse horseshoe geometry used in the experiments is compared with classical circular geometry in pressure tunnel simulations. There is an approximate 3% difference in the circumferential lengths of these two geometries, which are very close to each other in terms of total area (the circumference of the circular section is shorter).

Modulus of elasticity (24.3 GPa) measured experimentally in the first experiment was used for the concrete lining. With the previously mentioned OLM material parameters, concrete fracture energy (G_F) for the lining was taken as 45 N/m. The rock elasticity modulus was selected as 8 GPa, similar to the layered rock material in the second experiment. Therefore, fracture energy for rock body incorporated into OLM model, was approximately 3.0 N/m.

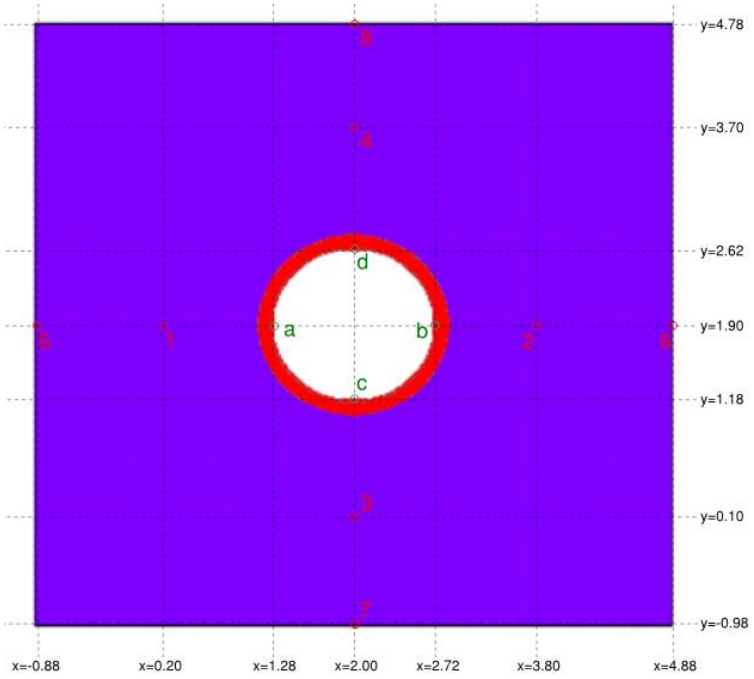

Figure 74. *OLM elements and corresponding data points for circular lining*

When Figure 78 is compared with Figure 73, it is observed that the difference in damage amounts distributes the load of the circular section up to 0.6 MPa value of the internal pressure, but above this value, both tunnel geometries are insufficient to meet the pressure. In the reverse horse-shoe tunnel geometry, due to stress concentrations, cracks occur in the lower corners when the internal pressure exceeds 0.4 MPa, and when the internal pressure reaches 0.6 MPa, significant differences occur between the vertical and horizontal tunnel expansions. In circular tunnel geometry, when the internal pressure is below 0.6 MPa, the cracks are considered as within acceptable limit. As shown in Figure 75, depending on modulus of elasticity of the rock, circular shaped tunnels have 10-20 % less expansions comparing to the tunnels with horse-shoe shaped geometry. With rock modulus of elasticity as 4 GPa, it is concluded that the rock lost its strength when the internal pressure exceeds the limit 0.6 MPa (Figure 76). Finally, OLM simulations were performed for all combinations where the circular tunnel was placed at 0 m, 25 m and 50 m depth and the rock elasticity modulus was 2 GPa, 4 GPa and 8 GPa by the method described in Section 4.3.2. The results are shown

in Figure 77 and Figure 78. Similar to the horse-shoe shaped geometry results, it can be said that the rock confinement up to 50 m, decreases the number of cracks and crack widths considerably.

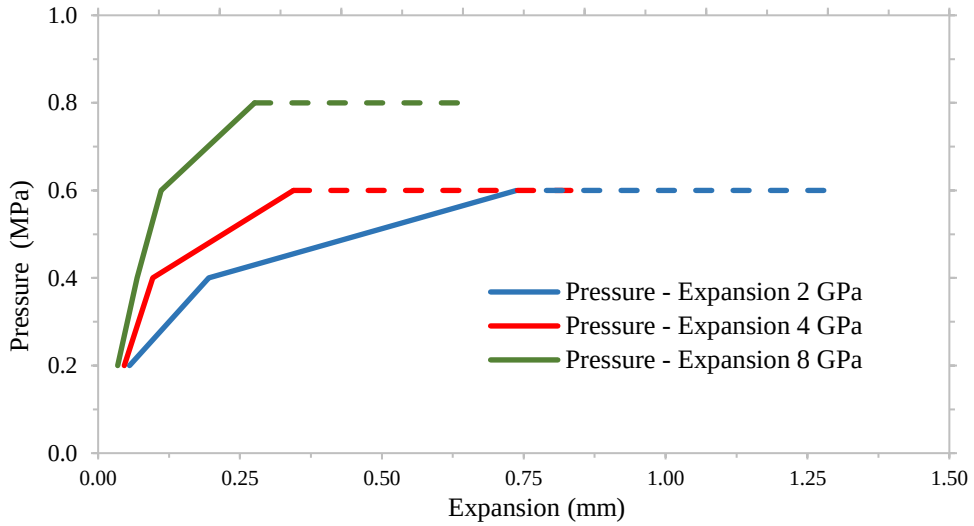

Figure 75. *Tunnel expansions for rock stiffness E = 2 GPa, 4 GPa and 8 GPa*

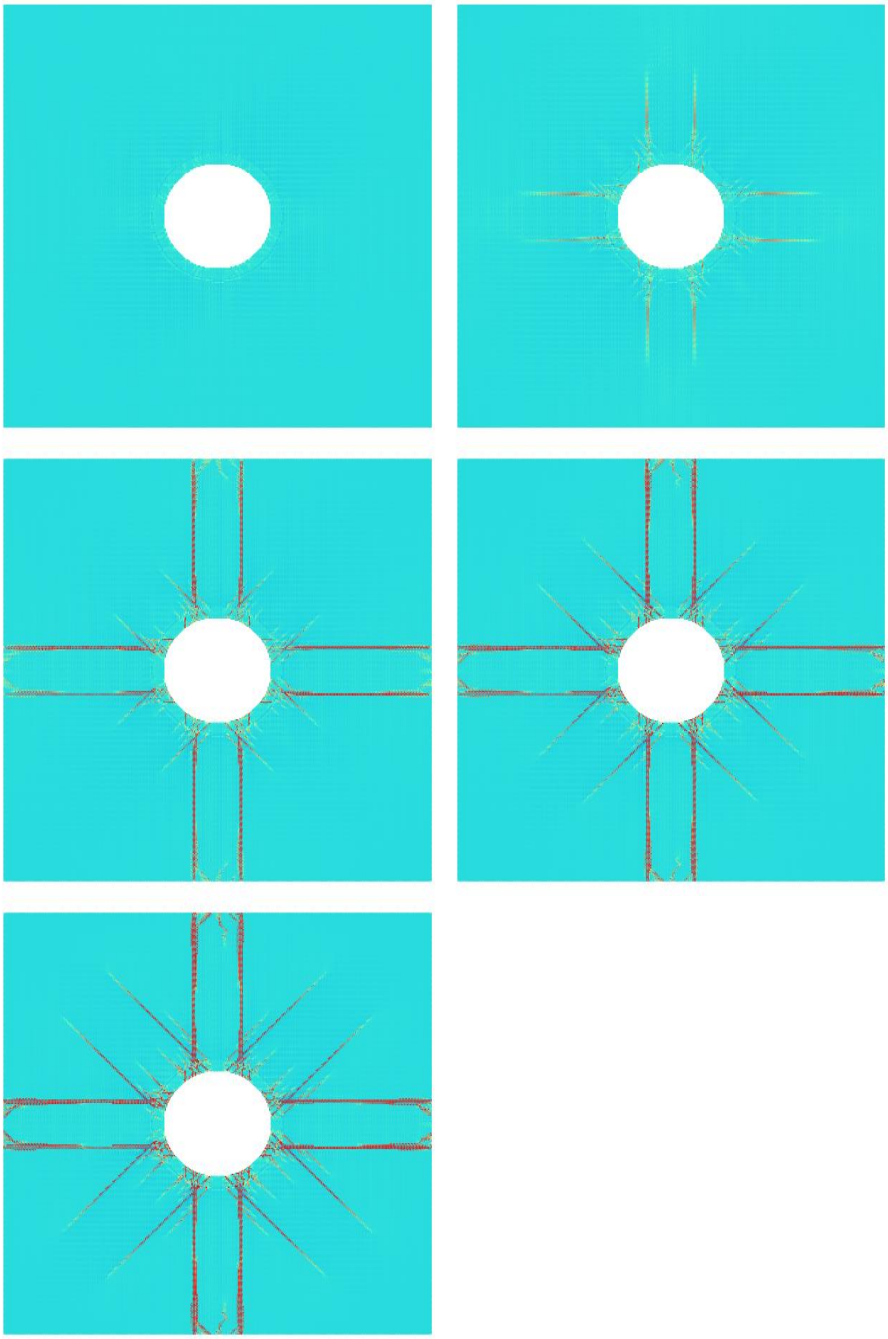

Figure 76. *Strain distribution estimated by OLM when total applied force is 0.2 MPa, 0.4 MPa, 0.6 MPa, 0.8 MPa and 1.0 MPa respectively (E = 4 GPa) (color scale: blue = -0.0001, red = 0.0002)*

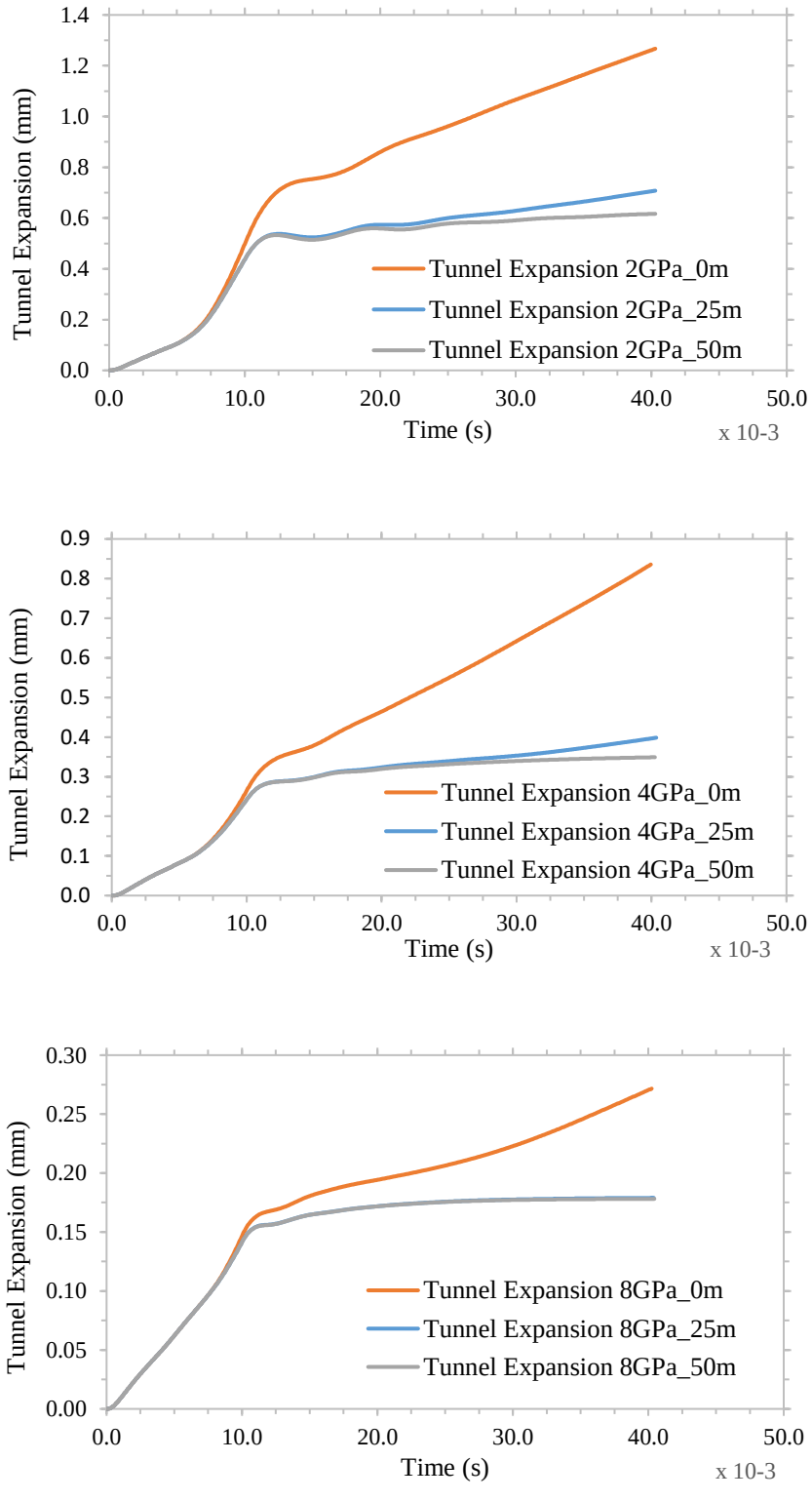

Figure 77. *Variation of tunnel expansions over depth*

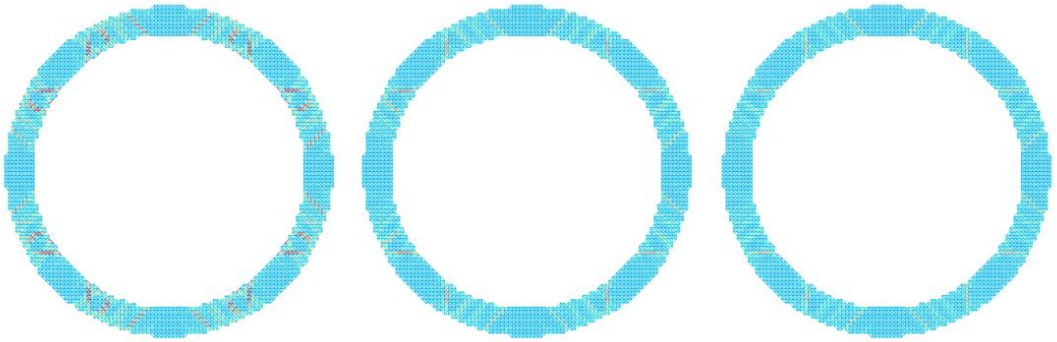

(a) E = 2 GPa

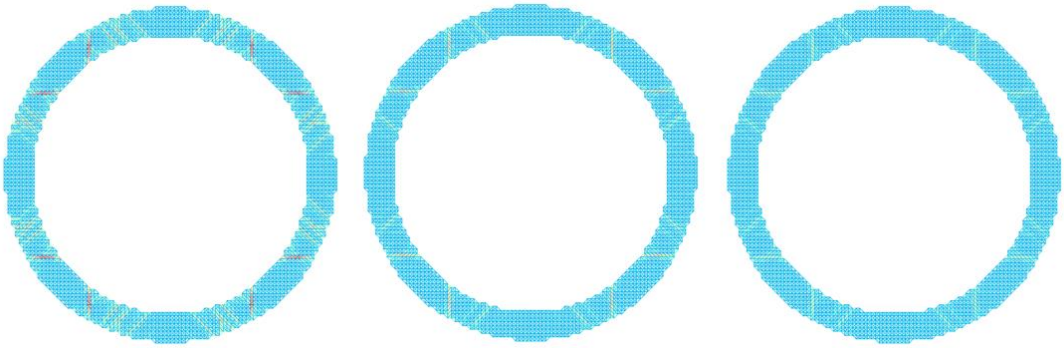

(a) E = 4 GPa

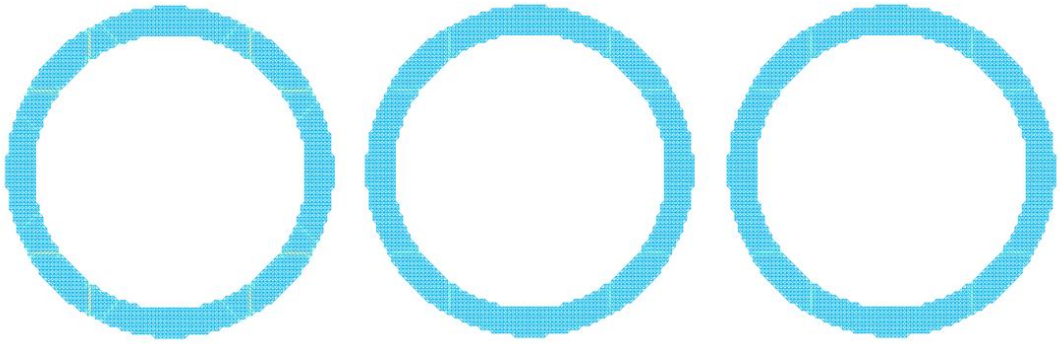

(a) E = 8 GPa

Figure 78. *Estimated strain distribution according to the elasticity modulus of rock (E = 2 GPa, E = 4 GPa, E = 8 GPa) from top to bottom and the increasing depth from left to right (0 m, 25 m, 50 m) (color scale: blue = -0.001, red = 0.003, 0.8 MPa internal pressure)*

CHAPTER 5

CONCLUSION

In this study, OLM simulations of pressure tunnel experiments are presented. Following conclusions are drawn with future studies for applications and further development of the numerical modeling as follows:

- OLM was capable of predicting the key variables (such as tunnel expansion, damage distribution, etc.) with a reasonable accuracy using just a few variables (fracture energy, elasticity modulus, tensile strength).
- Behavior of tunnel lining depends considerably on the contact between the lining and rock body. Local imperfections are likely cause of cracks that are observed in practice.
- Dynamic amplification was not accounted in the computations, as loading rate considered in the experiments were very low. As dynamic experiments do not seem feasible, computational approach is the only way to simulate the actual crack initiation and propagation in pressure tunnels.
- Fiber-reinforced concrete tunnel linings are likely to distribute evenly the damage and decrease crack widths.
- Circular shaped tunnels have 10-20 % less expansions compared to the tunnels with horse-shoe shaped geometry
- Tunnel linings with appropriate rock confinement have less cracks with the application of in-situ stress conditions up to 50 m.
- Based on the findings of experimental and computational studies, design guidelines for pressure tunnels can be created to assist practicing engineers.
- The effect of water pressure in the cracks was ignored. Experimental and computational research programs focusing on the micro modeling of this phenomenon are necessary for more advanced mathematical models.

- Effects of cold joints and localized rock softening due to early tunneling applications could be studied to be incorporated into mathematical models.
- Computational time of the PID solutions should be evaluated further to obtain an optimum time-cost relation.
- Shear and compression failure modes could be implemented into the OLM for better understanding of concrete behavior.
- Three-dimensional OLM studies should be carried out to eliminate the 2D-3D effect which can be the cause of the differences between dynamic results.

REFERENCES

ACI 318-11. (n.d.). *Building code requirements for structural concrete (ACI 318-11). American Concrete Institute*. https://doi.org/10.1016/0262-5075(85)90032-6

ACI Committee 544. (2010). *ACI 544.5R-10 - Report on the Physical Properties and Durability of Fiber-Reinforced Concrete*. *ACI Structural Journal*.

ASTM C-76-15. (2009). *Standard Specification for Reinforced Concrete Culvert, Storm Drain, and Sewer Pipe*. https://doi.org/10.1520/C1417M-15.2

Aydin, B. B., Tuncay, K., & Binici, B. (2018). Overlapping Lattice Modeling for concrete fracture simulations using sequentially linear analysis. *Structural Concrete*, *19*(2), 568–581. https://doi.org/10.1002/suco.201600196

Aydın, B. B. (2017). *Overlapping Lattice modelling for concrete fracture simulations using sequantially linear analysis*.

Bakhshi, M., & Nasri, V. (2016). Design of fiber-reinforced tunnel segmental lining according to new ACI report, 1–10.

Barenblatt, G. I. (1959). The formation of equilibrium cracks during brittle fracture. General ideas and hypotheses. Axially-symmetric cracks. *Journal of Applied Mathematics and Mechanics*. https://doi.org/10.1016/0021-8928(59)90157-1

Bazant, Z. P., & Oh, B. H. (1983). Crack band theory for fracture of concrete, 155–177. https://doi.org/10.1007/BF02486267

Bazant, Z. P., & Planas, J. (1997). Fracture and size effect in concrete and other quasibrittle materials. *CRC Press*. https://doi.org/10.12989/cac.2012.9.1.001

Bieniawski, Z. T. (1978). Determining rock mass deformability: experience from case histories. *International Journal of Rock Mechanics and Mining Sciences And*, *15*(5), 237–247. https://doi.org/10.1016/0148-9062(78)90956-7

Biot, M. A. (1935). Effect of certain discontinuities on the pressure distribution in a loaded soil. *Journal of Applied Physics*, *6*(12), 367–375.

Boussinesq, J. V. (1877). Essai sur la thêorie des eaux courantes (Essay on the theory of water flow). *Mêmoires Prêsentês Par Divers Savants â l'Acadêmie Des Sciences, Paris*, 1–680.

Brekke, T. L., & Ripley, B. D. (1993). Design of pressure tunnels and shafts. In *Analysis and Design Methods*. https://doi.org/10.1016/b978-0-08-040615-2.50020-4

British Standards Institution. (2008). Eurocode 2 - Design of concrete structures. *Part 1-1: General Rules and Rules for Buildings*.

Chung, J., & Lee, M. J. (1994). A new family of explicit time integration methods. *International Journal for Numerical Methods in Engineering*, *37*(1), 3961–3976. https://doi.org/10.1088/1757-899X/10/1/012145

Chung, S. K., Synn, J. H., Park, C., Sunwoo, C., Park, C., & Choi, S. O. (2001). Design criteria for the reinforcement of a water pressure tunnel driven by TBM. *Geosystem Engineering*, *4*(2), 43–49.

Collins, M. P., & Vecchio, F. J. (1986). The Modified Compression-Field Theory for Reinforced Concrete Elements Subjected to Shear. *ACI Journal Proceedings*, *83*(2). https://doi.org/10.14359/10416

Coon, R. F., & Merritt, A. H. (1969). Determination of the in situ modulus of deformation of rock (pp. 154–173). Denver CO: ASTM Special Technical Publication.

Cusatis, G., Bažant, Z. P., & Cedolin, L. (2003). Confinement-Shear Lattice Model for Concrete Damage in Tension and Compression: II. Computation and Validation. *Journal of Engineering Mechanics*, *129*(12), 1449–1458. https://doi.org/10.1061/(asce)0733-9399(2003)129:12(1449)

Dowding, C. H., & Rozen, A. (1978). Damage to rock tunnels from earthquake shaking. *International Journal of Rock Mechanics and Mining Sciences & Geomechanics Abstracts*, *15*(4), 83. https://doi.org/10.1016/0148-9062(78)91355-4

Dugdale, D. S. (1960). Yielding of steel sheets containing slits. *Journal of the Mechanics and Physics of Solids*

Fantilli, A. P., Chiaia, B., & Frigo, B. (2014). Analogies in Fracture Mechanics of Concrete, Rock and Ice. *Procedia Materials Science*, *3*(December 2014), 397–407. https://doi.org/10.1016/j.mspro.2014.06.067

Fernández, G. (1994). Behavior of pressure tunnels and guidelines for liner design. *Journal of Geotechnical Engineering*, *120*, 1768–191.

Gerstle, W., Sau, N., & Sakhavand, N. (2009). On peridynamic computational simulation of concrete structures. In *American Concrete Institute, ACI Special Publication*.

Gerstle, W., Sau, N., & Silling, S. A. (2005). Peridynamic modeling of plain and reinforced concrete structures. *18th International Conference on Structural Mechanics in Reactor Technology (SMiRT 18)*, 54–68.

Griffith, A. A. (1921). The phenomena of rapture and flow in soilds. *Philosophical Transactions of the Royal Society of London.Series A, Containing Papers of a Mathematical of Physical Character*.

Guinea, G. V., Planas, J., & Elices, M. (1992). Measurement of the fracture energy using three-point bend tests: Part 1 Influence of experimental procedures. *Materials and Structures*, *25*, 212–218.

Hashash, Y. M. A., Hook, J. J., Schmidt, B., & I-Chiang Yao, J. (2001). Seismic design and analysis of underground structures. *Tunnelling and Underground Space Technology*, *16*(4), 247–293.

Henager, C. H., & Doherty, T. J. (1976). Analysis of reinforced fibrous concrete beams. *Journal of the Structural Division*.

Herrmann, H. J. (1988). Introduction to Modern Ideas on Fracture Patterns. In *Random Fluctuations and Pattern Growth: Experiments and Models*. https://doi.org/10.1007/978-94-009-2653-0_27

Hillerborg, A., Modéer, M., & Petersson, P. E. (1976). Analysis of crack formation and crack growth in concrete by means of fracture mechanics and finite elements. *Cement and Concrete Research*, *6*, 773–781. https://doi.org/10.1016/0008-8846(76)90007-7

Hoek, E., Marinos, P., & Benissi, M. (1998). Applicability of the geological strength index (GSI) classification for very weak and sheared rock masses. The case of the Athens Schist Formation. *Bulletin of Engineering Geology and the Environment*, *57*(2), 151–160. https://doi.org/10.1007/s100640050031

Hrennikoff, A. (1941). Solution of problems of elasticity by framework method. *ASME J. Appl. Mech*, (8), 169–170.

Ingraffea, A. R., & Saouma, V. (1985). Numerical modeling of discrete crack propagation in reinforced and plain concrete. *Fracture Mechanics of Concrete: Structural Application and Numerical Calculation*, *4*, 171–225.

Irwin, G.R. (1958), "Fracture", *Handbuch der Physik*, 6, 551-590.

Jaramillo, C. A. (2017). Impact of seismic design on tunnels in rock – Case histories. *Underground Space*, *2*(2), 106–114.

Jenq, Y., & Shah, S. P. (1985). Two parameter fracture model for concrete. *Journal of Engineering Mechanics*, *111*(4), 1227–124.

Johnson, R. P., Eddie, C. M., & Psomas, S. (2017). Design of steel fibre reinforced concrete tunnel linings. *Proceedings of the Institution of Civil Engineers*, *170*(SB2), 115–130.

Kalaycıoğlu, M. T. (2019). *Experimental Investigation of Pressurized Concrete Tunnel Linings.* METU.

Kocamaz, K. (2018). *Explicit Nonlinear Analysis for Quasi-Static Behavior of Frame Structures with PID Control and Mass Scaling*. METU.

Kwak, H.-G., & Filippou, F. C. (1990). *Finite element analysis of reinforced concrete structures under monotonic loads*. *Structural Engineering Mechanics and Materials*.

Madenci, E., & Oterkus, E. (2014). *Peridynamic theory and its applications*. *Peridynamic Theory and Its Applications*. https://doi.org/10.1007/978-1-4614-8465-3

Mitchell, J. A. (2011). A Non-local, Ordinary-State-Based Viscoelasticity Model for Peridynamics. *Sandia Report*.

Mörsch, E. (1909). *Concrete-steel construction*. (English tranlation by E. P. Goodrich, Ed.). McGraw-Hill, New York.

Ng, C. W. W., Wang, R., & Boonyarak, T. (2016). A comparative study of the different responses of circular and horseshoe-shaped tunnels to an advancing tunnel underneath. *Géotechnique Letters*, *6*(2), 168–175.

Ngo, D., & Scordelis, A. C. (1967). Finite element analysis of reinforced concrete beams. *Journal of the American Concrete Institute*, *64*, 152–163.

Nitschke, A. G., & Winterberg, R. (2016). Performance of macro synthetic fiber reinforced tunnel linings. *ITA-AITES World Tunnel Congress 2016, WTC 2016*, *1*, 1–13.

Olumide, B. A. (2013). Numerical coupling of stress and seepage in the design of pressure tunnel under to high internal water pressure. *International Journal of Engineering and Technology*, *3*(3), 235–244.

Olumide, B. A., & Marence, M. (2012). A finite element model for optimum design

of plain concrete pressure tunnels under high internal pressure. *International Journal of Engineering and Technology*, *2*(5), 676–683.

Palmstrom, A. (1987). Norwegian design and construction experiences of unlined pressure shafts and tunnels. In *Proceedings of the International conference on Hydropower in Oslo* (pp. 87–111). Norway.

Palmström, A., & Stille, H. (2015). *Rock Engineering, Second edition*. *6th ISRM Congress*. ICE Publishing.

Rao, G. A., & Prasad, R. B. K. (2001). Fracture process zone in high strength concrete. *Fracture Mechanics of Concrete Structures*, (1990), 327–332.

Ritter, W. (1899). Die Bauweise Hennebique (Construction works). *Schweizerische Bauzeitung*. https://doi.org/10.3931/e-rara-20036

Rots, J. G. (1988). *Computational modeling of concrete fracture*. *Delft*. https://doi.org/10.1007/978-1-61779-191-8_1

Rots, J. G. (2001). Sequentially linear continuum model for concrete fracture. *Fracture Mechanics of Concrete Structures*, 831–839.

Rots, J. G., & Blaauwendraad, J. (1989). Crack models for concrete: discrete or smeared? Fixed multi-directional or rotatin? *Heron*.

Schlaich, J., Schafer, K., & Jennewein, M. (1987). *Toward a Consistent Design of Structural Concrete*. *PCI Journal* (Vol. 32).

Schleiss, A. J. (1986). Design of pervious pressure tunnels. *International Water Power and Dam Construction*, *38*, 21–26.

Schleiss, A. J. (1997). Design of reinforced concrete linings of pressure tunnels and shafts. *International Journal on Hydropower and Dams*, *4*, 88–94.

Sengun, E., Alam, B., & Yaman, I. O. (2016). Effect of synthetic fibers on flexural performance of normal and high performance concrete. *9th RILEM International*

Symposium on Fiber Reinforced Concrete, (September), 19–21.

Shah, S. P., & Naaman, A. E. (1976). Mechanical Properties of Glass and Steel Fiber Reinforced Mortar. *ACI Journal Proceedings*. https://doi.org/10.14359/11055

Silling, S. A. (2000). Reformulation of elasticity theory for discontinuities and long-range forces. *Journal of the Mechanics and Physics of Solids*.

Silling, S. A., Epton, M., Weckner, O., Xu, J., & Askari, E. (2007). Peridynamic states and constitutive modeling. *Journal of Elasticity*. https://doi.org/10.1007/s10659-007-9125-1

Sinha, R. S. (1989). *Underground Structures: Design and Instrumentation*. Elsevier.

Sorelli, L., & Toutlemonde, F. (2005). On the design of steel fiber reinforced concrete tunnel lining segment. *11th International Conference on Fracture, Turin (Italy)*, 3–8.

Sukumar, N., Moës, N., Moran, B., & Belytschko, T. (2000). Extended finite element method for three-dimensional crack modelling. *International Journal for Numerical Methods in Engineering*, *48*(11), 1549–1570.

Swamy, R. N. (1975). Fibre reinforcement of cement and concrete. *Matériaux et Constructions*. https://doi.org/10.1007/BF02475172

Trivedi, N., Singh, R. K., & Chattopadhyay, J. (2015). A comparative study on three approaches to investigate the size independent fracture energy of concrete. *Engineering Fracture Mechanics*, *138*, 49–62.

TS-500. (2000). *Betonarme Yapıların Tasarım ve Yapım Kuralları*. Ankara.

Tuncay, K., Binici, B., & Yaman, İ. Ö. (2016). Computational modelling of pressurized reinforced concrete tunnel linings. In *12th International Congress on Advances in Civil Engineering* (pp. 1–8).

USBR Design Standards No:3 Water conveyance facilities, fish facilities, and roads

and bridges. (2014). Water conveyance facilities, fish facilities, and roads and bridges chapter 4: tunnels, shafts, and caverns phase 4 (final), *4*(3).

Van Mier, J. G. M. (2012). *Concrete fracture: A multiscale approach*. *Concrete Fracture: A Multiscale Approach*. https://doi.org/10.1201/b12968

Wagner, H. (1929). Ebene blechwandträger mit sehr dünnem stegblech (Metal beams with very thin webs). *Zeitschrift Für Flugtechnik Und Motorloftschiffahr*, (20), 8–12. https://doi.org/10.1002/zamm.19250050103

Walraven, J. C. (1978). *The influence of depth on the shear strength of lightweight concrete beams without shear reinforcement*.

Weibull, W. (1939), "A Statistical Theory of the Strength of Metals", *Proceedings of the Royal Swedish Institute for Engineering Research*, 151.

Wells, A. A. (1961). Unstable crack propagation in metals, cleavage and fast fracture. *The Crack Propagation Symposium, Cranfield*, *1*(210–230).

Westergaard, H. M. (1938). A problem of elasticity suggested by a problem in soil mechanics; soft material reinforced by numerous strong horizontal sheets. In *Contributions to Mechanics of Solids, Stephen Timoshenko Sixtieth Anniversary Volume* (pp. 268–277). New York: The Macmillan Company.

Willam, K., Pramono, E., & Sture, S. (1987). Fundamental Issues of Smeared Crack Models. In *Proceedings of SEM/RILEM International Conference on Fracture of Concrete and Rock*. Houston. Texas.

Zhou, Y., Su, K., & Wu, H. (2015). Hydro-mechanical interaction analysis of high pressure hydraulic tunnel. *Tunnelling and Underground Space Technology*, *47*, 28–34. https://doi.org/10.1016/j.tust.2014.12.004

.